IPRenewal NPEmails

From: Gray, Dara F [DGray@entergy.com]
Sent: Monday, August 08, 2011 6:44 AM
To: Stuyvenberg, Andrew
Cc: Bessette, Paul M.; Sutton, Kathryn M.; Dacimo, Fred R.; YOUNG, GARRY G
Subject: FW: Follow up to email from Friday
Attachments: Hudson Modeling Report_22Mar10_wApps.pdf

Follow Up Flag: Follow up
Flag Status: Flagged

Hi Drew
I just wanted to make sure that you are in the loop in terms of where things stand with NMFS, on the technical end.

On this subject, do you have any information regarding the schedule/status of the BO? Based on the teleconference minutes, it looks like the draft BO should be out about August 26th.

Thanks and please don't hesitate to call if you have any questions.

From: Mark Mattson [mailto:mmattson@normandeau.com]
Sent: Friday, August 05, 2011 7:53 PM
To: Julie Crocker
Cc: Craig Swanson; Gray, Dara F
Subject: RE: Follow up to email from Friday

Julie – Thank you for clarifying your interest in information relating to Indian Point's thermal discharge plume extent analyses performed by ASA with Normandeau's assistance. The detailed reply below addresses your remaining questions using information from these analyses, underscoring that the analyses reflect extreme conditions – a "worst case" type condition experienced only once in the ten years of data analyzed during a limited summer period.

The ASA report "Hydrothermal Modeling of the Cooling Water Discharge from the Indian Point Energy Center to the Hudson River", 22 March 2010 presents a series of figures and text addressing plume extent, again for the extreme condition defined in the report. I have attached a PDF copy of this report in case you do not have one readily available and want to refer to it while reviewing this response (hopefully your email server will accept a 7 meg attachment).

Your inquiries about the lateral extent of the plume are addressed in Figure 7-9 on page 63 and Figure 7-10 on page 64. These two figures show the maximum surface plume extent for two stages within the dynamic tidal cycle, slack before flood and slack before ebb, respectively. Ambient conditions are represented by the dark blue color in the plan view color contour maps of the temperature in the river. Discussion of these figures is given on page 62 of the report. Because this is a surface plume, its scope will be larger than any other dimension measured, e.g., bottom or mid-water column, which enters a factor of conservatism in the figure with respect to your question.

Your inquiries about the vertical extent of the plume are addressed in Figure 7-15. That figure shows both the horizontal extent of the 4°F delta temperature above ambient and a vertical extent of the plume for a section downstream of IP, just north of Stony Point, under the studied extreme conditions.

Detail about the surface plume extent can be derived from the percent area coverage of the 4°F and 1.5°F criteria related delta temperatures above ambient background shown in Figure 7-14 and Figure 7-17, respectively. As summarized on page 73 of the report:

> "the model results for the simulation time period showed that the 4°F temperature rise covered less than 15% of the River vertical cross sectional area at the transects at all times during the simulation period, and generally

covered less than 3% of the cross sectional area. The model results also showed that the 4°F temperature rise surface extent was less than 35% across the River at all times, and generally less than 20%. Thus the model results show that the plant is in compliance with the NYSDEC thermal WQS.

In addition, the 1.5°F temperature rise above ambient was calculated for times when the ambient temperature exceeded 83°F. The 1.5°F temperature rise covered less than 40% of the River cross sectional area at all times, and generally covered less than 20 % of the cross sectional area. The 1.5°F cross-river temperature rise extent at the surface was also less than 40% across the River at all times and generally less than 21%."

Finally, based on the information from the criteria analyses, the following table of plume areas was developed for the 4°F delta temperature areas indicating the extent of the plume on an instantaneous and 24 hour average basis for the depth layer overlying the river bottom, which is the sturgeon habitat. Note that all of the data provided are consistent with the instrument accuracy +/- 1°F of the field observations to which the model was calibrated, and therefore provide a reasonable inference with respect to ambient conditions.

Percentile of Plume Extent	Instantaneous (acres)	24 Hr Avg. (acres)
Max	68	9
99%	39	8
95%	10	7
90%	2	4
80%	-	3
75%	-	3
50%	-	0
25%	-	-
20%	-	-
10%	-	-
5%	-	-
1%	-	-
Min	-	-

We trust this answers your remaining questions, particularly since NYSDEC staff already have agreed that Entergy's plume conforms to NYSWQS that necessarily reflect ensuring sturgeon protection and propagation." Take care and have a great weekend. Mark

><((((:> ><((((:> ><((((:> ><((((:>
Mark T. Mattson, Ph.D., Vice President
Normandeau Associates, Inc.
30 International Drive, Suite 6, Portsmouth NH 03801
Direct Phone: 603.319.5307
Cell: 603.345.0071

From: Julie Crocker [mailto:Julie.Crocker@Noaa.Gov]
Sent: Monday, August 01, 2011 5:05 PM
To: Mark Mattson
Subject: Re: Follow up to email from Friday

Hi Mark -

Thank you for the follow up info - that is helpful. Re. the request for the distance when the plume is fully dissipated/no longer detectable...as part of our biological opinion we need to describe the "action area" -- (see 50 CFR 402.02 "action area"), which is the geographic area that is affected by the action, so in this case it would include the area within the river where water temperature is affected by the discharge from Indian Point. I understand that this is a dynamic system and the geographic extent would not be static and may be constantly changing, but if it can be described in a meaningful way, even in a "worst case" scenario, that would be helpful as it would describe the maximum extent of the area affected. The description of the action area shapes some of our other analysis (for example, in our "environmental baseline" section of the Opinion we are required to include information on other actions that are happening in the "action area" - so if there was a dredging project or scientific research or something else that could affect shortnose sturgeon in that geographic area it would be discussed here, if it fell outside that area it would not be). Does that make sense?

Julie

On 7/25/2011 5:09 PM, Mark Mattson wrote:
Hi Julie – very strange about the yellow highlight, I couldn't make it go away in this response either. I managed to connect with Craig Swanson after lunch today, and we discussed your questions. We both are a bit baffled about your interest in ambient in Question 1 and the first part of Question 2. We don't understand why ambient would be part of the analysis, particularly since the Hudson at Indian Point is extremely dynamic with respect to both tidal and freshwater flow, and therefore continuously changing throughout each day. Perhaps Craig and I can give you a call (on Wed., I am out tomorrow) to discuss your intent for seeking the ambient information in order to help us answer Question 1 and the first part of Question 2.

The answer to the second part of question 2 is that below 5m the 33.7°C and 34.8°C are never experienced based on the 2010 thermistor data, which represented an extreme condition scenario experienced only for a brief period over the twenty year timeframe reviewed.

For Question 4, the answer is yes, the maximum recorded temperature for the 2010 survey - which again represented an extreme condition scenario - was 95.1°F recorded by the surface thermistor at station 25.

For Question 3, we will have to examine the historical monitoring data to describe the mosaic of bottom temperatures in space and time with respect to 28°C, so this will take a few days.

As always, please let me know if you have any questions and I will do my best to provide answers. Take care. Mark

><((((:> ><((((:> ><((((:> ><((((:>
Mark T. Mattson, Ph.D., Vice President
Normandeau Associates, Inc.
30 International Drive, Suite 6, Portsmouth NH 03801
Direct Phone: 603.319.5307
Cell: 603.345.0071

From: Julie Crocker [mailto:Julie.Crocker@Noaa.Gov]
Sent: Thursday, July 21, 2011 1:47 PM
To: Mark Mattson
Cc: dgrey@entergy.com
Subject: Re: Follow up to email from Friday

Hi Mark -

I've read through it a few times now and have a couple of remaining/clarifying questions that I've outlined below (all minor I believe!).... I apologize for the highlighting - I can't get it to go away! Thank you for your work on this.

1. At what distance from the outfall do temperatures return to ambient?

2. At what distance from the surface does the influence of the plume stop being detectable? Is it the 5m/16 feet from the surface, or is that just a reference to the depth that the 33.7C or 34.8C are never experienced?

3. The 7-8-11 email states that shortnose sturgeon could encounter near bottom areas with temps of 28°C but only in "discrete locations" and during "brief intervals". Is there information available that would allow you to describe how large these areas would be and for how long they would persist?

- 4.The information on p. 62 of the Swanson report seems to indicate that temperatures at thermistor station 25 reached 95.1°F. Is this the maximum temperature recorded at any of the measuring stations?

5. Thanks,
Julie

4.

On 7/13/2011 5:30 PM, Mark Mattson wrote:
Hi Julie – I just got back in from a long weekend, and the folks at Indian Point wanted me to follow up with you to confirm your receipt of that email I sent to you on Friday 8 July to address your 30 June questions about Indian Point's thermal plume and shortnose sturgeon. Did you get that email, and if so, is there any more information you need from me at this time? Thank you. Mark

><((((:> ><((((:> ><((((:> ><((((:>
Mark T. Mattson, Ph.D., Vice President
Normandeau Associates, Inc.
30 International Drive, Suite 6, Portsmouth NH 03801
Direct Phone: 603.319.5307
Cell: 603.345.0071

Hearing Identifier: IndianPointUnits2and3NonPublic_EX
Email Number: 2819

Mail Envelope Properties (DCB622189B67AD49AE39CD3ED1B4D99D114AE809)

Subject: FW: Follow up to email from Friday
Sent Date: 8/8/2011 6:44:21 AM
Received Date: 8/8/2011 6:45:34 AM
From: Gray, Dara F

Created By: DGray@entergy.com

Recipients:
"Bessette, Paul M." <pbessette@morganlewis.com>
Tracking Status: None
"Sutton, Kathryn M." <ksutton@morganlewis.com>
Tracking Status: None
"Dacimo, Fred R." <FDacimo@entergy.com>
Tracking Status: None
"YOUNG, GARRY G" <GYOUNG4@entergy.com>
Tracking Status: None
"Stuyvenberg, Andrew" <Andrew.Stuyvenberg@nrc.gov>
Tracking Status: None

Post Office: IPCEXETSP001.etrsouth.corp.entergy.com

Files	**Size**	**Date & Time**
MESSAGE	10549	8/8/2011 6:45:34 AM
Hudson Modeling Report_22Mar10_wApps.pdf	7076645	

Options
Priority: Standard
Return Notification: Yes
Reply Requested: Yes
Sensitivity: Normal
Expiration Date:
Recipients Received: Follow up

Report Prepared for:
Elise Zoli
Goodwin Proctor
55 State Street
Boston, MA 02109

Hydrothermal Modeling of the Cooling Water Discharge from the Indian Point Energy Center to the Hudson River

ASA Project 09-167 **Report** **22 March 2010**

Prepared by:
Craig Swanson
Daniel Mendelsohn
Yong Kim
Deborah Crowley

Applied Science Associates, Inc.
55 Village Square Drive
South Kingstown, RI 02879

Executive Summary

The Indian Point Energy Center (IPEC), consisting of two operating nuclear power plants (Units 2 and 3) in the village of Buchanan, New York, is located along the eastern side of the Hudson River (River) approximately 42 miles upstream of the Battery (southern tip of Manhattan). IPEC uses a once-through cooling water configuration to cool the two operating nuclear reactors discharging heated water employed in the cooling process associated with electricity generation through a common discharge canal. We have been advised that, in support of the license renewal application for Units 2 and 3, Entergy Nuclear Indian Point 2, LLC, Entergy Nuclear Indian Point 3, LLC, and Entergy Nuclear Operations, Inc. (collectively, "Entergy") has applied for a Water Quality Certification (WQC) under Section 401 of the federal Clean Water Act (WQC), the approval of which is based upon a finding that there are reasonable assurances that Units 2 and 3 will operate in compliance with applicable New York water quality standards (WQS), which include thermal WQS (Thermal WQS). This report addresses the Thermal WQS. For purposes of this report, the relevant New York State WQS is *6 NYCRR Part 704.2(b)(5): Special Thermal Criteria for Estuaries of Portions of Estuaries.* To evaluate IPEC's compliance with these criteria, this report describes the methodology and results of the thermal modeling component of a triaxial thermal study that consisted of a combination of field work, data analysis and numerical modeling. An initial report (Swanson et al., 2010), representing a summary of the empirical field work (Field Program), was submitted to NSYDEC on 12 February 2010, and established that IPEC's operations met Thermal WQS, as measured during the Field Program. This report focuses on the numerical modeling, which establishes that IPEC satisfies Thermal WQS during all average and extreme-case environmental conditions.

The Field Program, consisting of an fixed extensive thermistor array and mobile studies, was performed to monitor River temperatures and currents at various locations in the River from northern Haverstraw Bay (downstream) to the Bear Mountain Bridge (upstream) during a six-week period from 24 September through 3 November 2009. These data were analyzed, along with other publicly available River observations from the United States Geological Survey (USGS) and meteorological observations from the Northeast Regional Climate Center (NRCC), to first assess the dynamics of the thermal plume resulting from the IPEC discharge, and then to understand the response of the plume to various environmental forcing factors, such as tides, River water temperature and currents, as well as meteorological conditions that substantially effect thermal regimes.

The long term, fixed mooring field program used a sufficient number of thermistors (i.e., 300 thermistors on 50 moorings) to characterize the thermal structure in the River in the extended vicinity of Indian Point, accounting for the fact that the River's thermal structure varies with location, as well as with seasonal, daily, and tidal time scales. In addition, the flow data from two fixed current meters, at Indian Point and Stony Point, captured the physical dynamics – including velocity and water elevation over time -- in this area, which also influence the thermal regime. The relative contributions of different forcing mechanisms, including River flow, tide and estuarine circulation, cause temporal and spatial variability of the flow patterns. In general, bi-directional tidal flow with a period of 12.42 hours is dominant. The combined effect of River flow and salt intrusion resulted in estuarine circulation, where the surface flow was stronger during ebb while the bottom flow was stronger during flood. Also, the distinctive signal of the bi-weekly spring-neap cycle was observed at both Indian Point and Stony Point stations. In addition there are infrequent storm surge events that cause River elevations to rise and affect the regular flood and ebb tidal cycle, sometimes dramatically (e.g., elimination of the flood tide during one event). Nonetheless, during the

deployment period, the combination of the surface temperatures at the upstream and downstream boundaries appears to be a reasonable proxy for surface ambient conditions.

As noted above with respect to the Field Program and as confirmed in the 12 February 2010 Report (Swanson et al., 2010), the in-River thermal monitoring data collected during the deployment period, 9 September through 1 November 2009, showed Indian Point to be in compliance with 6 NYCRR §704.2(b)(5). The surficial extent of the plume did not exceed 67% of the cross River distance, and the areal extent of the plume did not exceed 50% of the River cross sectional area. Based on the Field Program data, the thermal plume was restricted to the surface and mid depth layers in the River, never extending to the bottom layers. The Field Program was performed, consistent with a protocol provided to New York State Department of Environmental Conservation (Department) staff.

Also consistent with the protocol submitted to Department staff, the field observations and insight gained from the Field Program were then used to develop and calibrate a three dimensional hydrothermal model of an area that covered a spatial extent from Hastings on Hudson, approximately 20 miles north of the Battery, to the upstream dam at Troy (Study Area). The model domain longitudinal extent spans approximately 130 miles, the lateral extent follows the varying width of the River cross section, and the vertical extent was captured by assigning a depth to each model grid cell, which was represented in eleven vertical layers, based on bathymetric analysis. A total of 51,909 cells were used in the model calculation consisting of 4,719cells in 11 levels.

The model application used water surface elevation (tides), water temperature and salinity at the southern boundary (Hastings on Hudson), and River flow and water temperature at the northern boundary (the dam at Troy)]. Meteorological forcing, including winds, solar radiation and air temperatures, was applied at the water surface. Plant forcing data consisted of intake and discharge temperatures, as well as cooling water flows.

The model calibration was successfully performed with both qualitative and quantitative methods that represent the industry standard, providing confidence in model results. Time series comparisons of model vs. observations at the monitoring station locations were successfully established, as well as calculation of quantitative statistics, including relative mean error (RME), error coefficient of variation (ECV), square coefficient of variation (R^2) and model skill. The parameters that were evaluated in the model calibration phase were water surface elevations, currents and temperatures. Specifically, the time series of observations vs. model predictions showed that the model captured both the surface elevation variations and currents with respect to phase and amplitude. The model was able to successfully simulate the current velocities with respect to the important tidal signals in the River including semi-diurnal bi-directional flow, diurnal inequality and bi-weekly spring-neap cycle. Most importantly, the model was able to simulate both the long-term trend of decreasing water temperature, due to the changing seasons and the short-term water temperature fluctuations, due to tidal flow observed at the thermistor mooring locations.

The table below summarizes the three averaged calibration statistic metrics for water surface, current velocities, and temperature. The summary shows that the model does well at achieving the goal metrics with the water surface elevation meeting three guidance values and only slightly exceeding the fourth; the current velocities meet two of the guidance values and slightly exceed two; and, most importantly, the temperature meets all guidance values. Those metrics that are met are shown with bolded font.

Model averaged calibration statistics summary.

Parameter	RME (%)	RME Goal	ECV (%)	ECV Goal	R^2	R^2 Goal	Skill	Skill Goal
Water Surface Elevation	**3**	<30	**9**	<10	0.90	>0.94	**0.96**	>0.85
Current Velocity	**6**	<30	14	<10	0.83	>0.94	**0.93**	>0.92
Temperature	**0**	<25	**1**	<45	**0.93**	>0.84	**0.94**	>0.85

Once the model was successfully calibrated, as here, it was used with confidence to run other time periods, including extreme environmental conditions, employing the same methodology of model forcing and modeling coefficients. To do so, the model scenario timeframe for simulations was developed, using a ten-year dataset of information based on observations compiled by USGS and NRCC. The goal of developing the scenario timeframe was to ensure that critical environmental conditions which have the largest influence on River temperature (particularly, with respect to the water quality criteria pertaining to spatial extent of the thermal plume) are captured. There were two steps in determining the time in which the influence of IPEC on the River would be most significant: a correlation analysis to determine the most influential environmental forcing factors on temperature in the River, and a joint probability analysis to determine the times at which the top three influential environmental factors synoptically occur at their individual 50^{th}, 90^{th}, 95^{th} and 99^{th} percentile values. The correlation analysis showed that the water temperatures near IPEC are most influenced by upstream River flow, water temperature and air temperature. The joint probability analysis showed that these parameters more frequently reach their higher percentile values during summer months, even more specifically during the month of August. Based on the detailed results of the joint probability analysis, the critical environmental conditions scenario timeframe was determined to be 1 August through 15 August 2005. This timeframe captures hourly occurrences of the three-way joint probability 50^{th}, 90^{th} and 95^{th} percentile conditions The 99^{th} percentile joint conditions were not found to occur naturally anytime during the 10 years of data analyzed.

Once the scenario timeframe was established, the calibrated model was then used to simulate this period for two cases; one with the plant operating at maximum capacity (5163.4 MW thermal with a flow rate of 1762.2 KGPM), and one simulating conditions with the plant not operating. The model application to the August 2005 Scenario time frame was first compared to available observations during that period. This constitutes a qualitative model validation to a consistent but small independent data set. A comparison of the model predicted water surface elevations at West Point, Poughkeepsie and Albany was made. A similar comparison for the model predicted surface water temperatures at the same USGS stations. While the modeled and observed temperature signals at Poughkeepsie and Albany are relatively uneventful, the model clearly reproduced the combined diurnal and semi-diurnal temperature signals at West Point, nearest to the upstream end of the Indian Point study area.

The scenario temperature results were post-processed to determine if the plant-in-operation case showed any occurrence of water temperature greater than 90°F, the maximum allowable per WQS. The results of the 90 °F analysis showed that the surface area coverage is predominantly semi-diurnal (tidally driven) and remains under 35 acres during the simulation period and is typically less than 20 acres. This area compares favorably to (is significantly smaller than) permitted mixing zones at other power stations along the river.

The results were further processed to determine the surface temperature difference for each model grid cell (totaling 51,909 cells) between the two cases run, for every time step of the model run. This post-processing result represents the temperature rise between the IPEC's discharge and the environmental background (without the plant), thus isolating the IPEC thermal contribution. These results were used to delineate the presence of a differential temperature greater than 4°F along representative cross sections of the River to determine either if the 67% cross-River distance or 50% cross sectional area requirements were in compliance. The transects chosen for evaluation of these metrics included one at IPEC, one at 3,000 ft (S2) and one at 1.5 miles (Stony Point) downstream from IPEC and one at 4,500 ft upstream (Charles Point).

The model results for the simulation time period showed that the 4°F temperature rise covered less than 15% of the River vertical cross sectional area at the transects at all times during the simulation period, and generally covered less than 3% of the cross sectional area. The model results also showed that the 4°F temperature rise surface extent was less than 35% across the River at all times, and generally less than 20%. Thus the model results show that the plant is in compliance with the NYSDEC thermal WQS.

In addition, the 1.5°F temperature rise above ambient was calculated for times when the ambient temperature exceeded 83°F within the timeframe designed in the Thermal WQS. In order to determine when the ambient river temperature exceeded the 83°F threshold, the environmental background case was evaluated at a representative station near the plant. The 1.5°F temperature rise covered less than 40% of the River cross sectional area at all times, and generally covered less than 20 % of the cross sectional area. The 1.5°F cross-river temperature rise extent at the surface was also less than 40% across the River at all times and generally less than 21%. All of these extents are consistent with the thermal WQS set forth in 6 NYCRR §704.2(b)(5).

In conclusion, a field program was established to monitor the thermal plume from IPEC which was subsequently used to calibrate a numerical model representing the study area. This successfully calibrated model was then used to model extreme environmental conditions during both maximum IPEC heat rejection and a no plant heat load scenario representing ambient conditions. The results taken from the differential of these two model runs isolated the influence of IPEC on the thermal structure in the River. These results, as well as the analysis of the field data, established that the thermal plume conforms to Thermal WQS, and, therefore, that there are reasonable assurances that IPEC will operate in compliance with applicable thermal criteria during the license renewal period.

Table of Contents

List of Figures

List of Tables

1. Introduction

The Indian Point Energy Center (IPEC), consisting of two operating nuclear power plants (Units 2 and 3), is located along the eastern side of the Hudson River (River) approximately 42 miles upstream of the Battery (located at the southern tip of Manhattan and defined as the mouth of the River) in the village of Buchanan, New York. IPEC uses a once-through cooling water configuration to cool two operating nuclear reactors discharging heated water employed in the cooling process associated with electricity generation through a common discharge canal. We have been advised that, in support of the license renewal application for Units 2 and 3, Entergy Nuclear Indian Point 2, LLC, Entergy Nuclear Indian Point 3, LLC, and Entergy Nuclear Operations, Inc. (collectively, "Entergy") has applied for a Water Quality Certification (WQC) under Section 401 of the federal Clean Water Act (WQC), the approval of which is based upon a finding that there are reasonable assurances that Units 2 and 3 will operate in compliance with applicable New York water quality standards (WQS), which include thermal WQS (Thermal WQS). This report addresses the thermal WQS. For purposes of this report, the relevant New York State WQS is *6 NYCRR Part 704.2(b)(5): Special Thermal Criteria for Estuaries of Portions of Estuaries: parts (i), (ii), (iii) & (iii).* The requirements set forth in these regulations dictate a maximum water temperature not to be exceeded of 90°F, and delineates both a surface distance limitation of 67% across the River, as well as a vertical cross sectional area limitation of 50% cross section, both that may not exceed a temperature differential of either 4°F or 1.5°F above ambient, under particular conditions. The 4°F differential is applicable when the River ambient temperature is less than 83°F, and a more stringent differential of 1.5°F is applicable when the River ambient temperature is above 83°F during the months of July through September. To evaluate IPEC's compliance with these criteria, this report describes the methodology and results of the thermal modeling component of a triaxial thermal study that consisted of a combination of field work, data analysis and numerical modeling.

Applied Science Associates, Inc. (ASA) and Normandeau Associates Inc. (NAI) were retained to design and carry out the Field Program, respectively, of the triaxial thermal study. The field survey consisted of a long term (8 September to 3 November), high resolution, fixed temperature and current observations using 50 thermistor arrays representing a total of 300 thermistors, as well as two days of mobile surveys that captured currents and temperature profiles of the River at various stages of the tide. The fixed observations consisted of temperature monitoring at fifty stations located near the IPEC, spanning approximately 4.5 miles north of and 5.5 miles south of IPEC, as well as two River current measurements at a location within the center of the River near Indian Point, as well as two miles south of the plant (Stony Point) during the time period from 24 September to 3 November. The mobile surveys, performed on 24 September 2009 and 30 October 2009 , spanned the section of the River as the fixed survey measured temperature and current cross profiles at numerous transects across the River, as well as measuring vertical temperature profiles at numerous spot locations along the center of the channel. The observations yielded from the Field Program were used to assess the extent of the thermal plume under the conditions observed during the Field Program, as well as to calibrate a numerical model (discussed below) used to simulate these and other conditions, including critical environmental conditions. A review and preliminary analysis of the Field Program, and dataset derived from that Program, is described in Swanson, et al. (2010), and was submitted to New York State Department of Environmental Conservation (Department) staff on 12 February 2010; this report is summarized in Chapter 3 and incorporated by reference to this report.

ASA was contracted to assess the thermal discharge from IPEC, and its potential effects on the River, using a state-of-the-art, boundary fitted computer simulation hydrothermal model previously

accepted for other modeling projects involving thermal assessments by the United States Environmental Protection Agency (EPA) and numerous state regulators. The model was set up, based on the known physical characteristics of the River and the environmental forcing parameters that drive the surface elevation, currents and temperatures within the River. The model was calibrated using Field Program data and observations. Background information on the model system is provided in Chapter 4, the details of the model application to the River are presented in Chapter 5 and the model calibration results are described in Chapter 6.

Subsequent to model calibration, ASA and NAI worked together to determine the critical timeframe in which extreme environmental conditions would cause potential IPEC thermal impacts to be the greatest This was achieved through a combination of a correlation analysis to determine the most influential environmental forcing factors on temperature in the River, and a three-way joint probability analysis to determine the times at which the top three influential environmental factors synoptically occur at their individual 50^{th}, 90^{th}, 95^{th} and 99^{th} percentile values. The methodology and findings of this analysis are described in Chapter 7. The timeframe identified through this procedure was then used as the model scenario simulation time period, and the model was run both with and without IPEC impacts to isolate its relative temperature contribution. The results of these simulations were used to compare the IPEC's thermal influence to the thermal water quality standards. The details of the model forcing, model results and the implications of these scenario results are documented in Chapter 7.

The study conclusions are summarized in Chapter 8 and references are listed in Chapter 9. Appendices A and B provide further details of the WQMAP model system.

2. Description of Study Area

The Hudson River is approximately 315 miles long, and originates at Lake Henderson in the Adirondack Mountains from which it flows south toward the Atlantic Ocean via New York harbor. The lower half of the Hudson is an estuary; as such, technically, the River portion extends only from Lake Henderson to Troy, NY from which point on it is a tidally influenced estuary. However, for the intents of this report, the Hudson River Estuary and the Hudson River will be treated as a single entity, referred to as the "River". The River depths vary naturally and because it is dredged in places. Depths vary generally from 32 feet (in the shipping channel in the lower section of the River) to more than 200 feet. Figure 2-1 illustrates the location of the Hudson.

The actual source of the River is located north of its origin at the Lake Tear of Clouds, as well as many tributaries within the vast 13,400 square miles of watershed that drain to the River. Freshwater flow is seasonal, with the greatest flow rates typically in the spring and fall, and lowest typically in the summer. The average River flow at the Federal Dam at Troy is 13,000 cubic feet per second (cfs) while the minimum and maximum flows are 882 cfs and 152,000 cfs respectively (USGS). The lower Hudson, south of Troy, also has freshwater inputs from tributaries, so that total freshwater flow in the region of IPEC exceeds measured flow at Troy.

The lower Hudson is tidal, meaning that it experiences two high and two low tides approximately every day. The tidal range varies from approximately 4.5 ft at the Battery in Manhattan (defined as the River mouth) to approximately 4ft at the northern end at Albany, with tidal amplitude attenuation observed in the lower portion followed by amplification in the upper portion. Salinity that intrudes from the Atlantic typically remains in the lower 45 miles of the River, but has extended as far as 60 miles upstream from the Battery. The average currents in the River vary from approximately 0 to 1.5 ft/s on average and are slightly greater during ebb tide, when the tide is receding and flowing in the same direction as the River flow.

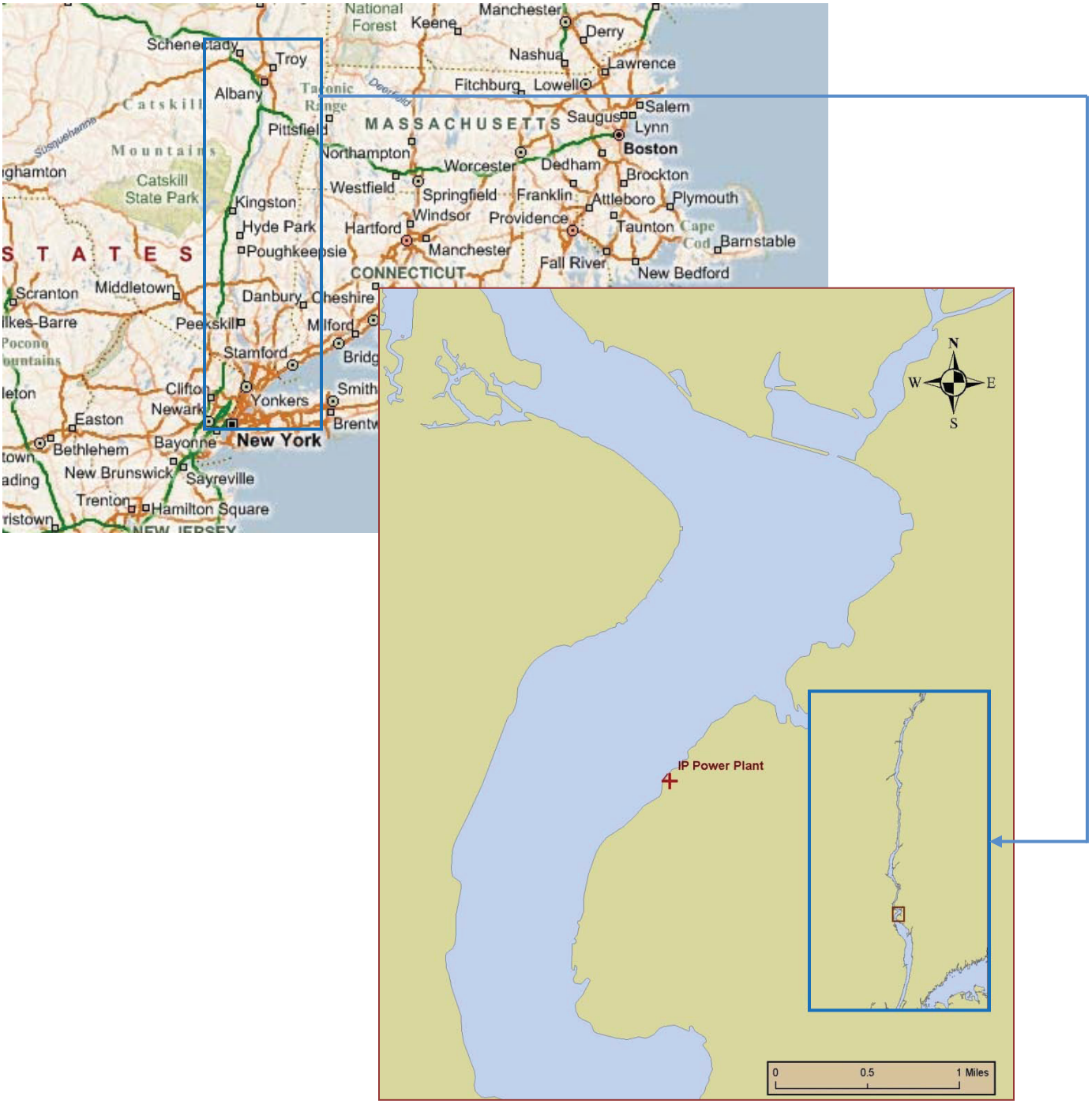

Figure 2-1 Study Area.

IPEC is a nuclear power plant with two operational reactors (Unit 2 and Unit 3); an aerial photograph of the plant is shown in Figure 2-2. The plant has a maximum rated capacity of 2,158MW (Enercon 2009). IPEC is located is in the village of Buchanan, New York approximately 41 miles upstream of the Battery along the eastern side of the Hudson River as illustrated in

Figure 2-2 IPEC Aerial View

3. River Characterization

An extensive field program was designed jointly by NAI and ASA to acquire in-River temperature and current velocity data with which to evaluate the potential characteristics of the thermal discharge in the River from Indian Point and to provide data with which to calibrate the model. Thermistors were used to measure temperature data, and Acoustic Doppler Current Profilers (ADCPs) were used to measure current velocities. Data considered here are from the field survey conducted by NAI from 24 September through 1 November 2009. Locations of these instruments are shown in Figure 3-1. The temperature data is discussed in the following section followed by a discussion of the current data.

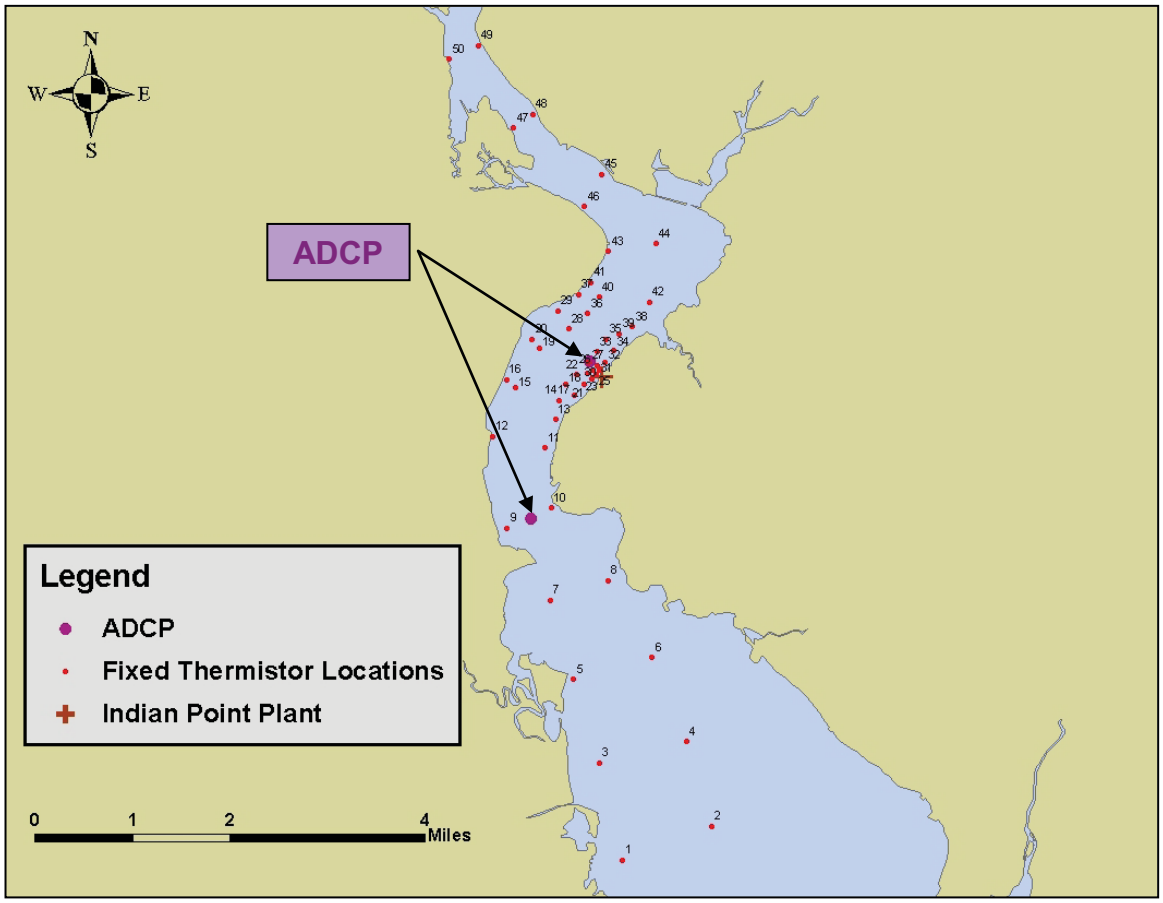

Figure 3-1 Plan view of 50 thermistor string moorings and two ADCP locations in the Hudson River.

3.1. Temperature

Over 4,700,000 temperature measurements were made during the deployment period from 9 September to 1 November 2009 from 300 thermistors located on 50 arrays linked to 50 fixed moorings. Each thermistor collected data instantaneously at 5-min intervals. A more detailed description of the filed deployment can be found in Swanson et al. (2010). This density of instruments and sampling rate was sufficient to capture the thermal structure and was performed consistent with the protocol provided to NYSDEC staff.

The data presented here focus mainly on the period of 24 September to 3 November 2009, when both current and temperature data sets are available. Data from a thermistor mooring near the IPEC discharge (station 27) is shown in Figure 3-2. There is a general seasonal-based water temperature cooling effect shown over time with the mean temperature dropping approximately 20°F over the 24 September to 3 November 2009 period]. The oscillations shown most clearly in the surface and near-surface temperatures are caused by the tides with a 12.42-hr period. The highest temperatures are found at the shallowest thermistor (1.2 ft) followed closely by temperatures at 5.0 ft. The large amplitude of the variation in these temperatures is due to the proximity to the IPEC discharge which typically heats its intake water by 15 to 20 °F before discharge to the River.

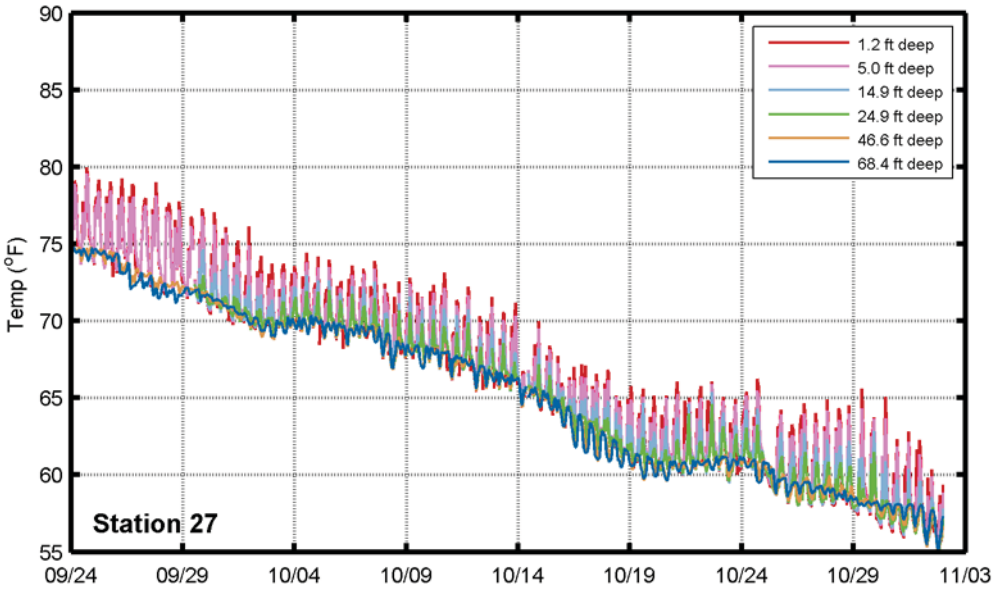

Figure 3-2 Time series of temperature at station 27.

Data from thermistor moorings at the southern and northern boundaries (stations 1 and 50, respectively) are shown in Figure 3-3 and Figure 3-4, respectively. There is again seen a general cooling effect shown over time with the mean temperature dropping approximately 20 °F over the deployment period. Although the oscillations are caused by the tides with a 12.42-hr period, the amplitude of the variation in surface temperatures is much smaller (maximum of 3 °F) than that observed at station 27.

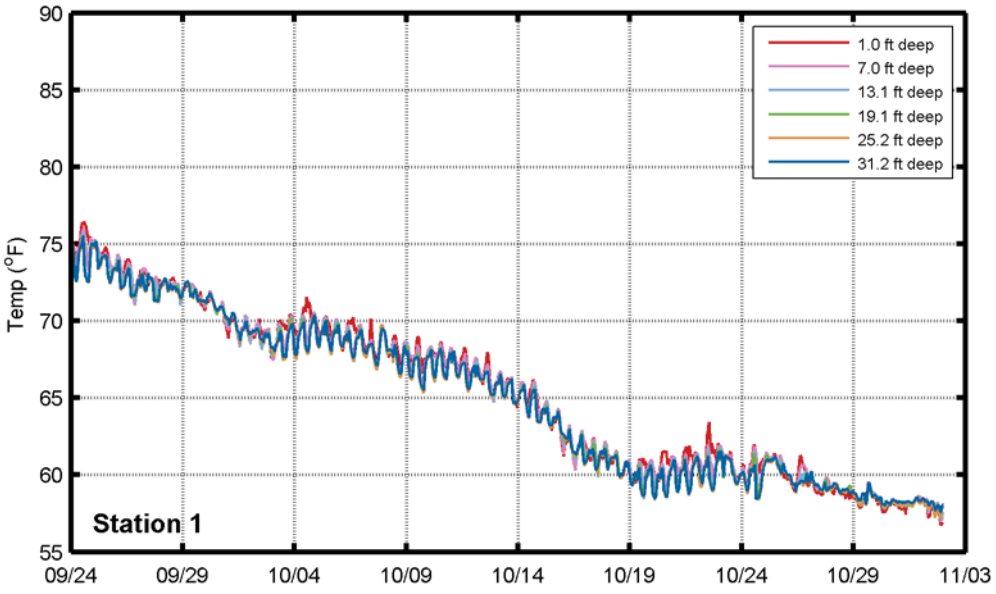

Figure 3-3 Time series of temperature at station 1.

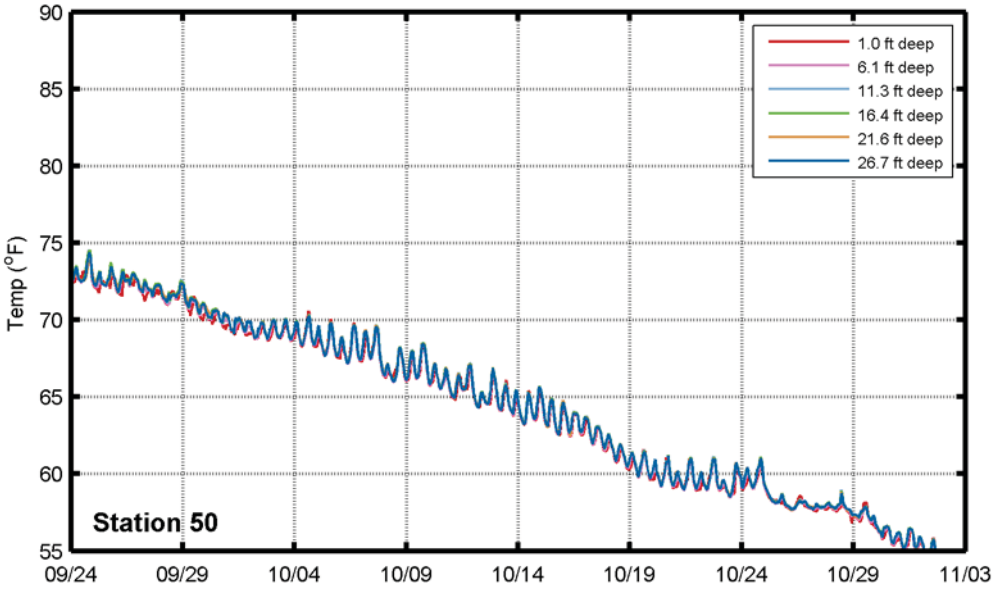

Figure 3-4 Time series of temperature at station 50.

3.2. Currents

Among the important factors controlling the thermal regime in the River are the currents in the vicinity of the IPEC. Previous studies on dynamics of the River show that tidal velocities are much higher than the velocity induced from freshwater inflow to the River (Geyer and Chant, 2006). Thus, in this part of the River, the flows are bi-directional with the period of 12.42 hrs. In addition, this tidal forcing also varies with a longer period generally of 14 days, due to the relative location of Sun and Moon, generating so-called neap-spring cycle. During spring tide, the current is faster and thus

more vertical mixing occurs. During neap, less mixing due to lower currents occurs which results in more intrusion of salt up the River. Owing to this neap-spring variation of the mixing, the River has known to be transitional between salt-wedge conditions during neap and well-mixed estuarine conditions during spring tide (Geyer et al., 2000). Due to this salt intrusion in the River, there is a strong horizontal salinity gradient along the estuary. This causes a longitudinal density gradient resulting in estuarine circulation, where the bottom flow is directed upstream and the surface flow is directed downstream. Relative contributions of such forcings as River discharge, tidal flow and estuarine circulation characterize the flow pattern, which varies over time and space due to the variation of those physical processes.

3.2.1. Currents at Indian Point

The ADCP data collected during the field program show the temporal variation of the current velocities that reflect the variability of the forcings mentioned in the previous section. Figure 3-5 shows the time series of surface and bottom current vectors taken from the ADCP at Indian Point (approximately 0.18 mi (270 m) from the discharge canal (see Figure 3-1 for location). The length of the vector represents speed, and the angle of the line represents direction: north to up and east to right. Both surface and bottom flows are mainly controlled by the tides with a 12.42 hr period, and are thus bi-directional following the River geometry along a generally NE-SW axis. In general, the surface current is stronger than the bottom current due to the well-known reduction due to bottom friction at the seabed. The current velocities from ADCP Bin 11, approximately 13.7 ft deep, were found to be a complete record of near surface currents, and thus used as representative of surface currents (Figure 3-5a). For the surface layer, the maximum peak upstream (flood) velocity is 3.0 ft/s on 4 November; the minimum peak upstream velocity is 0.6 ft/s on 18 October; and the mean peak upstream velocity is 1.0 ft/s. Also for the surface layer, the maximum peak downstream (ebb) velocity is 3.8 ft/s) on 29 October; the minimum peak downstream stream velocity is 1.7 ft/s on 27 September; and the mean peak downstream velocity is 1.6 ft/s. The surface current has a mean downstream component of 0.5 ft/s, resulting a net speed similar to the River flow. Figure 3-5 also shows the biweekly spring-neap cycle clearly in the ebb (downstream) currents with small velocities recurring around 28 September, 12 October and 27 October.

For the bottom layer (Figure 3-5b), defined as Bin 1 from the ADCP data as approximately 49.8 ft deep, the maximum peak upstream (flood) velocity is 2.6 ft/s on 29 October; the minimum peak upstream velocity is 0.8 ft/s on 25 October; and the mean peak upstream velocity is 1.1 ft/s. Also for the bottom layer, the maximum peak downstream (ebb) velocity is 2.6 ft/s on 7Oct09; the minimum peak downstream stream velocity is 0.1 ft/s on 28 September; and the mean peak downstream velocity is 0.9 ft/s. The mean bottom velocity over the entire period is 0.2 ft/s upstream, typical of two layer estuarine flow due to the density gradient. The bottom flows show more distinctive spring-neap cycle as of very small downstream current during late September and late October.

One highly atypical feature reflected in Figure 3-5 is the lack of a flood tide early on 25 October. It appears this occurred after a storm surge moved into the River from the ocean raising water levels by approximately 1 ft for about 18 hrs. As the surge ended, the resulting downstream flow was sufficient to overwhelm to predicted flood tide and prevented any upstream flow. The bottom currents shown in Figure 3-5b show a reduction greater than 50% in the expected flood velocity during this time.

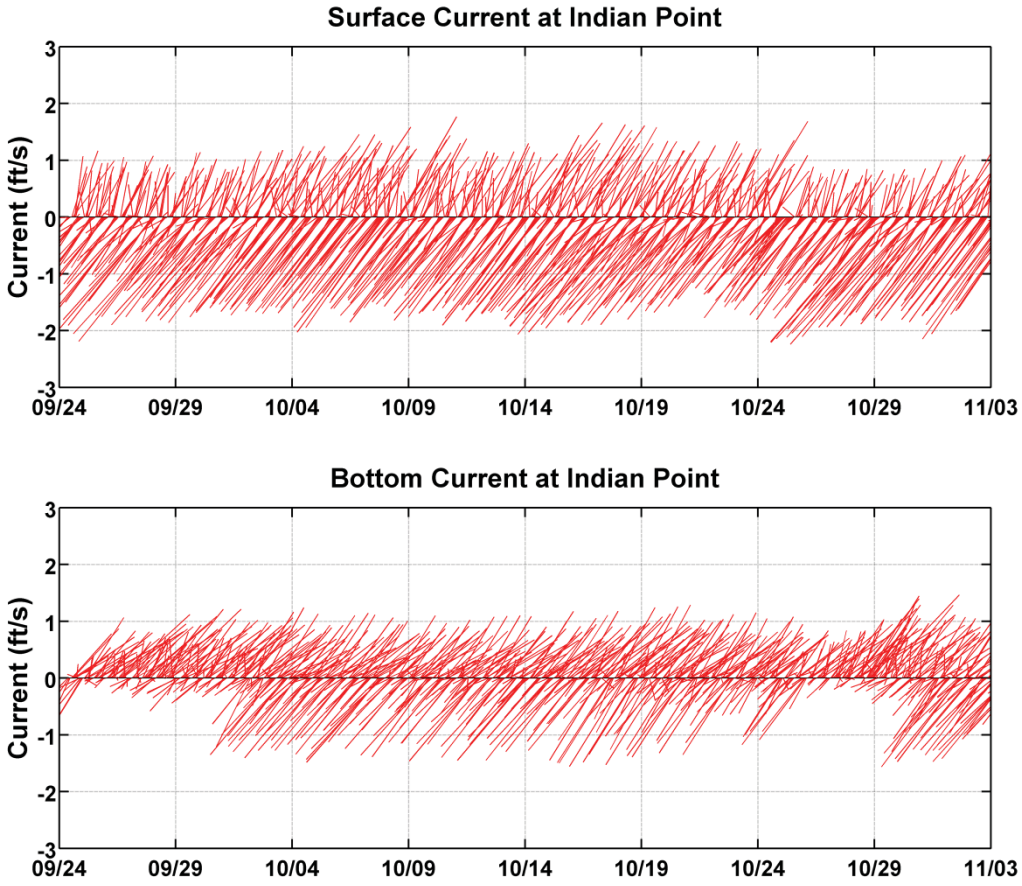

Figure 3-5 Vector plot for (a) surface and (b) bottom current at Indian Point station.

3.2.2. Flow at Stony Point

Figure 3-6 shows the time series of surface and bottom current vectors taken from the ADCP moored at Stony Point (approximately 2 miles south of Indian Point). Both surface and bottom flows are mainly controlled by the tides with a 12.42 hr period, and thus bi-directional following the River geometry along a generally NW-SE axis. The current velocities from ADCP Bin 15, approximately 17.6 ft deep, were found to be a complete record of near surface currents, and thus defined as representative of surface currents. For the surface layer (Figure 3-6a), the maximum peak upstream (flood) velocity is 2.6 ft/s on 8 October; the minimum peak upstream velocity is 0.81 ft/s on 27 September; and the mean peak upstream velocity is 1.2 ft/s. The maximum peak downstream (ebb) velocity is 2.9 ft/s on 3 November; the minimum peak downstream stream velocity is 1.4 ft/s on 26 September; and the mean peak downstream velocity is 1.4 ft/s. The mean surface velocity over the entire period is 0.2 ft/s downstream typical of two layer estuarine flow. Figure 3-6 also shows the biweekly spring-neap cycle clearly in the ebb (downstream) currents with small velocities recurring around 28 September, 12 October and 27 October.

For the bottom layer (Figure 3-6b), defined as Bin 1 from the ADCP data as approximately 63.5 ft deep, the maximum peak upstream (flood) velocity is 2.8 ft/s on 18 October; the minimum peak upstream velocity is 0.36 ft/s on 28 September; and the mean peak upstream velocity is 1.2 ft/s. The maximum peak downstream (ebb) velocity is 2.5 ft/s on 3 November; the minimum peak downstream stream velocity is 0.1 ft/s on 27 October; and the mean peak downstream velocity is

1.1 ft/s. The mean bottom velocity over the entire period is 0.3 ft/s upstream, again typical of two layer estuarine flow. Also, the bottom flows show more distinctive spring-neap cycle as no or very small downstream current during late September and late October.

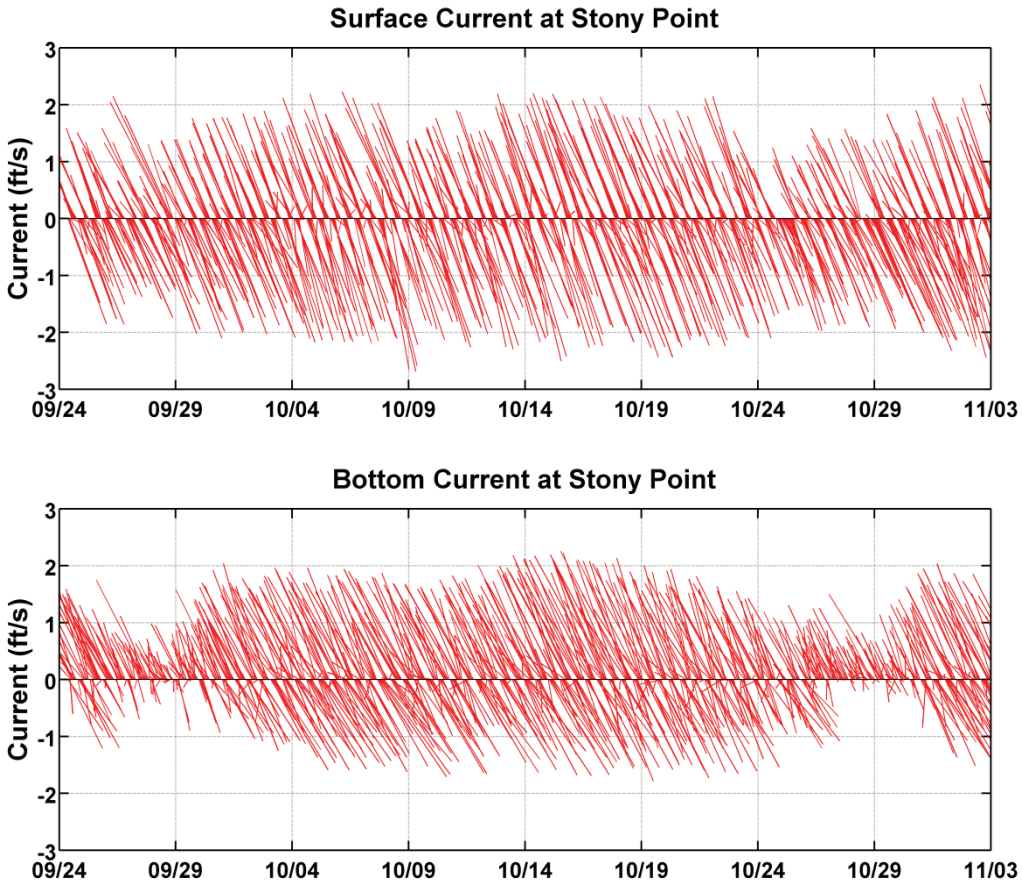

Figure 3-6 Vector plot for (a) surface and (b) bottom current at Stony Point station.

4. Hydrothermal Model

The hydrothermal computer model used to predict the velocity and temperature structure of the Hudson River, and IPEC's potential thermal influence, is part of a PC-based modeling system, known as Water Quality Mapping and Analysis Program (WQMAP) (Mendelsohn et al., 995). The focus of the model in this instance is the spatial extent of the plume, consistent with New York thermal criteria, an area known as the far field. The model calculates the circulation and thermal characteristics in the far field area where the initial plume momentum has dissipated and the plume is affected only by the ambient currents. ASA determined that near field modeling to predict plume dilution in the relatively small area where the discharge plume is primarily influenced by its own momentum was not required.

4.1. Model Description - BFHYDRO

WQMAP consists of a family of computer models, one of which is a hydrodynamic (hydrothermal) model known as BFHYDRO. A three dimensional, general curvilinear coordinate, boundary-fitted computer model (Muin and Spaulding, 1997; Huang and Spaulding, 1995b; Swanson et al, 1989)BFHYDRO was used to predict elevations, velocities, salinities and temperatures in the Hudson River. The boundary-fitted model matches the model coordinates with the shoreline boundaries of the water body, accurately representing the study area. This system also allows the user to adjust the model grid resolution as desired. This approach is consistent with the variable geometry of shoreline features of the River. Development of the boundary fitted model approach has proceeded over more than two decades (Spaulding, 1984; Swanson et al., 1989; Muin, 1993; and Huang and Spaulding, 1995a). The model may be applied in either two or three dimensions, depending on the nature of the inquiry and its complexity. In this instance, a three-dimensional or triaxial study was performed.

The boundary fitted method uses a set of coupled quasi-linear elliptic transformation equations to map an arbitrary horizontal multi-connected region from physical space to a rectangular mesh structure in the transformed horizontal plane (Spaulding, 1984). The three dimensional conservation of mass and momentum equations, with approximations suitable for lakes, rivers, and estuaries (Swanson, 1986; Muin, 1993) that form the basis of the model, are then solved in this transformed space. In addition a sigma stretching system is used in the vertical to map the free surface and bottom onto coordinate surfaces to resolve bathymetric variations. The resulting equations are solved using an efficient semi-implicit finite difference algorithm for the exterior mode (two dimensional vertically averaged), and by an explicit finite difference leveled algorithm for the vertical structure of the interior mode (three dimensional) (Swanson, 1986). The velocities are represented in their contra-variant form.

A detailed description of the model used for the IPEC study, with associated test cases, is included as Appendix A (Muin and Spaulding, 1997). The publication was originally part of a Ph.D. dissertation (Muin, 1993), which extended the boundary fitted model capabilities developed by Swanson (1986), applying a contra-variant velocity formulation to the transformed momentum equations. A brief description of the model follows.

The basic equations are written in spherical coordinates to allow for accurate representation of large modeled areas. The conservation equations for water mass, momentum (in three dimensions) and constituent mass (temperature [heat] and salinity) form the basis of the model, and are well established. It is assumed that the flow is incompressible, that the fluid is in hydrostatic balance,

the horizontal friction is not significant and the Boussinesq approximation applies, all customary assumptions.

The boundary conditions are as follows:

- At land, the normal component of velocity is zero.
- At open boundaries, the free surface elevation must be specified, and temperature and salinity specified on inflow.
- On outflow, temperature (heat) and salinity is advected out of the model domain.
- A bottom stress or a no slip condition is applied at the bottom. No temperature (heat) is assumed to transfer to or from the bottom, a conservative assumption as some transfer of hear to the bottom is expected to occur.
- A wind stress, and appropriate heat transfer terms, are applied at the surface.
- The surface heat balance includes all of the primary heat transfer mechanisms for environmental interaction, including evaporative and sensible heat exchange with the air just above the water surface, long wave radiation exchange between the water surface and the sky, and net short wave solar radiation between the loss due to reflection and the gain due to absorption at the water surface. Details of this surface heat transfer submodel are found in Appendix B.

There are various options for specification of vertical eddy viscosity, A_v, (for momentum) and vertical eddy diffusivity, D_v, (for constituent mass [temperature and salinity]). The simplest formulation is that both are constant, A_{vo} and D_{vo}, throughout the water column. They can also be functions of the local Richardson number, which, in turn, is a function of the vertical density gradient and vertical gradient of horizontal velocity. A more complex formulation adds the dependence on mixing length and turbulent energy and was chosen for use here to better simulate vertical momentum shear and thermal stratification. Details on turbulence closure formulations can be found in Appendix A.

The set of governing equations with dependent and independent variables transformed from spherical to curvilinear coordinates, in concert with the boundary conditions, is solved by a semi-implicit, split mode finite difference procedure (Swanson, 1986). The equations of motion are vertically integrated and, through simple algebraic manipulation, are recast in terms of a single Helmholtz equation in surface elevation. This equation is solved using a sparse matrix solution technique to predict the spatial distribution of surface elevation for each grid.

The vertically averaged velocity is then determined explicitly using the momentum equation. This step constitutes the external or vertically averaged mode. Deviations of the velocity field from this vertically averaged value are then calculated, using a tridiagonal matrix technique. The deviations are added to the vertically averaged values to obtain the vertical profile of velocity at each grid cell thereby generating the complete current patterns. This constitutes the internal mode. The methodology allows time steps based on the advective, rather than the gravity, wave speed as in conventional explicit finite difference methods, and therefore results in a computationally efficient solution procedure (Swanson, 1986; Swanson et al., 1989; Muin, 1993).

The environmental heat transfer model, (Mendelsohn, 1998) at the water surface contains a balance of the important terms governing the flow of heat, including:

- short wave solar radiation
- long wave atmospheric radiation
- long wave radiation emitted from the water surface

- convection (sensible) heat transfer between water and air
- evaporation (latent) heat transfer between water and air

A detailed description of the equations used for the environmental heat transfer model is given in Appendix B.

4.2. WQMAP System

ASA personnel have developed and applied many computer modeling tools. In conducting aquatic environmental analyses, ASA has developed a PC-based modeling system, which integrates geographic information (land use, watersheds, etc.), environmental data (water quality parameters, surface elevations and velocities, stream flows, bathymetry, etc.) and models (analytical and numerical, hydrodynamic, pollutant transport, etc.). The power of such a system, called WQMAP (Water Quality Mapping and Analysis Program) (Mendelsohn, et al., 1995), is that it allows the user to model and analyze many different scenarios efficiently. A graphical user interface simplifies user inputs and allows a graphical display of model output. In addition, one of the modeling components within ASA's WQMAP has been specifically developed for application to the study of thermal effluents in coastal waters, and widely used to undertake such analyses, including by regulators.

The geographic information component of WQMAP holds user-specified layers of data appropriate for and available to be used to address a specific task. For instance, in this instance such layers might include shorelines, intake locations, the discharge canal, monitoring data locations, etc. Each data layer can be easily input, either directly into WQMAP with a mouse and screen forms, or through import from existing geographic information system software. Data can be exported as well. Each layer can be displayed separately or in any combination. Graphics can be generated and displayed, either printed or stored for later use.

The environmental data component of WQMAP stores and displays actual environmental data, which are needed for analysis or used in model input or calibration. This component links to standard PC software, such as databases, spreadsheets, and data contouring packages. Importing to and exporting from other systems is also possible.

A suite of tools in WQMAP can be used to import, export and analyze environmental data. Time series of data at single or multiple stations can be imported, processed and displayed. Other measuring systems (e.g., moored current meters, sea surface radars, acoustic Doppler current profilers) can also be accessed and incorporated into the model.

4.3. WQMAP System Applications

The BFHYDRO model in WQMAP has been successfully used in many hydrodynamic and hydrothermal studies both in the U.S. and worldwide with results accepted by a variety of federal and state government agencies, including the following:

- U. S. Environmental Protection Agency
- U. S. National Oceanic and Atmospheric Administration
- U. S. Army Corps of Engineers
- U.S. Naval Oceanographic Office
- Massachusetts Department of Environmental Protection,
- Massachusetts Coastal Zone Management
- Rhode Island Department of Environmental Management
- Rhode Island Coastal Resources Management Council
- Vermont Agency of Natural Resources

- Connecticut Department of Environmental Protection
- New York State Department of Environmental Conservation
- South Carolina Department of Health and Environmental Control.
- The World Bank.

Examples where the model has been successfully applied to thermal plume applications include the following:

- Canal Station at Sandwich, MA (Swanson and Mendelsohn, 2000)
- Fore River Station at Weymouth, MA (EAI et al., 1998)
- RESCO Facility at Lynn, MA (Swanson and Isaji, 2001)
- Vermont Yankee at Vernon, VT (Swanson et al., 2004)
- Brayton Point Station at Somerset, MA(Swanson et al., 2006; Swanson et al., 1998)
- Arabian Gulf (Shahriar et al., 2003)
- Ras Tanura Integrated Project, Ras Tanura, Saudi Arabia (Crowley and Mendelsohn, 2010).

ASA is also presently modeling the discharge canal for the Brayton Point Station in Somerset, MA and the Merrimack Station discharge into the Merrimack River in support of permit renewals.

5. Model Application to the Hudson River

The model application to the Hudson River requires defining the spatial extent and resolution of the model grid, generating a bathymetric data file for the grid, and creating boundary forcing files. Furthermore, model parameters suitable to the application area are chosen and then model simulations for the period of interest, either calibration or some critical scenario, are run. These elements of the model application are defined in the following sections.

5.1. Grid Generation

The first step in generating a boundary-fitted grid, using WQGRID, is to define the study area of interest, e.g., a portion of the Hudson River estuary in the vicinity of Indian Point. Experience with previous model applications indicates that open boundaries ideally are located away from the specific area of interest at locations where forcing data exist. This principle suggests that the model boundaries be located at the northern and southern extents of the Hudson River, although the focus of the analysis is in the vicinity of Indian Point. Considering these factors, the boundaries for the model application are Hastings on Hudson (a USGS station) for the southern boundary, and the dam at Troy for the northern boundary. The choice of the southern boundary at Hastings on Hudson is also influenced by the desire to be north of complicating tidal River connections, like the Harlem River. The northern boundary was forced with River flow from observations at the USGS Lock 1 station, with water temperature based on observations at the USGS Albany station, and the southern boundary was forced based on water surface elevation, temperature and salinity observations at the USGS Hastings on Hudson station. Based on knowledge of the complex dynamics of the Hudson River estuary and the need to simulate the vertical structure in the River, the model grid is a three dimensional representation of the water column with a sigma coordinate system in the vertical dimension. This means that, for every grid cell defined by lateral and longitudinal coordinates, the vertical water column is split in to an equal number of layers, which for this application was 11 layers.

The WQGRID component of WQMAP consists of a set of tools to generate a boundary fitted grid. The grid is specified by locating grid points along shorelines and bathymetric features. Each point has assigned grid counters to keep track of how each grid point relates to its neighbors. The grid spacing in the domain is roughly determined by grid spacing at land boundaries. Finer grid resolution is specified for increased model results resolution of the thermal discharge from IPEC. Once the boundary grid points along the shoreline have been specified, and any interior bathymetric feature grid points located, the gridding model generates all the remaining interior points. These points are constrained to obey a Poisson equation, and their locations are solved iteratively by a Poisson solver. Technical details can be found in the WQMAP User's Manual (ASA, 1996).

Figure 5-1 shows the model grid. In this application, the full grid covers a 130-mile span of the River from Hastings on Hudson, approximately 20 miles north of the Battery, to the dam upstream at Troy, with 4,719 water grid cells in each of 11 layers for a total of 51,909 grid cells. The grid resolution ranges in size with larger cells located furthest from the plant up to 6,000 ft in length while the grid is finer (165 ft ×165 ft) in the area near the IPEC discharge to better resolve the circulation and thermal structure there. The grid cell size upstream and downstream from the IPEC is purposely larger to minimize the model computations required, while still providing accurate predictions. This number of grid cells and cell resolution is more than adequate for this application.

In general, the grid aspect ratio reflects *a priori* estimates of expected flows. This means that the longer grid dimension, if any, is oriented along the major axis of the flow. This approach is

necessary because the hydrodynamic model has inherent time step restrictions based on the ratio of grid size to flow speed. Faster model runs are possible when the grid is optimized in this manner.

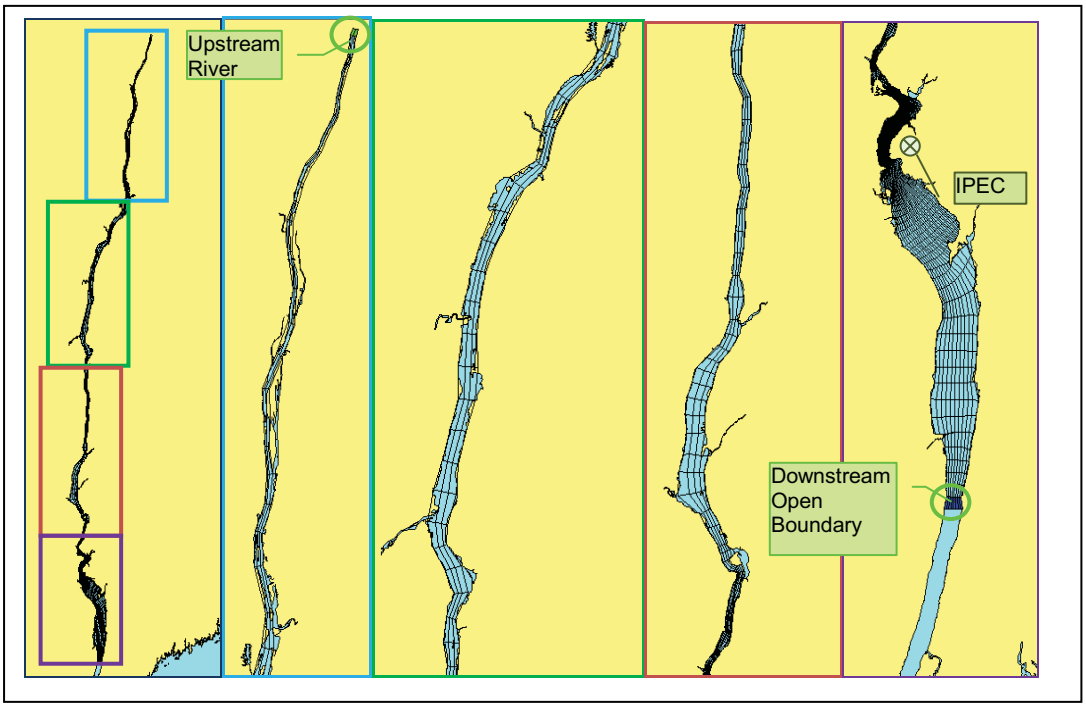

Figure 5-1 Model grid for the IPEC study area: Blue shaded cells represent the open boundary at Hastings and the green shaded cells represent the upstream river boundary at Troy

5.2. Bathymetry

A depth value must be assigned to each cell in the model grid. Two data sources of bathymetric soundings, including sounding coordinates and water depth, were used to create the array of grid depths: (1) the National Ocean Service (NOS), which maintains a database of various surveys and had a combination of surveys that covered the entire extent of the model grid; and (2) a localized survey performed for the IPEC by Hudson Engineers (2009) as part of a survey of the IPEC intakes. The two datasets showed the bathymetry was consistently measured with the Hudson Engineers survey more highly resolving the depth in the local area near the intakes. Each grid cell was automatically assigned a depth value by interpolation from the data, based on a distance-weighting algorithm for soundings close to the grid location. Once the bathymetric measurements were applied, the WQGRID result was generated.

Figure 5-2 shows a plan view of both the model grid and the resulting model bathymetry in the vicinity of IPEC. The River depths increase with distance from the shoreline, with most River cross sections with a maximum depth less than (35 ft) The River generally is shallow at the northern and southern extremes and has deep pockets (> 65 ft) starting approximately 3 miles south and as far as 15 miles north of the IPEC; however, within that 18-mile stretch, there is an area just south of IPEC for approximately a mile and a half where the depths are slightly more shallow (~50 ft). The northern shoreline of IPEC, located on the eastern side of the Hudson, drops off quickly, reaching depths of (65 ft) within the first couple of hundred feet from the shore.

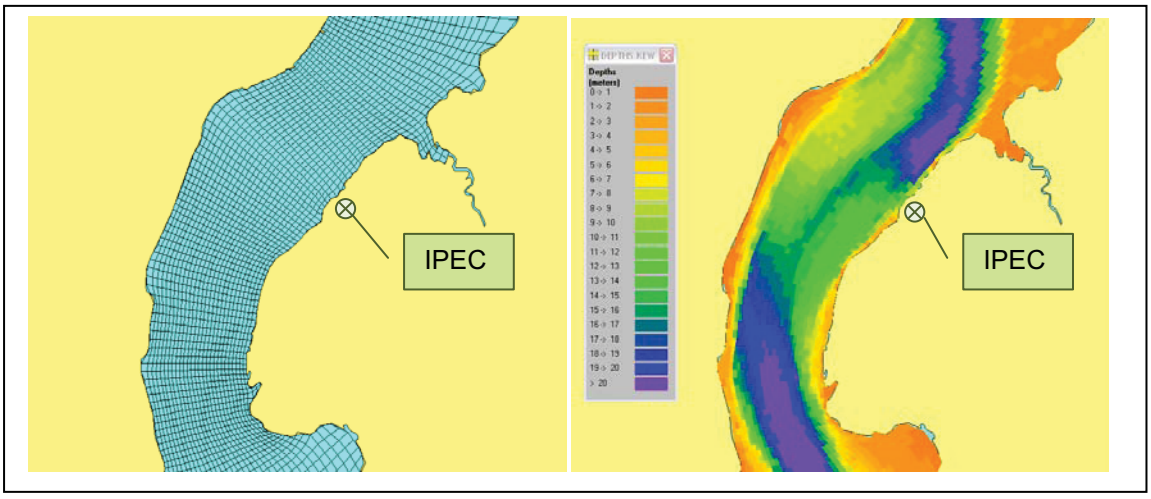

Figure 5-2 Model grid (let) and grid bathymetry (right) in the region closest to IPEC within the study domain.

5.3. Boundary Conditions

The 11-layer, 3-dimensional boundary fitted hydrodynamic model (BFHYDRO) employed to determine the circulation and thermal distribution requires a set of boundary forcing conditions for each step. River flow, water surface elevation, temperature, salinity and winds are major forcing functions important in driving the circulation, while solar radiation and auxiliary parameters, such as air and dew point temperature, relative humidity and pressure, play an important role in determining the thermal field.

The model was forced at its open boundaries which include the lower River boundary at Hastings-on-Hudson, the upper River boundary at Troy (Lock 1), the water-air boundary at the River surface, and necessarily the thermal discharges into the River. Figure 5-3 shows the Hudson River from Hastings-on-Hudson to Green Island, along with USGS stations at Hastings-on-Hudson, West Point, Poughkeepsie, Albany, and Green Island; the Danskammer, Roseton, Indian Point and Bowline power plants; and the White Plains Airport. The model forcing changes with time, as the tides, water temperature, River flow and meteorological conditions change. Water surface elevation, water temperature and salinity observed at the USGS Hastings on Hudson station were used as the downstream River boundary, and flow observed at Lock 1 was used with the water temperature at the Albany Station, located 8miles downstream from Lock 1, specified at the upstream River boundary. The forcing for the calibration period and model scenario period are described separately in Chapter 6 and Chapter 7 respectively.

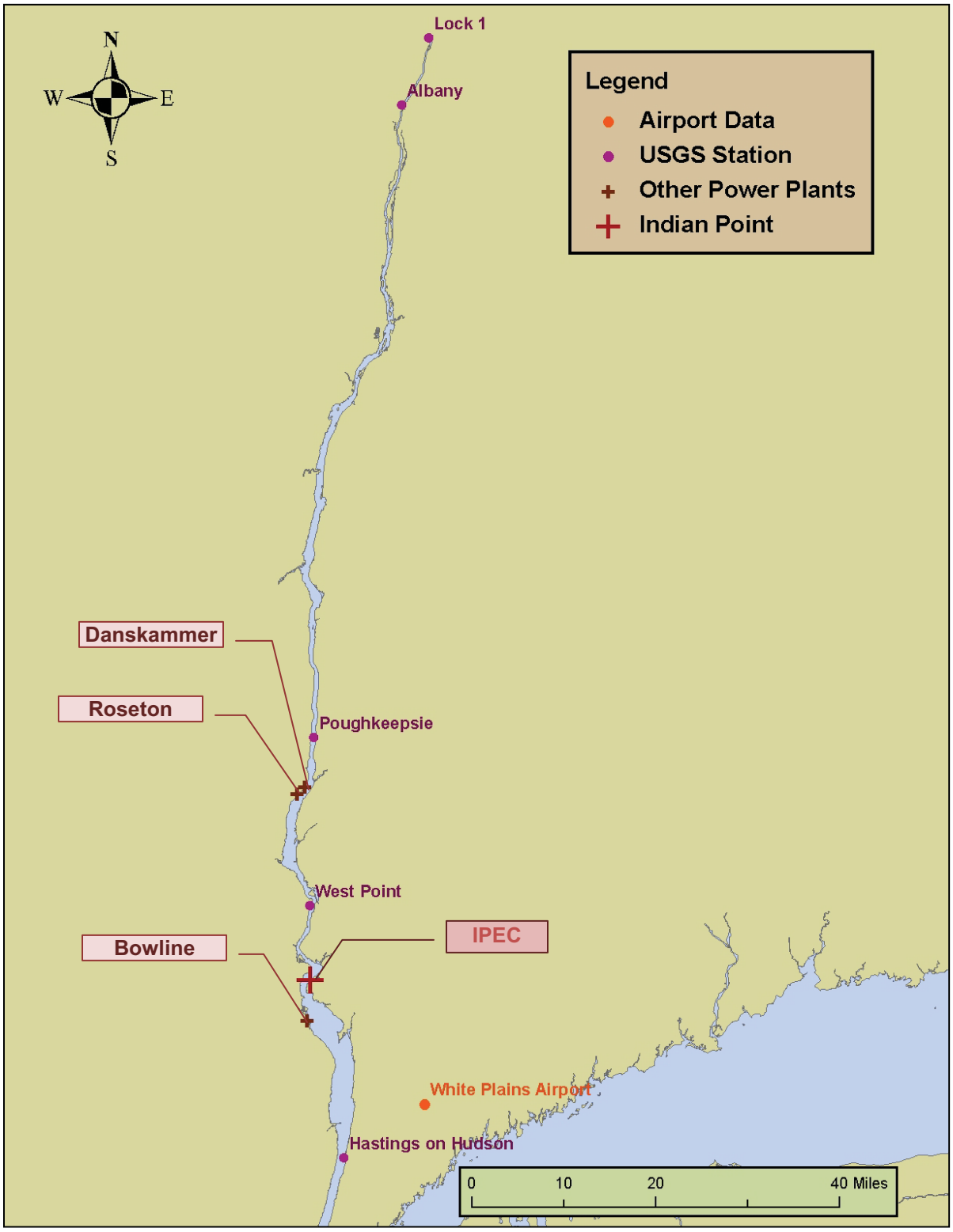

Figure 5-3 Model domain in the Hudson River showing locations of data sources.

6. Model Calibration

The period chosen for the model calibration was based on the timing of available high resolution measurements of water temperature and River currents obtained near the plant through the Field Program carried out in 2009. During this period, 24 September through 3 November, River measurements from all instruments (moored thermistors and Acoustic Doppler Current Profilers [ADCPs]) were available. Also available during this period were lower resolution data from various USGS River stations located both north and south of IPEC, as well as nearby meteorological observations. The USGS data included water surface elevation, temperature and salinity at Hastings, West Point and Poughkeepsie, water surface elevation and temperature at Albany and River flow at the Lock 1 station near Troy.

6.1. Model Forcing

The period chosen for the model calibration was a portion of the 2009 time period over which in-River measurements from all instruments (thermistors and Acoustic Doppler Current Profilers [ADCPs]) were available: 24 September though 8 October. The model was driven at its open boundaries, which include the lower River boundary at Hastings on Hudson, the upper River boundary at Troy (Lock1), the water-air boundary at the River surface, and the plant thermal discharges along the River. Figure 6-1 shows the Hudson River from Hastings-on Hudson to Troy, along with USGS stations at Hastings on Hudson, West Point, Poughkeepsie, Albany, and Green Island; the Danskammer, Roseton, Indian Point and Bowline power plants; and the White Plains Airport. The data used to drive the model at each boundary is described in the following sections.

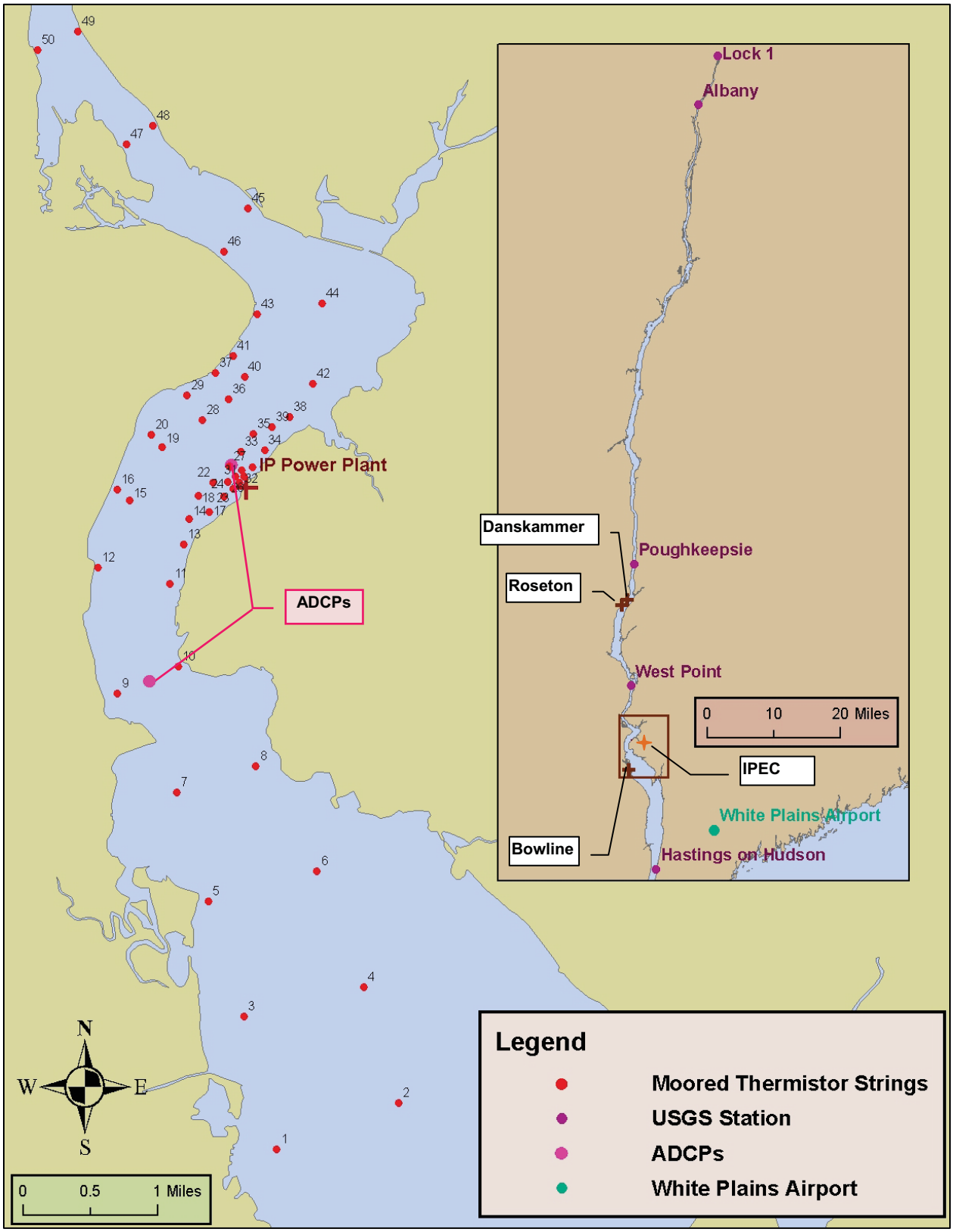

Figure 6-1 Illustration of Data Observation Locations.

6.1.1. Lower River Boundary at Hastings-on-Hudson

The downstream open boundary forcing used available USGS collected data at Hastings-on-Hudson. The site, designated as 01376304, measured water level, as well as temperature and conductivity at a depth of 10 ft. Data was acquired at 15-min intervals and was processed by hourly averaging, and subsampled to the hour. The conductivity was converted to salinity using the relationship developed empirically by NAI (Texas Instruments, 1976). While other model forcing factors were applied at one hour time steps the lower river boundary forcings were applied at a 15 minute time step; given that surface elevation can change relatively significantly within an hour this method ensures that the minimum and maximum surface elevations are more accurately represented. Figure 6-2 shows the time history over the calibration period of water level, temperature and salinity at the lower River boundary at Hastings-on Hudson.

The elevation or water level clearly indicates tidal influence at this location in the Hudson River. Generally or typically, the tide oscillates with a 12.42 period (M2 tidal constituent). The tidal range changes over the 14-day spring-neap cycle with neap (smaller) tide ranges occurring around 25 to 27 September, 10 to 12 October (not shown well due to larger than usual neap – requires clarification), and 24 to 26 October. The tidal range varies between 2.2 and 5.1 ft during the calibration period.

Since ocean salinity averages 33 psu in the New York Bight (Gordon and Aikman, 1981), the salinity at Hastings-on-Hudson varies somewhere between this value and the freshwater value of 0 psu. During the period of the field program, the salinity varied between 4.1 and 14.8 psu on a tidal frequency at the measurement depth of 10 ft.

The River temperature is cooling during this period, from 72.5 °F on 24 September to 56 °F around 19 October and relatively constant (between 56 and 59 °F) through 3 November at the 10-ft measurement depth. The tidal-induced variation is not significant.

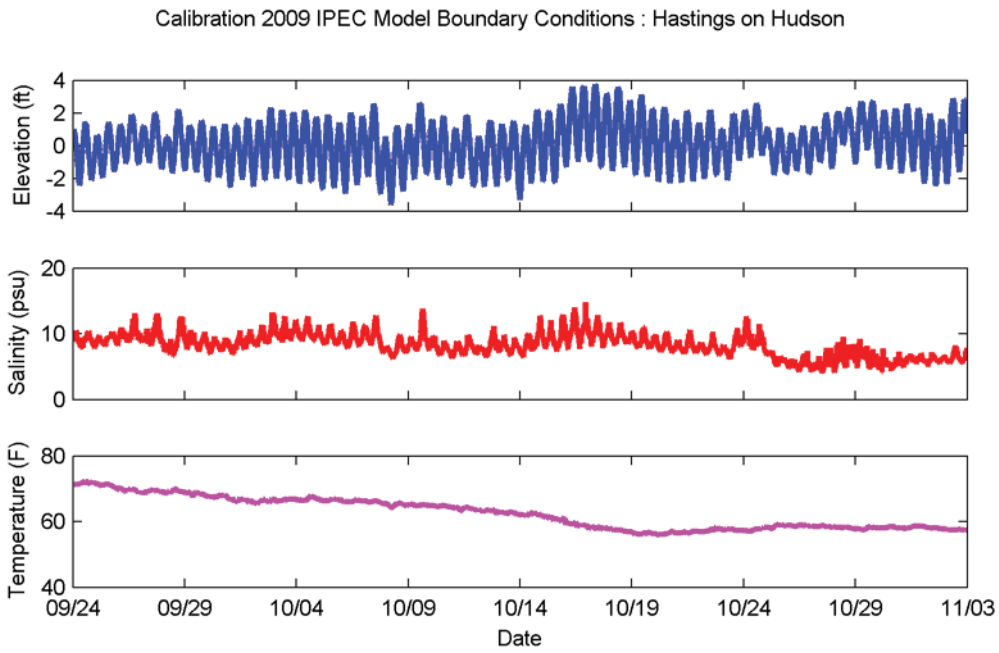

Figure 6-2 USGS water level, temperature and salinity for the calibration period from 24 September to 3 November 2009 measured at Hastings.

6.1.2. Upper River Boundary at Troy

The upstream open boundary forcing used available USGS collected data at two adjacent sites near the dam in Troy. The Green Island site, designated as 01358000, provided River flowrate data, while Albany, designated as 01359139, provided water temperature (salinity was zero), both at 10-ft depths below the surface. A regression between Green Island and Esopus Creek (01362500) was developed to fill data gaps in the Green Island data. Data was provided at 15-min intervals and was processed to hourly averages and subsampled to the hour. Figure 6-3 shows the time history over the calibration period of flowrate and temperature.

River flow is relatively low during the period, ranging between 1,900 and 11,550 cfs before 24 October, and then rising to a maximum of 20,125 cfs on 25 October, before dropping off to 7,700 cfs by the end of the period. River temperature tracks the same variation as seen in the Hastings-on-Hudson, although with slightly lower temperatures (68.5 °F on 24 September, 49.5 °F on 19 October, and 49 - 52.5 °F through 3 November).

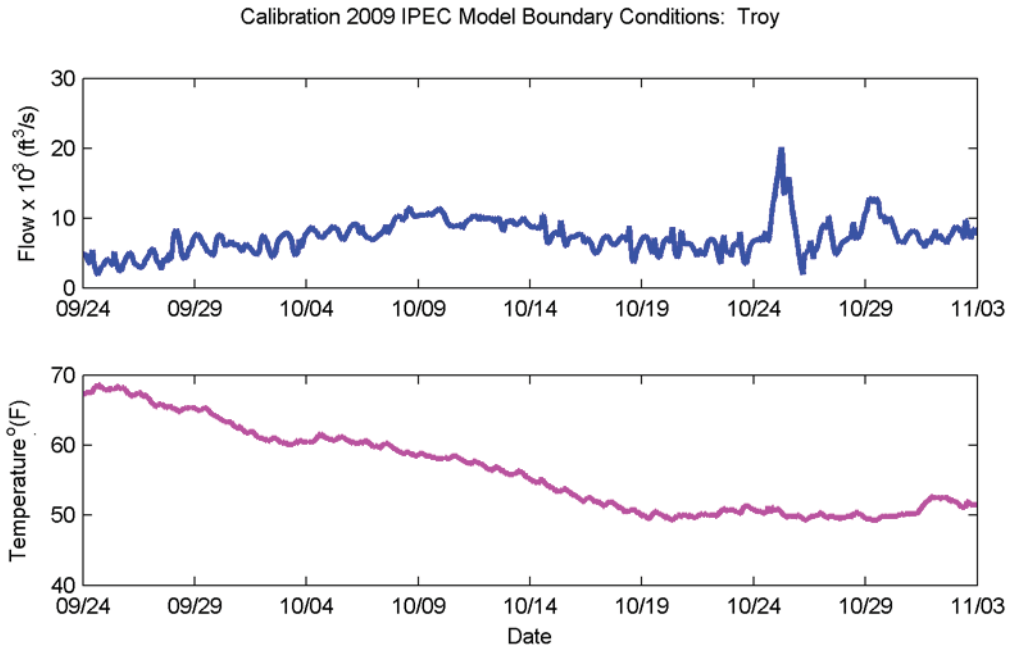

Figure 6-3 USGS flowrate and temperature for the calibration period from 24 September to 3 November 2009 measured at Lock 1 and Albany.

6.1.3. Meteorological Conditions

The meteorological variables used in the model were those from the White Plains Airport (HPN). The data consisted of air temperature, dew point, relative humidity, wind speed and direction, pressure and radiation. Figure 6-4 shows the time history of these variables during the calibration period.

The air temperature was relatively constant during this period, typically within a range of 44 to 62 °F. The dew point tracked the air temperature relatively closely, although typically 3 to 16 F cooler. The relative humidity varied from 28 to 97% with periodicities of 1 to 3 days.

The wind is shown as a vector with its length scaled to the speed and its direction pointing downwind (oceanographic convention). Peak speeds of 27 mph heading south southeast occurred on 7 October.

Atmospheric pressure varies between 983 and 1014 mbar with a 1 to 3 day period. Solar radiation peaks at 683 W/m^2 on 25 September with the peaks slightly diminishing further into the period.

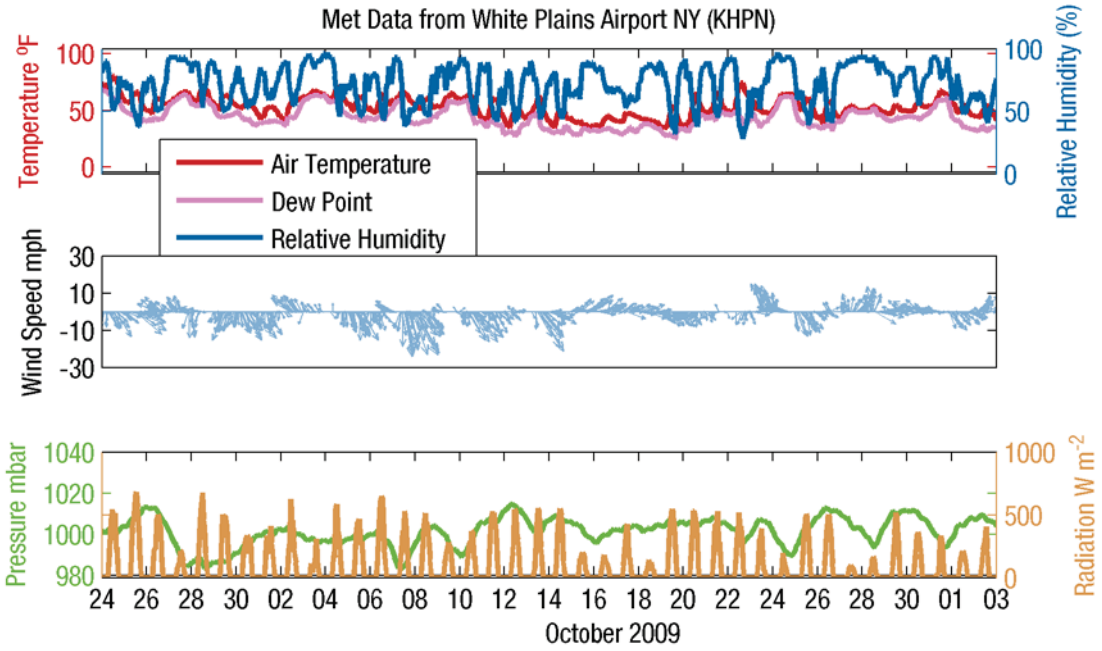

Figure 6-4 NRCC meteorological data for the calibration period from 24 September to 3 November 2009 measured at the White Plains Airport.

6.1.4. Plant Thermal Discharges

6.1.4.1 IPEC Operations

Flow and temperature records were provided by IPEC describing their operations during the calibration period. Figure 6-5 shows the time history of cooling water flow, intake and discharge temperature, and the calculated rejected heat. The rejected heat calculation was based on the temperature difference between discharge and intake temperatures and the cooling water flow.

IPEC operated at a relatively consistent flow of approximately 1700 Kgpm from 24 September through 14 October, and then gradually reduced flow to 1500 Kgpm by 27 October. Discharge temperature dropped over the period from 92°F to 70°F, and intake temperature dropped from 74°F to 58°F. The heat rejected to the cooling water system averaged about 4400 MW from 24 September to 29 September and then gradually rose to 5200 MW before dropping to 2600 MW on late 2 November.

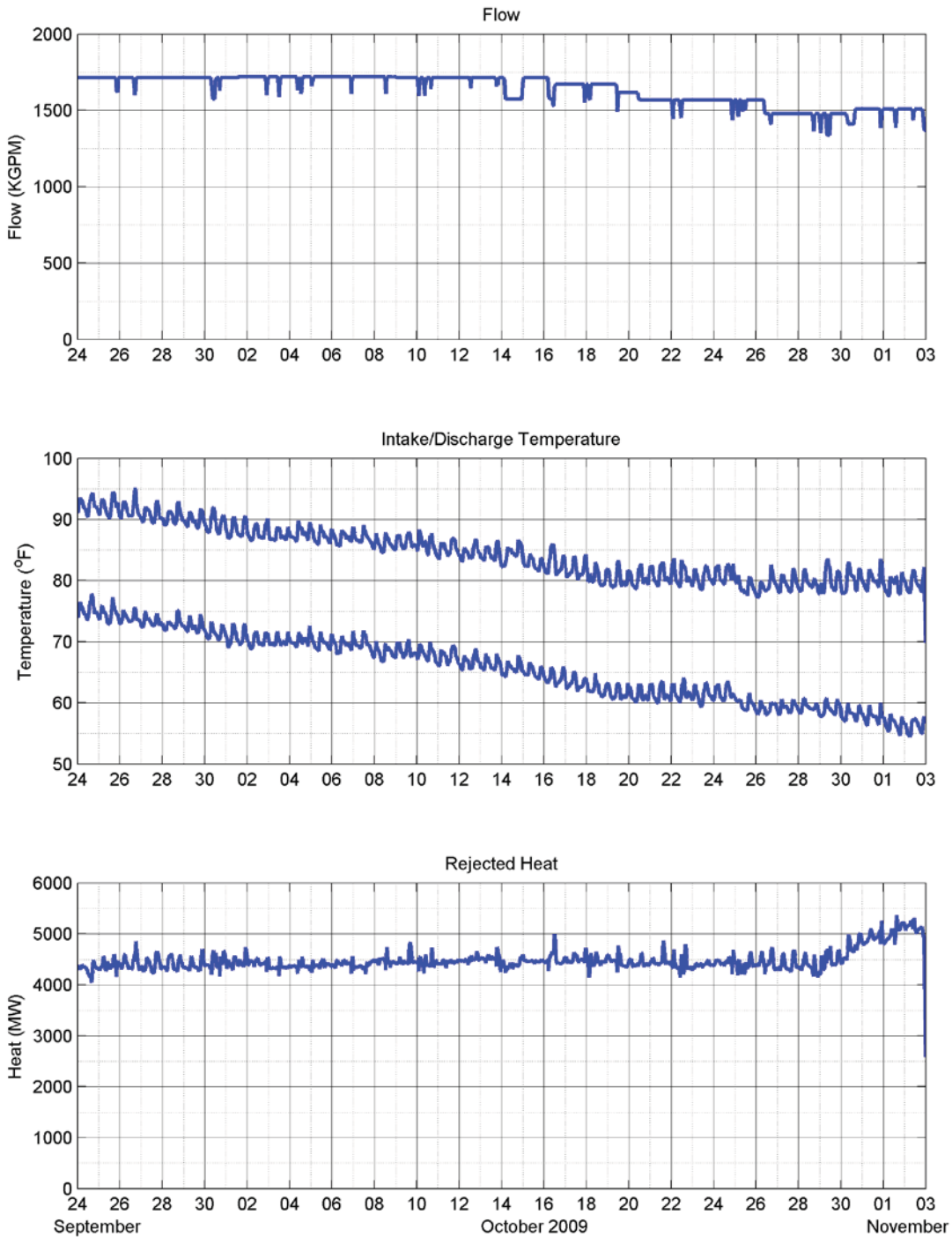

Figure 6-5 IPEC operations (discharge flow and temperatures) with computed rejected heat for the calibration period from 24 September to 3 November 2009.

6.1.4.2 Other Plant Operations

Daily flow and temperature records for the Roseton and Danskammer Generating Plants were provided by Dynegy as part of their Daily Operating Reports for the September through November 2009 period. Figure 6-6 and Figure 6-7 show the time history of cooling water flow, intake and

discharge temperature and the calculated rejected heat for the Roseton and Danskammer plants, respectively. The rejected heat calculation was based on the flow and temperature difference between discharge temperature and intake temperature.

The operation at Roseton (Figure 6-6) generated less electricity and therefore less rejected heat than IPEC during the calibration period. Plant operation was intermittent during this period as well. The maximum flow was approximately 9 Kgpm and the temperature rise was typically less than 4 °F. This resulted in about 5 MW of rejected heat that occurred twice during the calibration period lasting from 1 to 3 days.

The operation at Danskammer (Figure 6-7) generated slightly more electricity than Roseton, but therefore rejected less heat than IPEC during the calibration period. Plant operation was continuous but variable during this period. The flow varied from2 to 6 Kgpm and the temperature rise was varied from 10 to 27 °F. This resulted in between 5 and 20 MW of rejected heat.

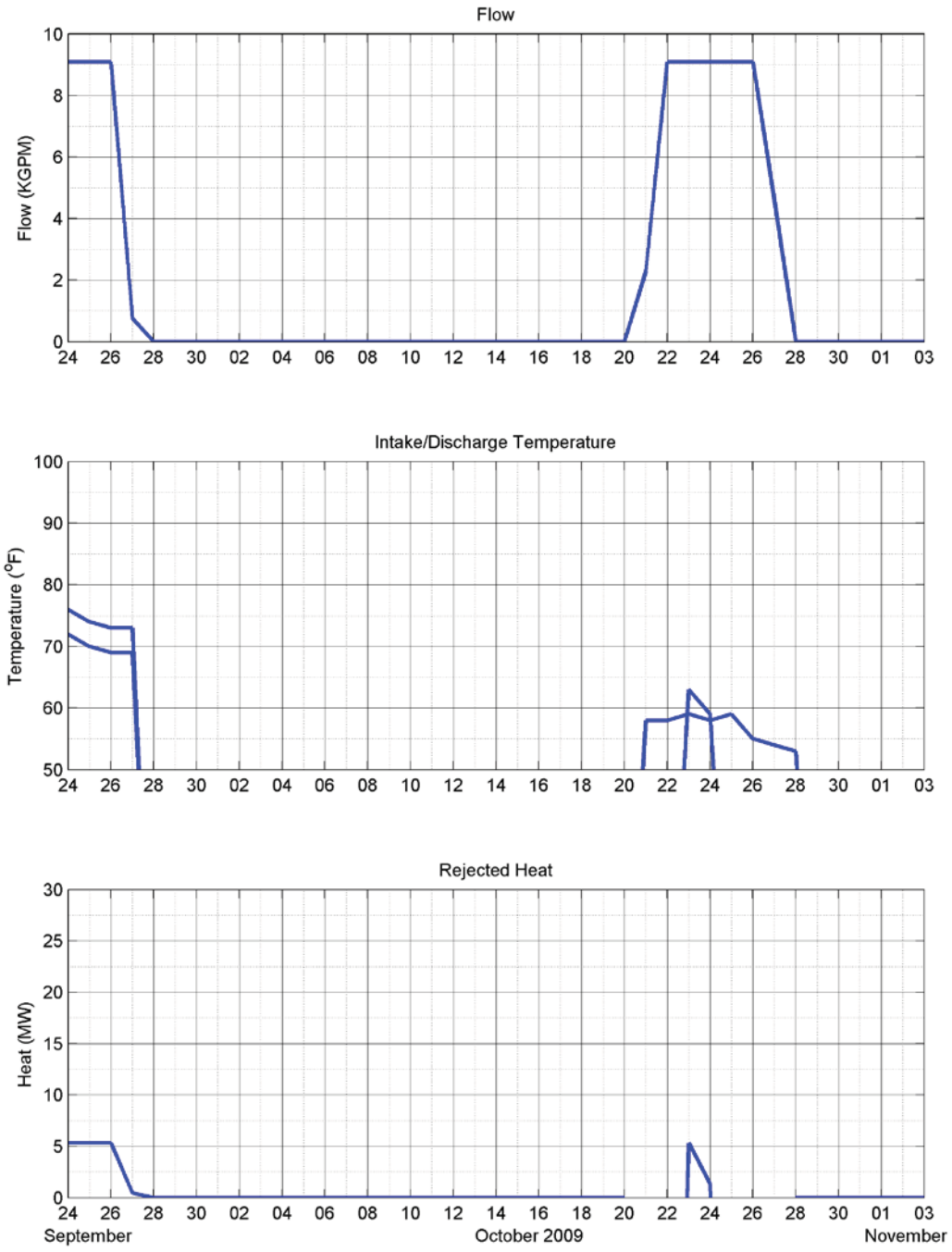

Figure 6-6 Roseton Generating Plant operations(discharge flow and temperature) with computed rejected heat for the calibration period from 24 September to 3 November 2009.

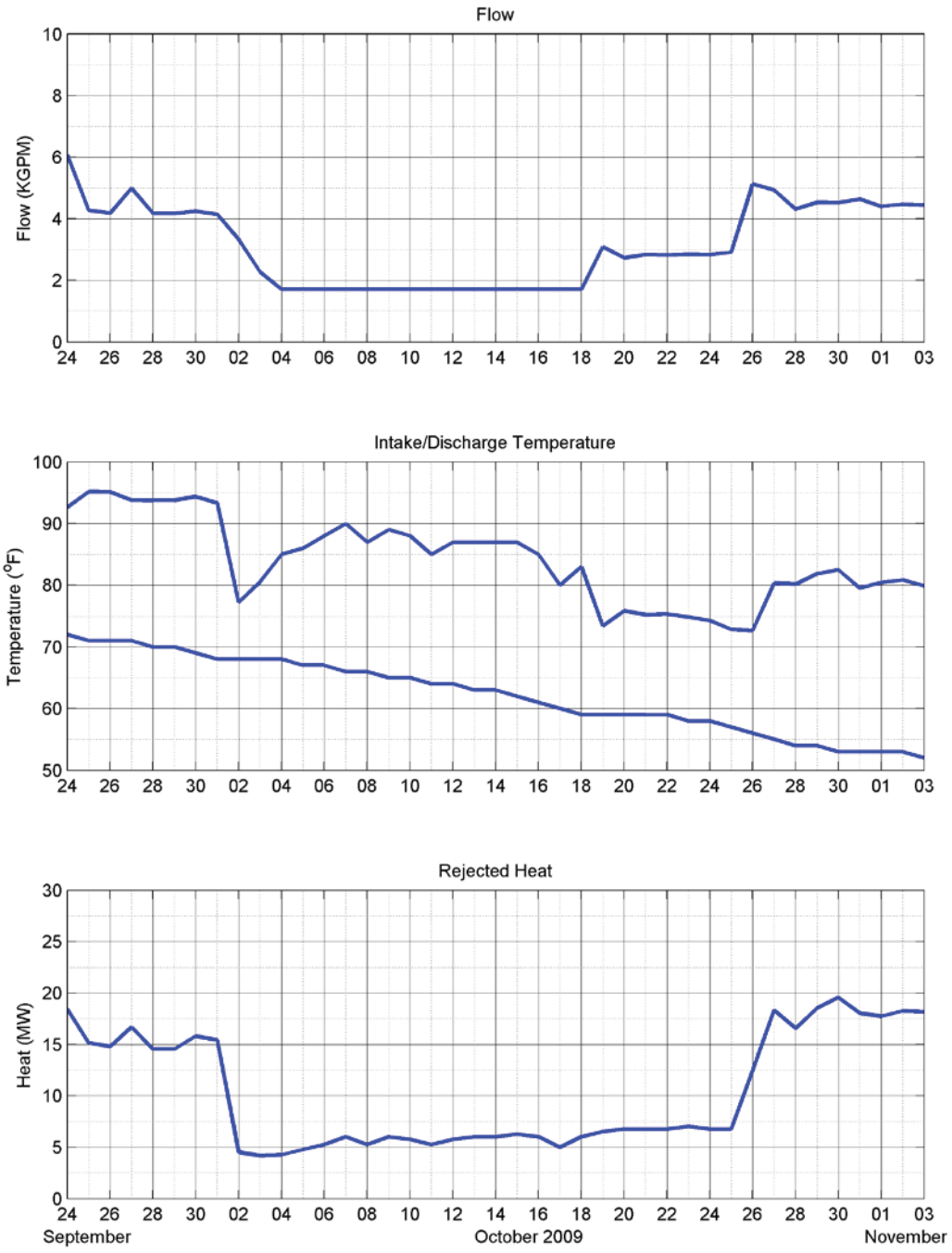

Figure 6-7 Danskammer Generating Plant operations (discharge flow and temperature) with computed rejected heat for the calibration period from 24 September to 3 November 2009.

Bowline Generating Station was not in operation during the calibration period (Mark Mattson, personal communication).

6.2. Calibration Procedute

For the calibration effort, a total of over 100 model runs were executed to determine the sensitivity of the model to variations in model parameters and find the set that gave the best model results in comparison with observations. The resulting hydrodynamic model parameters ultimately chosen included a Mannings n of 0.03 for Chezy formulation of bottom friction and a turbulence closure model for vertical eddy viscosity and diffusivity. The horizontal eddy diffusivity for temperature were 21 ft2/s. The net surface heat fluxes were computed using observed solar radiation and other environmental parameters (air temperature, dew point temperature, winds and relative humidity). These hydrodynamic and temperature parameters were selected to minimize the difference between model predictions and observations, using the qualitative and quantitative evaluation metrics described below. The purpose of the qualitative comparison is to evaluate how well the model performed from a visual, but subjective perspective. The purpose of the quantitative comparison is to evaluate model performance based on objective statistical measures. In both approaches the analysis involved a comparison of model predictions to measurements or observations from the period, which include the moored thermistors strings measuring water temperature along the water column, ADCPs measuring water pressure (proxy for surface elevation) and currents, and USGS stations which collect either water surface elevation, water temperature and salinity or river flow. The location of these stations and with a key to identifying available data sources is shown in Figure 6-1.

6.2.1. Qualitative Comparisons

The comparison of model results and observations depends on data dimensionality. For example, a time series of data collected at a particular site can be plotted together with model output to provide a visual comparison. This comparison can provide information on the suitability of the model to simulate the range of variability evident in the observations.

The most direct way to provide a qualitative comparison is to plot the model predictions and the observed data for each variable over the time of the simulation. This can be done with time series plots of the variables of interest or contour plots when looking at spatially varying patterns.

6.2.2. Quantitative Comparisons

Quantitative comparisons are statistical measures that can be applied to the model predictions and field data sets that provide a numerical assessment of the comparison. These statistical measures can be grouped into two major components: those measures that describe an individual set of data (e.g., a time series of one variable), and those that relate the degree of difference (error) between two data sets (e.g. time series of model predictions and field observations). Individual statistical measures include the mean, standard deviation, percentiles, minimum, and maximum. The independent variable can be time, depth or distance in these data. The quantitative comparisons between data sets include relative error, root mean square error, linear regression, comparison of means and correlation coefficient. McCutcheon et al (1990) describes these quantitative comparisons in detail, and provide guidance on acceptable values. Each statistical measure used in this analysis is briefly discussed below.

6.2.2.1 Relative Mean Error (RME)

The relative error measures the difference between calculated and observed mean values and can be defined in a variety of ways. The relative mean error is the relative difference of the means

$$rme = \frac{\bar{x} - \bar{c}}{29\bar{x}}$$

where $\bar{x}$ is the mean of the observation values and $\bar{c}$ is the mean of the model-predicted or calculated values. Evaluation of this statistic over space and time can be made to provide a cumulative frequency of error (median error, percentile exceedances). The relative error is expressed as a percentage. This statistic can be unreliable for small values of the mean, and does not provide information on the variability in the data, but can be a useful indicator for general model performance.

6.2.2.2 Error Coefficient of Variation (ECV)

The error coefficient of variation is the ratio of the root mean square error to the mean. It is defined as:
and expressed as a percentage.

$$ecv = \frac{1}{\bar{x}}\sqrt{\frac{\Sigma(x_i - c_i)^2}{N}}$$

6.2.2.3 Square of Correlation Coefficient (r2)

The correlation coefficient (r) relates to the linear interdependence of the predictions to observations. It is defined as the ratio of the covariance and the standard deviations of predicted and observed values.

$$r_{xy} = \frac{\sum_{i=1}^{n}(x_i - \bar{x})(y_i - \bar{y})}{(n-1)s_x s_y},$$

where x and y are the sample means of X and Y, s_x and s_y are the sample standard deviations of X, the observations, and Y, the predictions. The squared correlation coefficient is the square of r, and lies between -1 and 1. A value of zero indicates no correlation between two observations and predictions, 1 represents perfect positive correlation and -1 implies perfect negative correlation.

The USEPA has published guidance on the acceptable statistical measure values for model calibration/confirmation (McCutcheon et al., 1990). Table 6-1 shows a summary of the guidance for different measures and properties. The statistical measures have been defined above, and the properties include flow and temperature. There is a unique value presented for each property. McCutcheon, et al. (1990) state that these guidance values are representative of a mean level of calibration/confirmation among multiple comparisons, and are not to be considered an upper limit (RME, ECV) or lower limit (r^2) for individual comparisons.

Table 6-1 Model calibration guidance (McCutcheon et al., 1990).

Error Measure	Property	Value
Relative Mean Error, RME	Elevation, Velocity	±30%
	Temperature	±25%
Error Coefficient of Variation, ECV	Elevation, Velocity	10%
	Temperature	45%
Squared Correlation Coefficient, r^2	Elevation, Velocity	0.94
	Temperature	0.84

6.2.2.4 Skill

Another measure of the quantitative comparison between model predictions and observations is skill (Wilmott, 1981)

$$Skill = 1 - \frac{\Sigma |X_{model} - X_{obs}|^2}{\Sigma (|X_{model} - \overline{X_{obs}}| + |X_{obs} - \overline{X_{obs}}|)^2}$$

A skill value of 1 indicates perfect agreement, and 0 indicates complete disagreement. This measure was recently used in a ROMS model application to the Hudson by Warner et al. (2005) that assessed the performance of the model in resolving the temporal variations from an extensive field data set. They report a skill level of 0.85 to 0.95 for water level, 0.92 for velocity (depth averaged), and 0.85 for salinity (taken here as a proxy for temperature). The approach was used more recently by Ralston et al. (2008) to evaluate salinity stratification and residual velocity in the River.

6.3. Calibration Results

The primary focus of the calibration process is to adjust appropriate model parameters to optimize the comparison to a data set of observations. The parameters, as discussed in the previous sections, include bottom friction, horizontal and vertical dispersion, and atmospheric exchange rates. The observed data used for the model calibration are time series of water level (surface elevation) from USGS stations and ADCPs from the field program, current velocities from ADCPs and temperatures from selected thermistors deployed as part of the field program.

The first 13 days of the calibration period, from 25 September through 8 October, was selected since that period had warmer water temperatures than the later portion to highlight model performance under more extreme environmental conditions and included a complete spring-neap tidal cycle.

6.3.1. Water Level Comparison

The observed data used for the model calibration are time series of water level (surface elevation) from the USGS stations at West Point, Poughkeepsie, and Albany as well as the from the two deployed ADCPs at Indian Point and Stony Point; note however that the measurements at the ADCPs are not corrected for atmospheric pressure. Results are shown in Figure 6-8 and Figure 6-9.

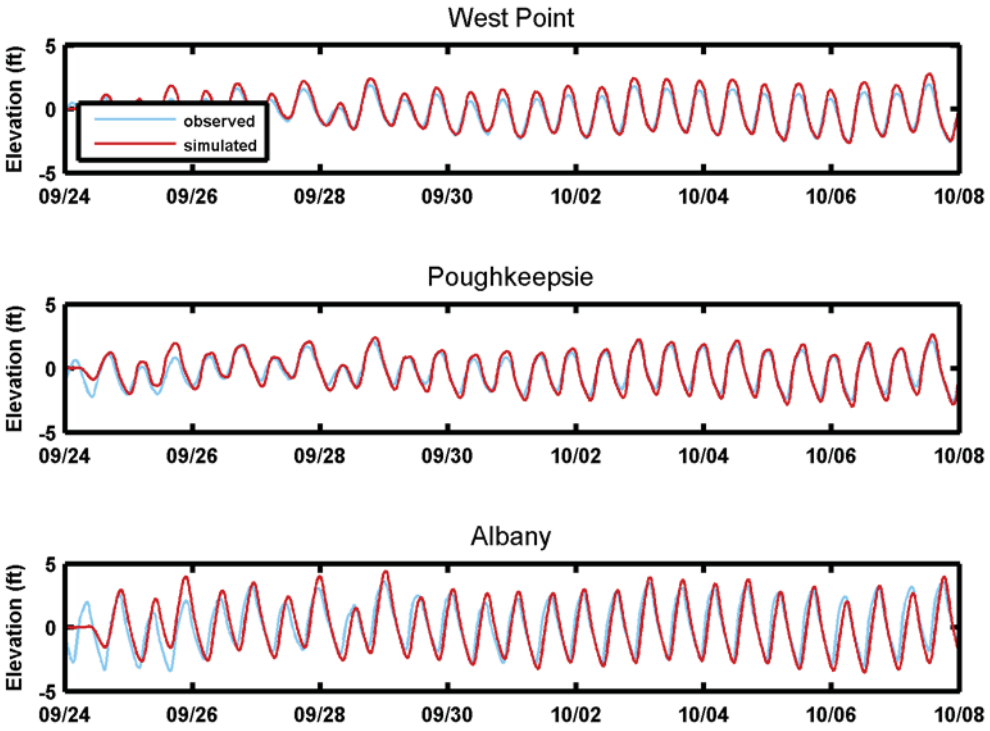

Figure 6-8 Water level comparison between model predictions and observations for the calibration period from 24 September to 8 October 2009 for West Point (top) Poughkeepsie (middle) and Albany (bottom).

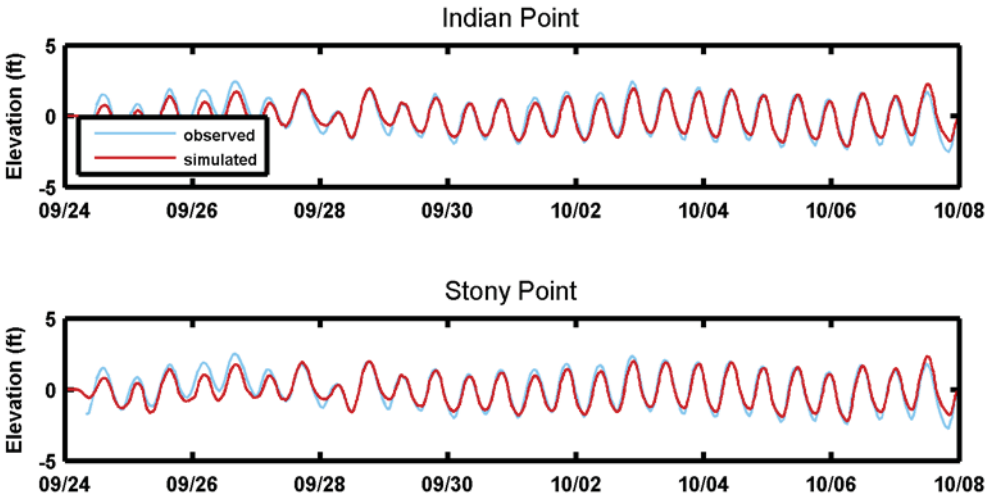

Figure 6-9 Water level comparison between model predictions and observations for the calibration period from 24 September to 8 October 2009 for Albany, Indian Point ADCP and Stony Point ADCP

The model simulates the tide range and phase well, as illustrated in the above Figures. Table 6-2 summarizes the maximum observed and simulated tide range at each of the stations. The model does slightly over predict tidal amplitude (and therefore) range in a non significant fashion. The model does track the observed trend of amplified tidal amplitude in the northern portion of the River increasing from West Point to Albany.

Table 6-2 Summary of maximum tide range at USGS and ADCP locations for the calibration period from 24 September to 8 October 2009.

Station	Observed Maximum Range (ft)	Predicted Maximum Range (ft)
West Point	4.4	5.0
Poughkeepsie	4.6	5.3
Albany	6.9	7.8
Indian Point	4.8	4.0
Stony Point	4.8	4.2

Table 6-3 summarizes the quantitative calibration measures for the USGS and ADCP locations. For surface elevation statistical calculations of RME and ECV the mean was assumed equal to the tidal range to make them a useful measure of variance, otherwise the mean would be approximately zero as tide ranges oscillate close to zero.

Table 6-3 Quantitative comparisons of predicted and observed tidal range at USGS and ADCP locations for the calibration period from 24 September to 8 October 2009.

Station	r^2	RME	ECV	Skill
West Point	0.94	5	10	0.97
Poughkeepsie	0.94	1	9	0.97
Albany	0.76	1	14	0.93
Indian Point	0.92	3	7	0.97
Stony Point	0.92	3	7	0.98
Average	0.90	3	9	0.96
Guidance	**0.94**	**±30%**	**10%**	**0.850.95**

The results show that the model performs well in all locations, although it does less well at Albany than at any of the other locations. This differential at Albany is not significant here, since that station is far removed from the area of the River of concern for this study. Discounting the Albany results raises the average r^2 to 0.93, , generally commensurate with the recommended guidance. The average ECV and RME fall within the guidance level and the Skill is better than the other Hudson River model results (Warner et al., 2005), even when the Albany comparison is retained.

6.3.2. Flow Comparisons

Two ADCPs were deployed during the field program, one near Indian Point (IP) and a second near Stony Point (SP) (Figure 6-1). The current velocities recorded from the ADCPs were rotated to along-River direction to more clearly show that most of the flow travels in the up and downstream directions. The IP ADCP data were rotated 45 degrees east of north while the SP data were rotated 30 degrees west of north. Figure 6-10 shows the time series of current velocities at the surface and bottom layers, respectively, at Indian Point while Figure 6-11 shows the time series of current velocities at the surface and bottom layers, respectively, at Stony Point.

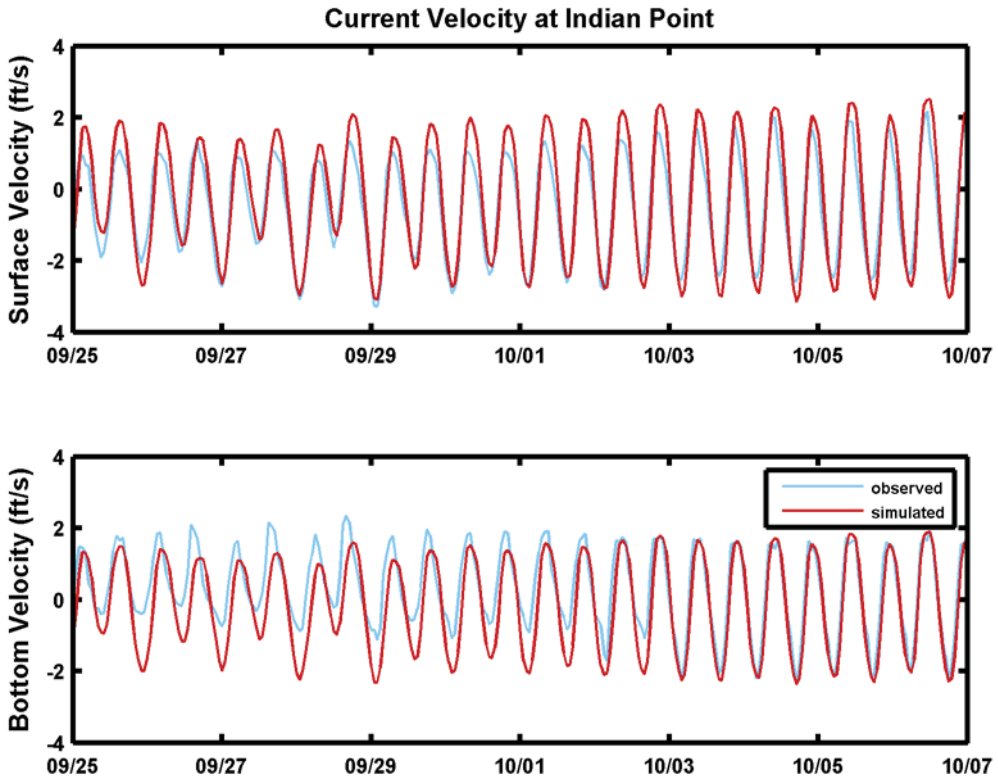

Figure 6-10 Surface (top) and bottom (bottom) current comparison between model predictions and observations for the calibration period from 24 September to 8 October 2009 at Indian Point.

The surface currents show the strong tidal variation moving up and down with the period of 12.42 hours. In addition, the simulated results captured bi-weekly spring-neap tide as well as diurnal inequality in successful manner. The simulated flow is slightly larger than the observations. The bottom currents again show the strong tidal variation moving up and down river. The simulations capture the reduced bottom currents compared to the higher surface currents.

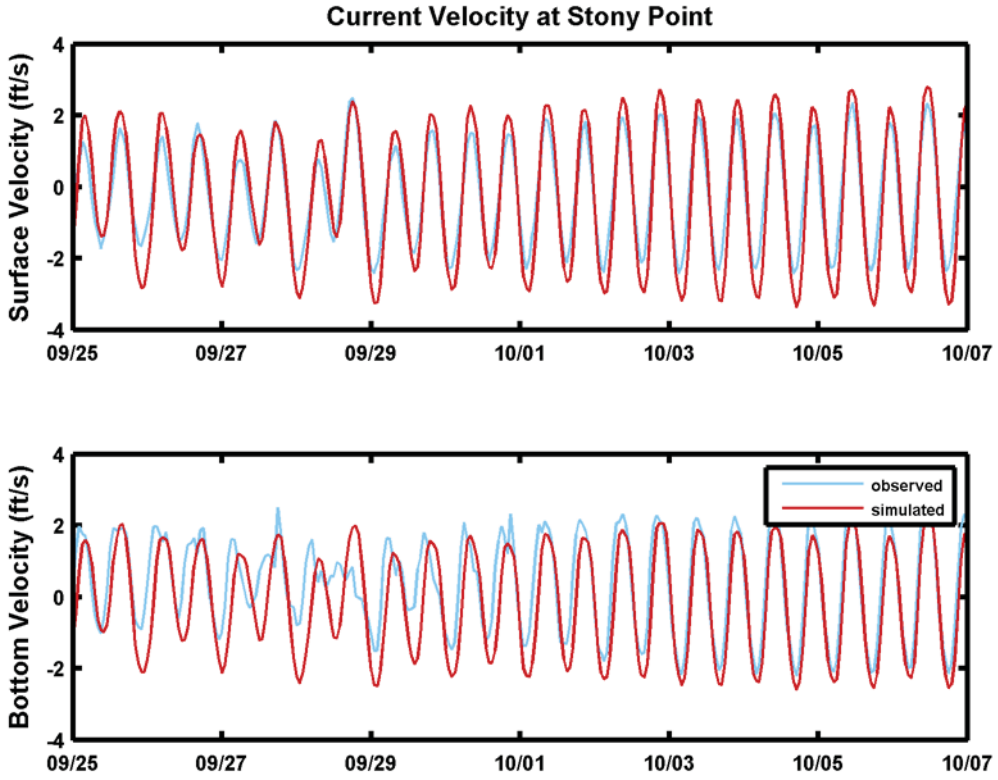

Figure 6-11 Surface (top) and bottom (bottom) current comparison between model predictions and observations for the calibration period from 24 September to 8 October 2009 at Stony Point.

Similar to the IP ADCP observations, the SP currents (Figure 6-11) show the strong tidal variation moving up and down river in both surface and bottom layers. Again, bi-weekly spring-neap cycle as well as diurnal inequality were successfully simulated on this station. The simulated flow is slightly larger than the observations in magnitude. The simulations capture the reduced bottom currents compared to the higher surface currents in a similar manner to the results at IP.

The quantitative calibration measures for the currents from the two ADCPs are presented in Table 6-4. In accordance with the time-series data presented above, the average statistics in this summary table shows that the current patterns was successfully simulated by the model being that the model meets the guidance values for RME and Skill although slightly over for ECV and under for r^2. The results show that the model predictions were better for the surface currents compared to those in the bottom layer.

Table 6-4 Quantitative comparisons of predicted and observed surface and bottom currents at Indian Point and Stony Point ADCPs for the calibration period from 24 September to 8 October 2009 at Stony Point.

Current Component Statistics	ECV	RME	r^2	Skill
Indian Point Surface Current	11	4	0.90	0.96
Indian Point Bottom Current	15	-9	0.79	0.91
Stony Point Surface Current	12	-2	0.92	0.96
Stony Point Bottom Current	19	-10	0.72	0.89
Average	14	6	0.83	0.93
Guidance	**10%**	**±30**	**0.94**	**0.92**

6.3.3. Temperature Comparisons

Temperature comparisons between model predictions and observations are shown as time series for selected surface and bottom thermistors, as well as USGS station data and IPEC intake temperature data. Each data type is separately presented below.

6.3.3.1 Thermistor Temperature Comparison

Temperature comparisons between model predictions and observations are shown for pairs of surface thermistor station locations (east and west side of the river) from the southernmost stations to the northernmost. Figure 6-1 shows all the thermistor station locations in the river. Figure 6-12 shows the comparison for stations 1 and 2, Figure 6-13 shows stations 5 and 6, Figure 6-14 shows stations 9 and 10, Figure 6-15 shows stations 14 and 15, Figure 6-16 shows stations 27 and 29, Figure 6-17 shows stations 37 and 38, Figure 6-18 shows stations 45 and 46, and Figure 6-19 shows stations 49 and 50. Comparisons should be made between surface simulations and observations separately from comparisons between bottom simulations and observations.

Stations 1 and 2 are the two southernmost thermistor mooring locations with station 1 on the west side of the main channel and station 2 on the east. Water depth for station 1 33 ft and depth for station 2 is 28 ft. Both the surface and bottom temperatures at stations 1 and 2 show similar characteristics indicating a relatively shallow, well-mixed system. The simulations at stations 1 and are slightly cooler, compared to the observations at the end of the period although the trend in temperature variation is similar.

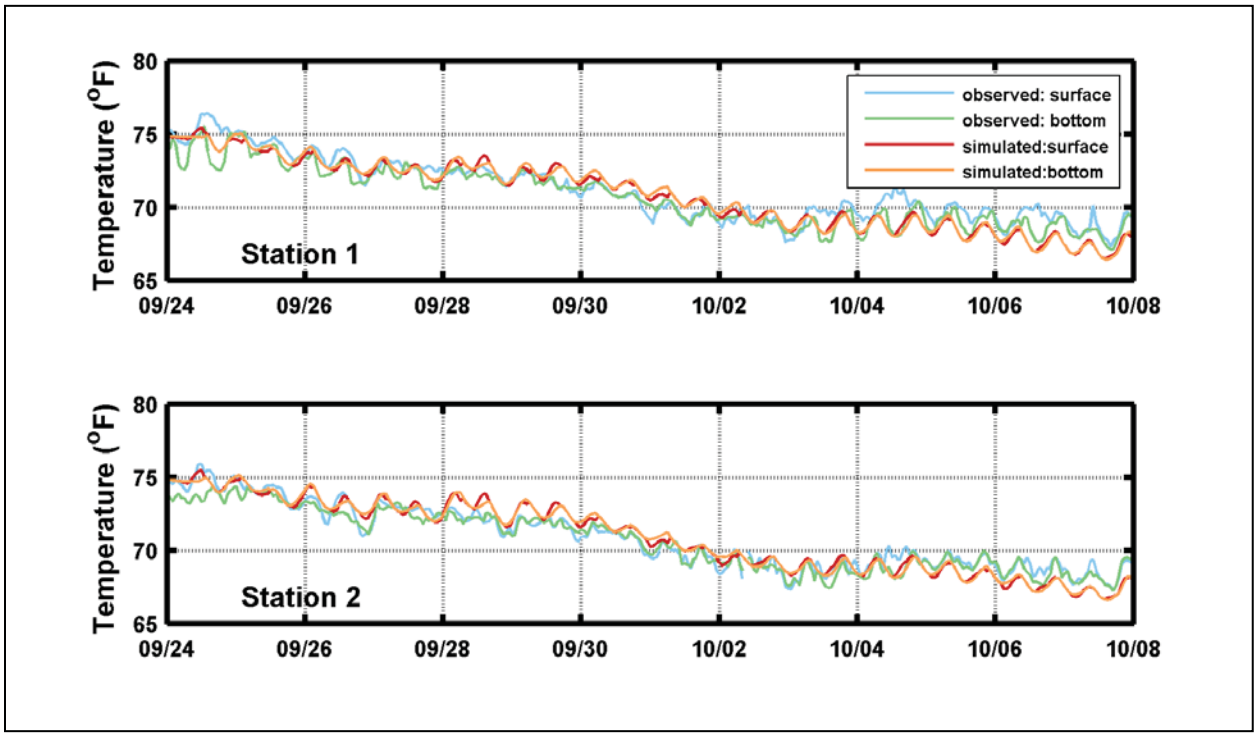

Figure 6-12 Surface and bottom temperature comparisons between model predictions and observations for the calibration period from 24 September to 8 October 2009 at stations 1 and 2.

Stations 5 and 6 are located approximately 2 mi up-River from stations 1 and 2, with station 5 on the west side of the main channel, and station 6 on the east. Water depth for stations 5 and 6 is 40 ft. Both the surface and bottom temperatures at stations 5 and 6 show similar characteristics indicating a relatively shallow, well-mixed system. The simulations at station 5 are slightly cooler compared to the observations at the end of the period, while at station 6 the simulations are slightly warmer at the beginning of the period although the trend in temperature variation is similar.

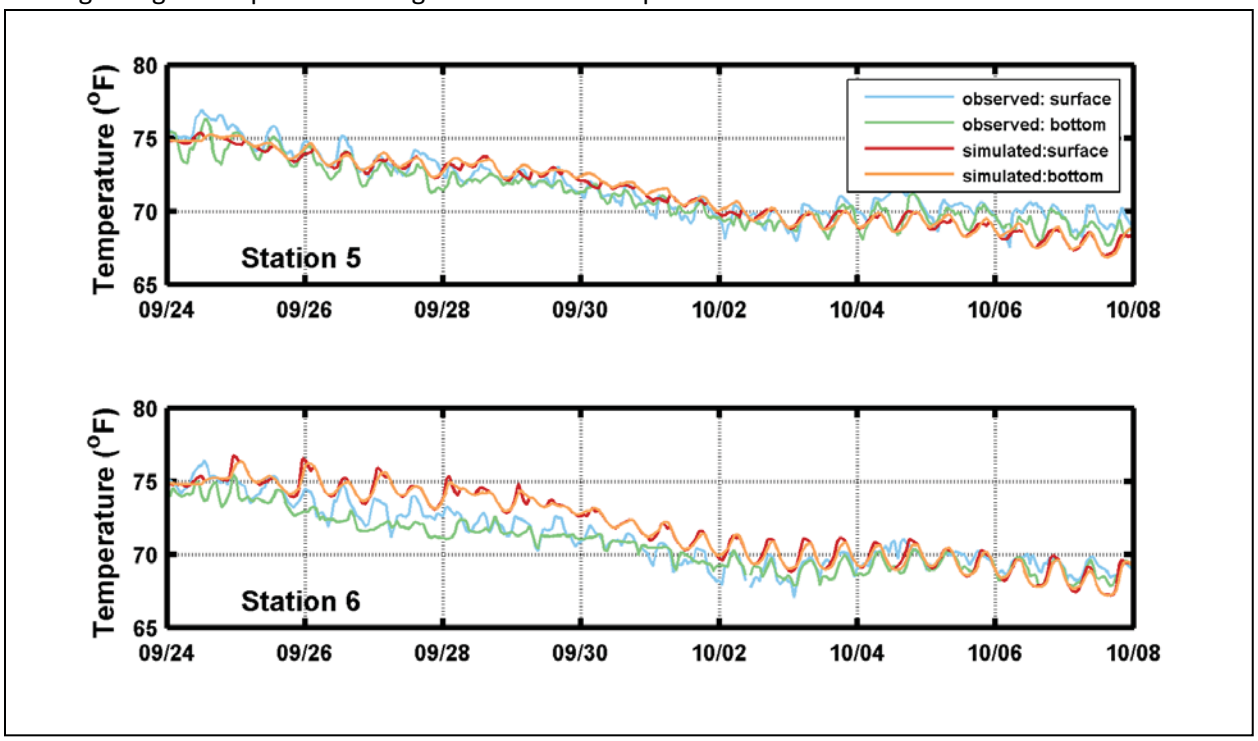

Figure 6-13 Surface and bottom temperature comparisons between model predictions and observations for the calibration period from 24 September to 8 October 2009 at stations 5 and 6.

Stations 9 and 10 are located approximately 2 mi up river from stations 5 and 6, in the vicinity of Stony Point, with station 9 on the west side of the main channel and station 10 on the east. Water depth for station 9 is 32 ft and depth for station 10 is 34 ft. The surface and bottom temperatures at station 9 show similar characteristics indicating a relatively shallow, well-mixed system. The simulations at station 9 are close to the observations. The surface and bottom temperatures at station 10 are somewhat different, however, indicating a rising or falling temperature response in phase with the tide at both the surface and less so at the bottom and is generally somewhat cooler at the bottom. This is most noticeable during the beginning of the calibration period 27 September and 2 October. The simulation captures this response although there is a smaller temperature difference between surface and bottom. The station 10 simulations are somewhat higher than the observations during the beginning of the period although the trend in temperature variation is similar.

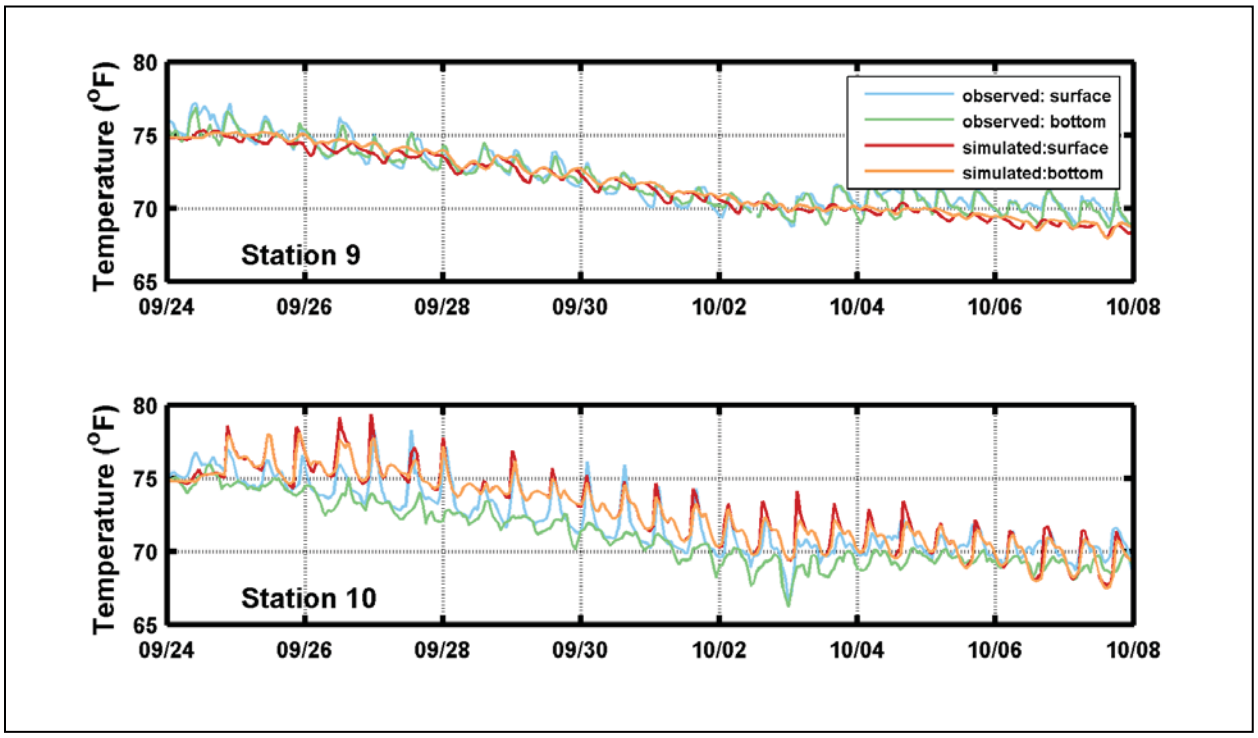

Figure 6-14 Surface and bottom temperature comparisons between model predictions and observations for the calibration period from 24 September to 8 October 2009 at stations 9 and 10.

Stations 14 and 15 are located approximately 1 to 1.5 mi up river from stations 9 and 10, in the vicinity of Stony Point, with station 15 on the west side of the main channel and station 14 on the east. Water depth for station 14 and 15 is 45ft. The surface and bottom temperatures at station 15 show generally similar characteristics, but the surface sometimes has relatively short small amplitude temperature spikes. The simulations at station 15 are close to the observations except for the spikes. The surface and bottom temperatures at station 14 are significantly different, however, indicating a relatively short rising and falling temperature response in phase with the tide at the surface but much less so at the bottom. The simulation captures this response. The station

14 simulations are higher than the observations early in the period but match well later in the period. The trend in temperature variation is similar.

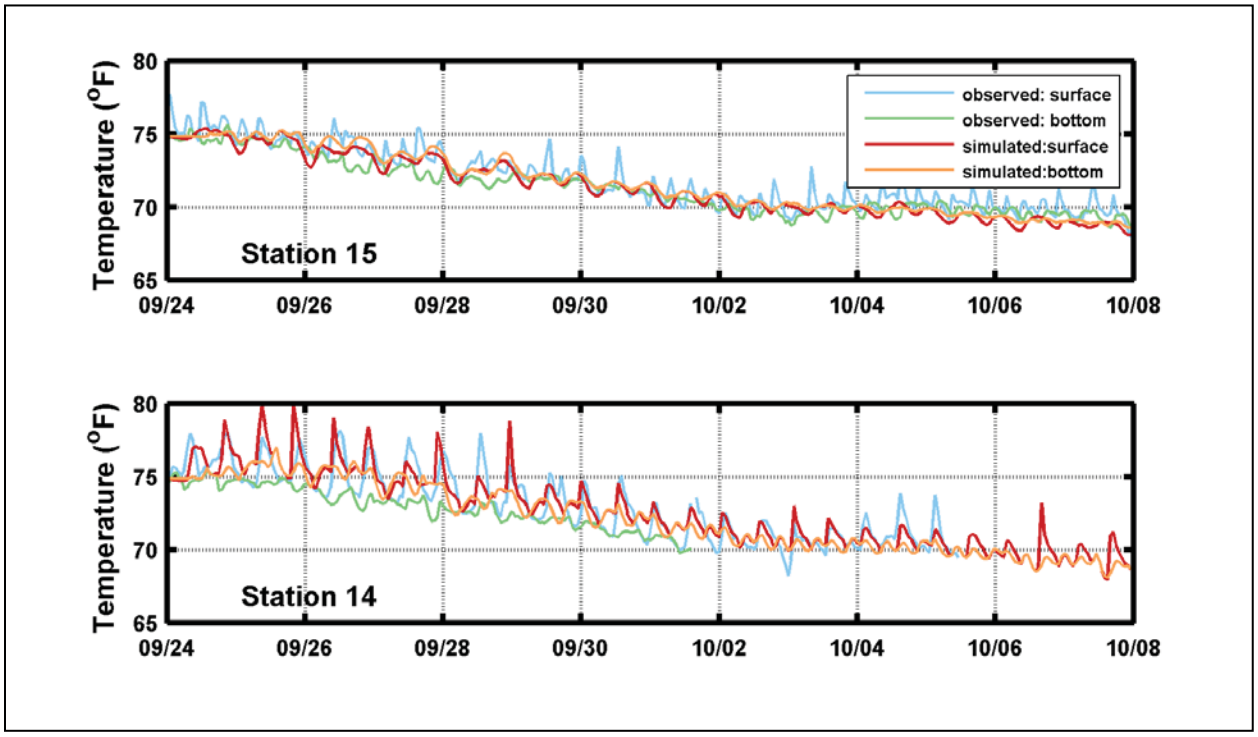

Figure 6-15 Surface and bottom temperature comparisons between model predictions and observations for the calibration period from 24 September to 8 October 2009 at stations 14 and 15.

Stations 27 and 29 are located on a line across the River from the IPEC, approximately 1 mi up River from stations 14 and 15, with station 29 on the west side of the main channel, and station 27 on the east. Water depth for station 29 is 16ft and depth for station 27 is 50 ft. The surface and bottom temperatures at station 29 show generally similar characteristics, but the surface sometimes has relatively short small amplitude temperature spikes which are typically smaller than those seen at station 15. The simulations at station 29 are close to the observations although slightly cooler towards the end of the period. The surface and bottom temperatures at station 27 are significantly different indicating a relatively short rising and falling temperature response in phase with the tide at the surface but not at the bottom. The simulation captures this response. The station 27 simulations capture the variations seen in the observations and the trend in temperature variation is similar.

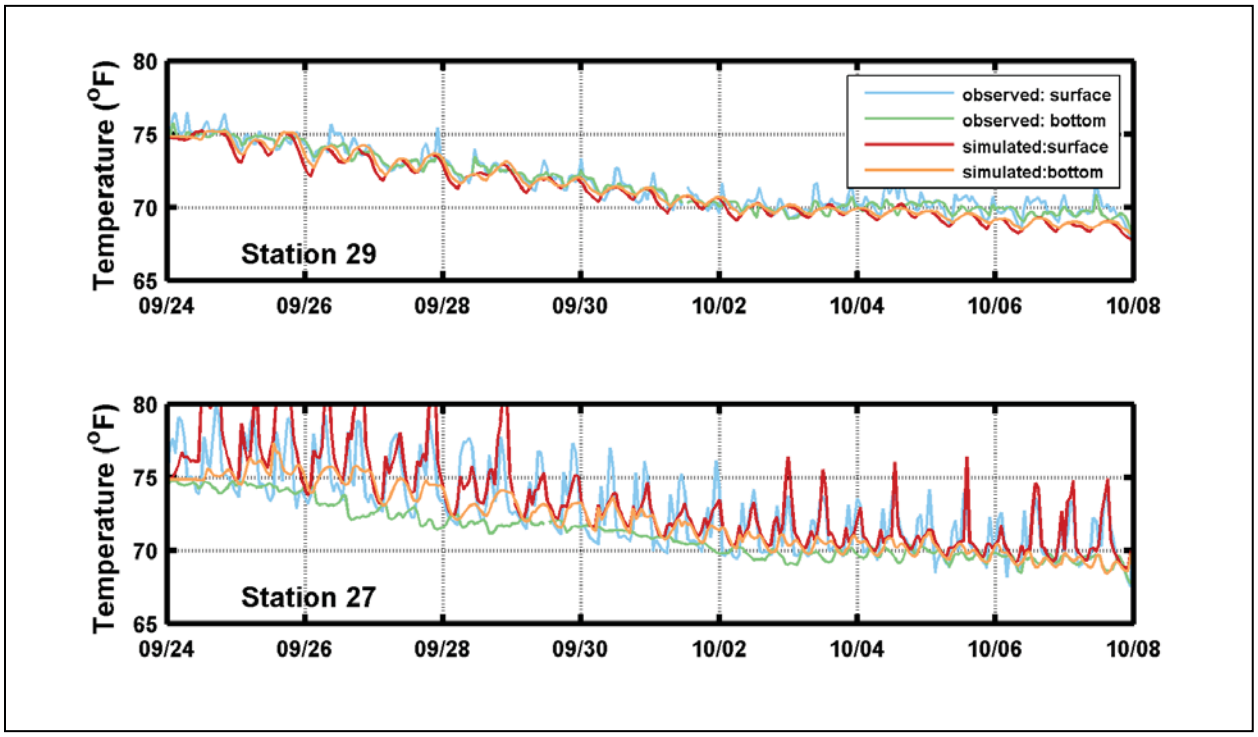

Figure 6-16 Surface and bottom temperature comparisons between model predictions and observations for the calibration period from 24 September to 8 October 2009 at stations 27 and 29.

Stations 37 and 38 are located approximately 0.5 mi up-River from stations 29 and 27, with station 37 on the west side of the main channel and station 38 on the east. Water depth for station 37 is 44 ft and depth for station 38 is 89 ft. The surface and bottom temperatures at station 37 show generally similar characteristics, but the surface sometimes has relatively short small amplitude temperature spikes. The simulations at station 37 are close to the observations. The surface and bottom temperatures at station 38 are significantly different indicating a rising and falling temperature response in phase with the tide at the surface and a similar but smaller response at the bottom. The station 38 simulations does not consistently capture the spikes seen in the observations, although the trend in temperature variation is similar.

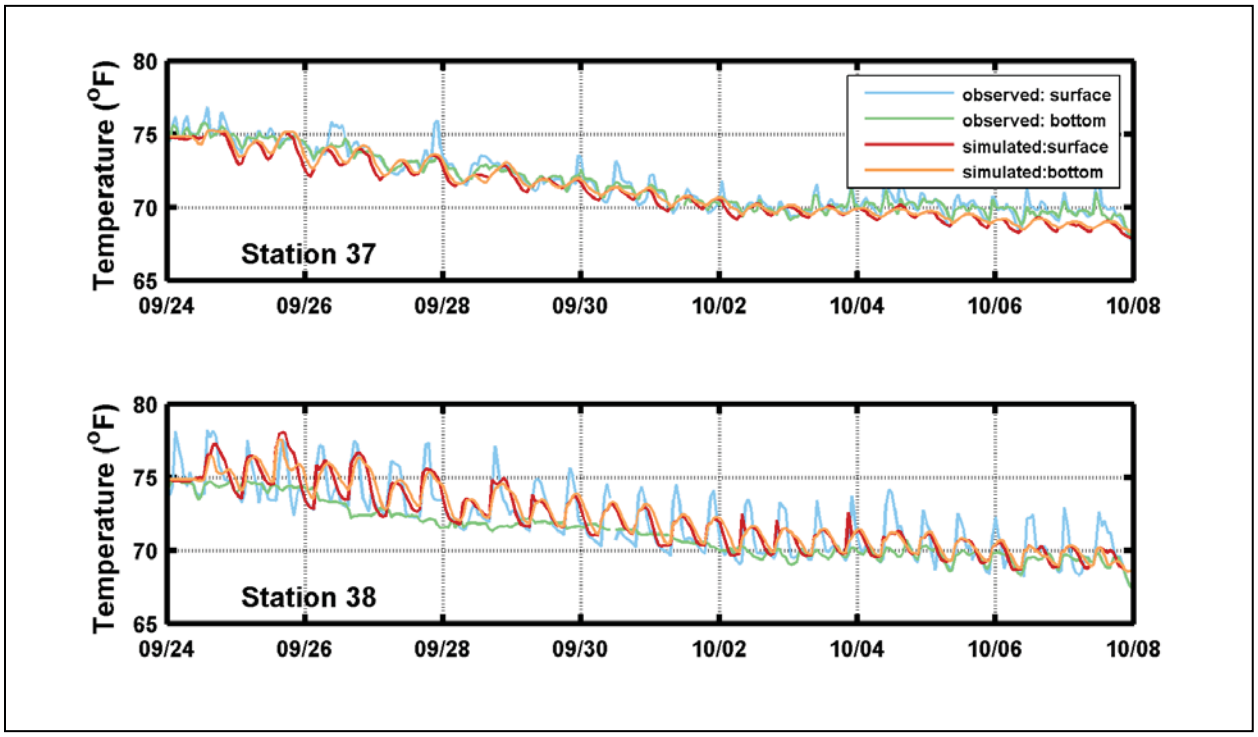

Figure 6-17 Surface and bottom temperature comparisons between model predictions and observations for the calibration period from 24 September to 8 October 2009 at stations 37 and 38.

Stations 45 and 46 are located approximately 1.5 to 2 mi up-River from stations 37 and 38, with station 46 on the west side of the main channel, and station 45 on the east. Water depth for station 45 is 59 ft and depth for station 46 is 70 ft. The surface and bottom temperatures at station 46 show generally similar characteristics. The simulations at station 46 are close to the observations. The surface and bottom temperatures at station 45 are also very similar and approximately the same temperature as station 46. The simulation typically captures this response. The trend in temperature variation for both simulations and observations is similar.

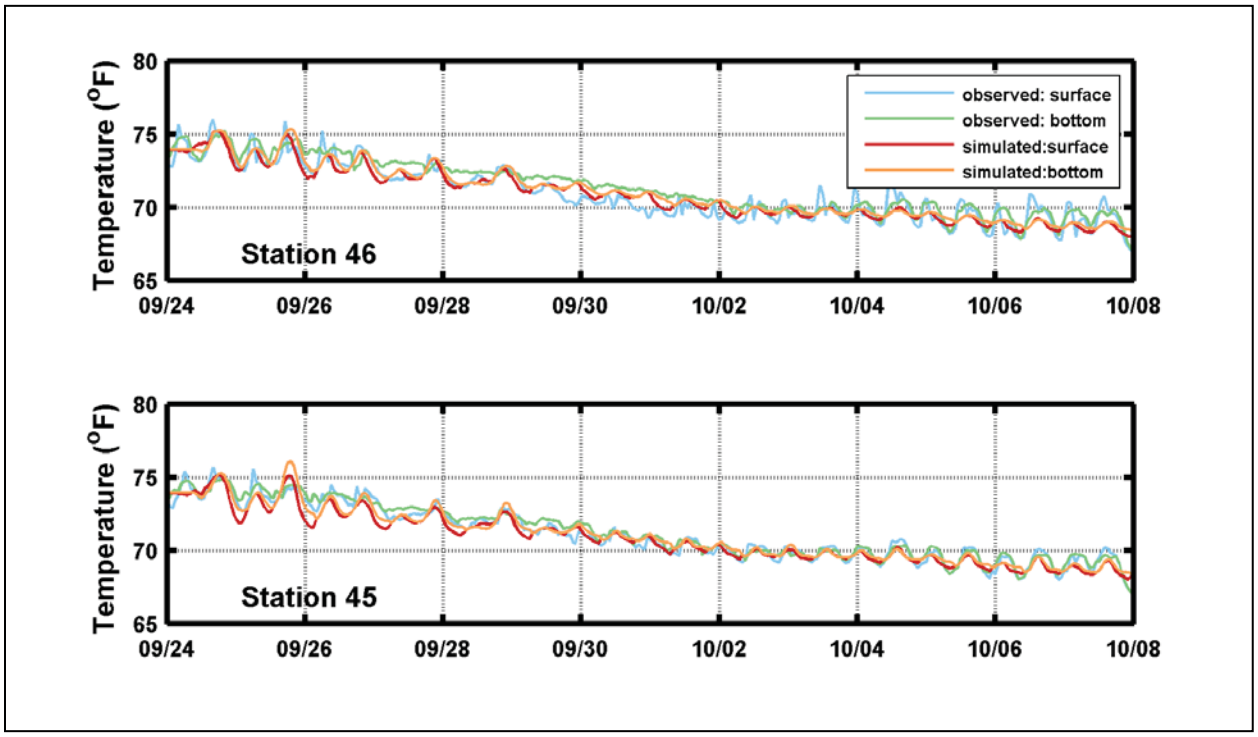

Figure 6-18 Surface and bottom temperature comparisons between model predictions and observations for the calibration period from 24 September to 8 October 2009 at stations 45 and 46.

Stations 49 and 50 are located approximately 2 mi up-River from stations 45 and 46, with station 50 on the west side of the main channel, and station 49 on the east. Water depth for station 49 is 41 ft and depth for station 50 is 28 ft. The surface and bottom temperatures at station 50 show generally very similar characteristics. The simulations at station 50 are close to the observations although with a smaller tidal amplitude. The surface and bottom temperatures at station 49 are also very similar and approximately the same temperature as station 50. The simulation typically captures this response again with smaller tidal amplitude.

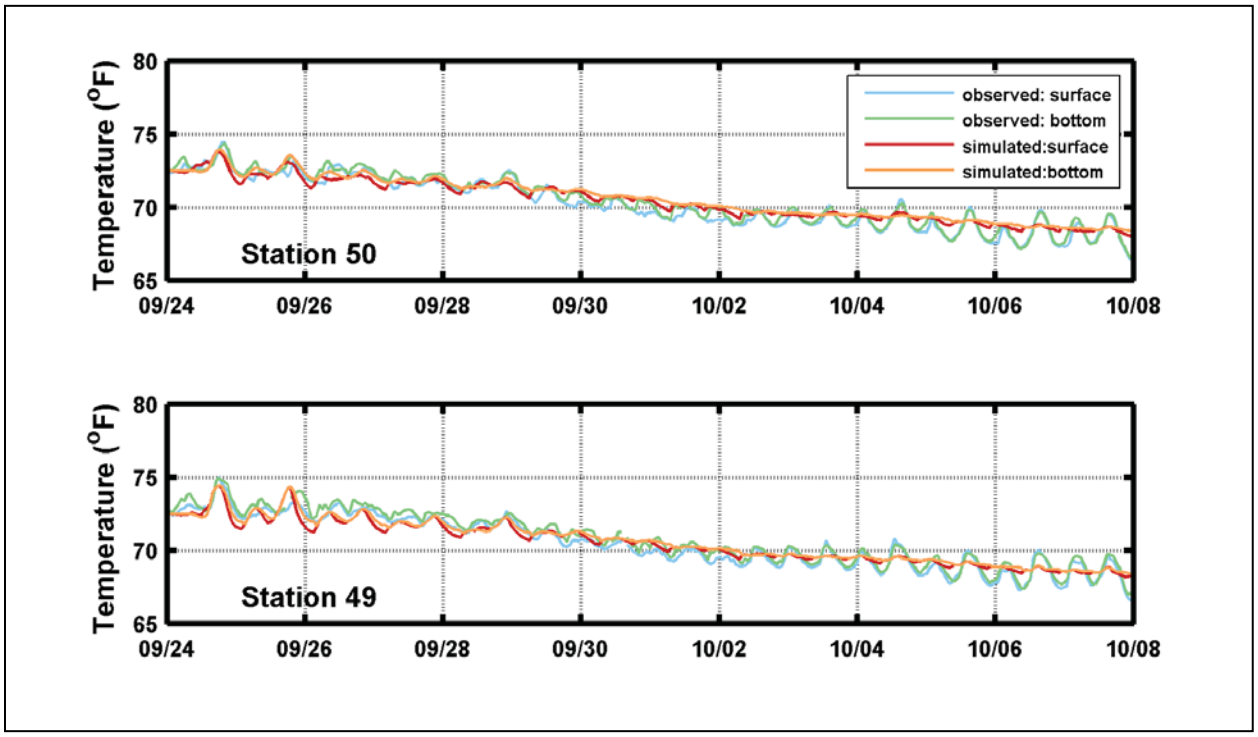

Figure 6-19 Surface and bottom temperature comparisons between model predictions and observations for the calibration period from 24 September to 8 October 2009 at stations 49 and 50.

6.3.3.2 Quantitative Statistical Measures

Quantitative comparisons for the selected thermistors are summarized in Table 6-5. Parameters presented in the tables are model and data statistical measures: relative mean error (RME), error coefficient of variance (ECV), and squared correlation coefficient, r^2. Also presented in each table are the average values of each measure and the USEPA guidance levels for each statistical measure. In addition model skill was calculated for each data set. The average of the skill was determined and compared with a previous modeling study of the Hudson River (Warner et al., 2005).

Table 6-5 Quantitative comparisons of predicted and observed temperatures for surface and bottom thermistors at selected stations for the calibration period.

Station	Location	r^2	RME	ECV	Skill
1	Surface	0.92	-1%	1%	0.95
1	Bottom	0.96	0%	1%	0.97
2	Surface	0.95	0%	1%	0.97
2	Bottom	0.97	0%	1%	0.97
5	Surface	0.91	-1%	1%	0.94
5	Bottom	0.94	0%	1%	0.96
6	Surface	0.91	1%	2%	0.92
6	Bottom	0.93	2%	2%	0.88
9	Surface	0.91	-1%	1%	0.94
9	Bottom	0.94	0%	1%	0.97
10	Surface	0.89	1%	2%	0.92
10	Bottom	0.91	2%	3%	0.85
15	Surface	0.93	-1%	1%	0.95
15	Bottom	0.95	0%	1%	0.96
14	Surface	0.90	0%	1%	0.94
14	Bottom	0.84	1%	2%	0.81
29	Surface	0.95	-1%	1%	0.95
29	Bottom	0.97	0%	1%	0.98
27	Surface	0.84	1%	3%	0.9
27	Bottom	0.92	1%	2%	0.9
37	Surface	0.94	-1%	1%	0.95
37	Bottom	0.97	0%	1%	0.98
38	Surface	0.87	0%	2%	0.93
38	Bottom	0.91	1%	2%	0.88
46	Surface	0.93	0%	1%	0.96
46	Bottom	0.97	0%	1%	0.97
45	Surface	0.96	0%	1%	0.97
45	Bottom	0.97	0%	1%	0.98
50	Surface	0.96	0%	1%	0.96
50	Bottom	0.96	0%	1%	0.97
49	Surface	0.95	0%	1%	0.96
49	Bottom	0.96	0%	1%	0.97
	Average	0.93	0.0%	1%	0.94
	Guidance	**0.84**	**±25%**	**45%**	**0.85**

Squared correlation coefficients for the surface temperature prediction vary from 0.84 (Station 27 Surface) to 0.97 for a number of stations, with an average for all thermistors of 0.93, higher than the USEPA guidance level of 0.84, clearly indicating modeling success. RME varies for the surface temperature predictions ranges between 0% and 2% with an average of 0%, compared to the guidance level of +25%. ECV varies from 1% (at many stations) to 3% (Station 10 Bottom and Station 27 Surface), with an average of 1%, compared to the USEPA guidance level of 45%. The RME and ECV values are much smaller than the guidance levels, implying that the model predicts the surface temperature well.

On average, the skill level of 0.94 exceeds the previous modeling result of 0.85, indicating equivalent success in modeling the temperature distribution.

The maximum longitudinal extent of the thermal plume is predicted to occur during slack tides, after peak currents have receeded resulting in a full extent of transported discharge from the previous tide and the pooling discharge due to the weak currents associated with slack condiitions. Figure 6-20 and Figure 6-21 below show the model predicted water surface temperatures for a representative slack before flood tide and slack before ebb tide respectively from the calibration time period. These Figures show that the bulk of the transport of heated discharage is along the eastern side fo the River, decreasing in temperature with distance across the channel as well as along the channel.

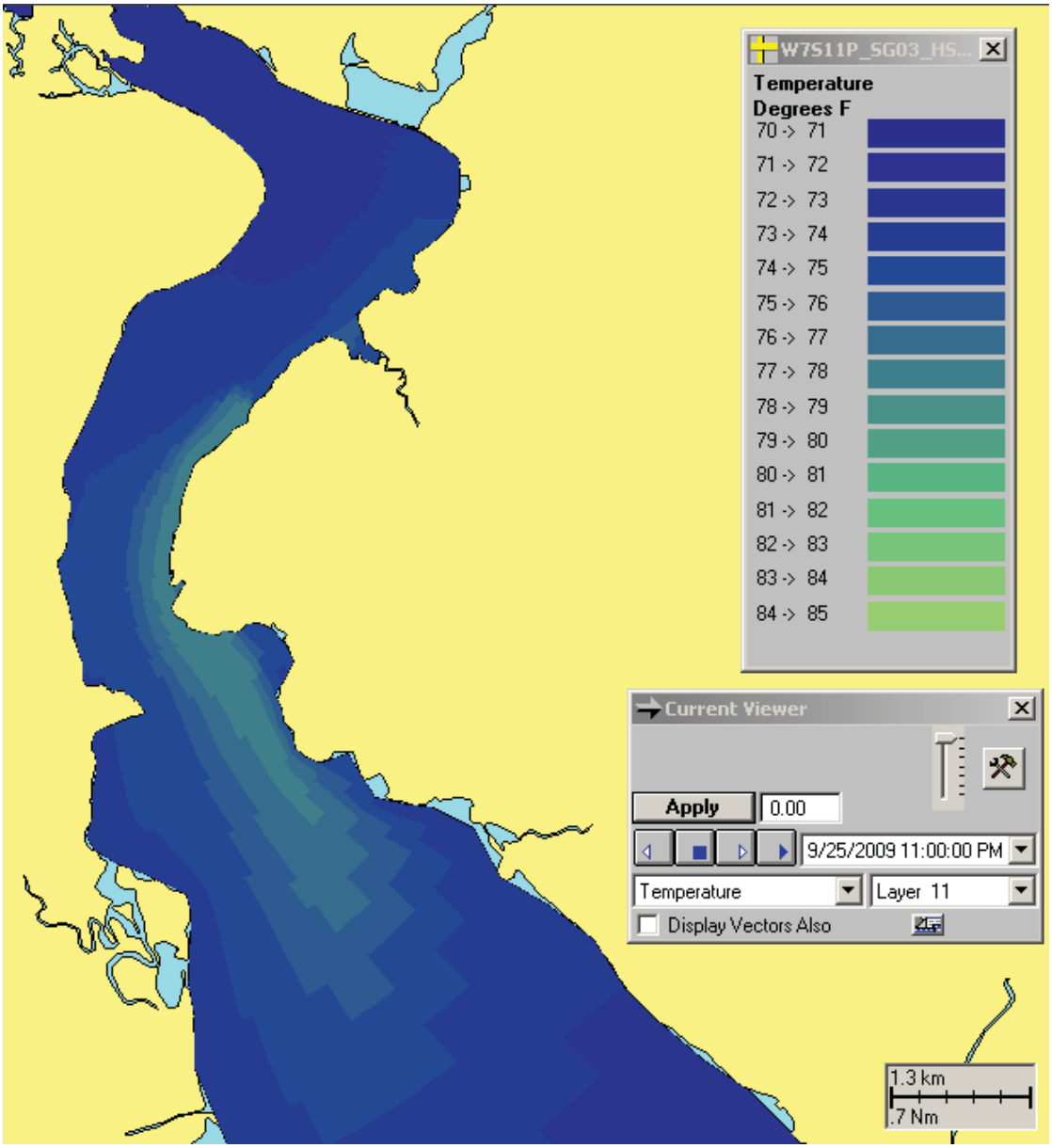

Figure 6-20 Plan view of the model predicted surface water temperatures showing the downstream extent of the plume at slack before flood during the Calibration time period.

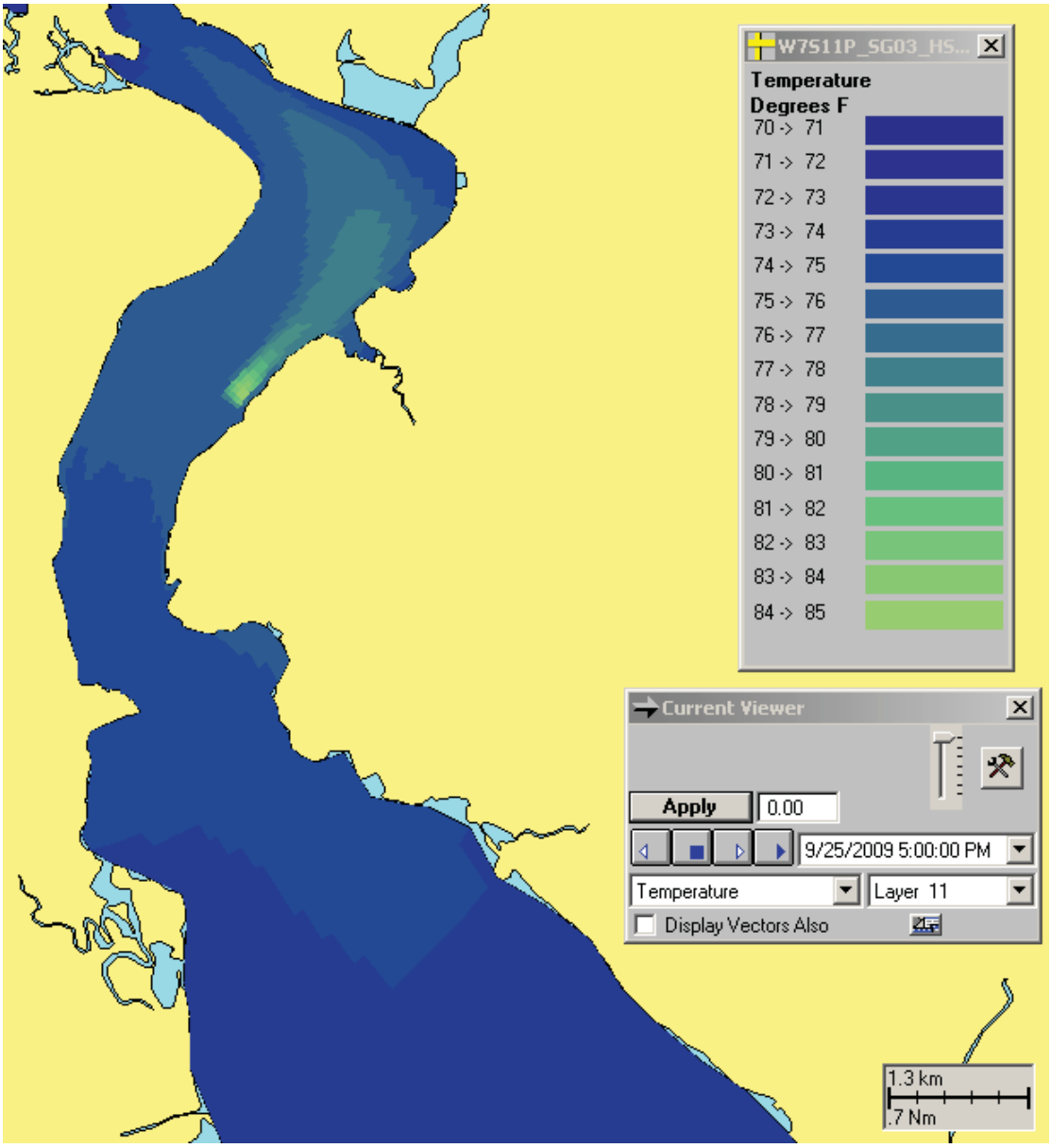

Figure 6-21 Plan view of the model predicted surface water temperatures showing the upstream extent of the plume at slack before ebb during the Calibration time period.

7. Scenario Simulation

There were two parts to the scenario simulation portion of this study: development of the scenario simulation time frame(s), and then model simulations and post processing. The model simulations utilized the previously calibrated model with appropriate forcing to reflect the scenario time frame(s). Furthermore, each scenario time period was run for two cases: one with the IPEC operating at maximum capacity (5163.4 MW of rejected heat at 1762.2 KGPM cooling water flow) and the other without the IPEC in operation, note that the 5163.4 estimate of rejected heat is conservative. The model results were then further processed to obtain the temperature differential between the two cases for each cell in the model domain at every time step of the model simulation period. This "deltaT" defines the relative IPEC thermal impacts to the River.

7.1. Development of Scenario Timeframe(s)

The goal of developing each scenario timeframe was to capture environmental conditions in which IPEC's thermal discharge exhibits the greatest spatial extent in the River. The thermal water quality standard (WQS) delineates both a surface distance limitation of 67% across the River, as well as a vertical cross sectional area requirement of 50% that is required to not exceed the allowable temperature differentials. A 4°F differential is applicable when the River ambient temperature is less than 83°F, and a more stringent differential of 1.5°F is applicable when the River ambient temperatures are above 83°F during the months of July through September.

Both a correlation analysis and a joint probability analysis were performed as search methods to identify and rank the environmental conditions most likely to result in the greatest extent of IPEC's thermal plume. First, a correlation analysis and stepwise regression to rank the most influential environmental forcing factors related to the hourly water temperature measured and recorded at West Point USGS gauging station. Second, a joint probability analysis to determine the magnitude, date, and hour of occurrence of the top three influential environmental factors corresponding to the50th, 90th, 95th and 99th probability of exceedance within the upstream and downstream period of record examined.

Both correlation and stepwise regression were performed on two classes of environmental variables; dependent and independent variables. The dependent variable used was the measured hourly water temperature at the West Point USGS gauge for the ten most recent years of available data (01 Jan 2000 through 31 Dec 2009; hours that contained missing data were excluded, resulting in a total of 83,028 hours of observation). The hourly independent variables used in this correlation analysis were: water temperature, tidal elevation, and salinity at Hastings, Lock 1 discharge, dew point, dry bulb temperature, relative humidity, and solar insolation at White Plains Airport. It was recognized that not all of the independent variables are completely independent of each other. For example, dry bulb temperature, dew point, and relative humidity are not independent. However, the purpose of this analysis was to search for the smallest suite of "independent" variables explaining the greatest amount of hourly variation in measured water

The analysis showed that West Point water temperature, White Plains air temperature and Lock 1 upstream River discharge were the factors that had the strongest correlation to surface thermistor temperatures near the IPEC. A correlation coefficient of 1 indicates that two variables are perfectly positively correlated, a value of -1 indicates that two variables are perfectly negatively correlated, and a value of 0 signifies no correlation. The correlation coefficients for water temperature ranged from 0.83 to 0.99, the most highly correlated variable, as illustrated as correlation contours in Figure 7-1. This indicates that increases or decreases in thermistor temperatures are positively related to

West Point water temperature. The correlation coefficients for White Plains air temperature ranged from 0.48 to 0.59, second most highly correlated variable, as illustrated in Figure 7-2. This result indicates that increases or decreases in thermistor temperatures are positively related to White Plains air temperature, but less so than West Point water temperature. The correlation coefficients for River discharge ranged from -0.25 to -0.57, the third most highly correlated variable, as illustrated in Figure 7-3 This result indicates that increases or decreases in thermistor temperatures are negatively related to Lock 1 River discharge, again less so than the positive relation of the West Point water temperature.

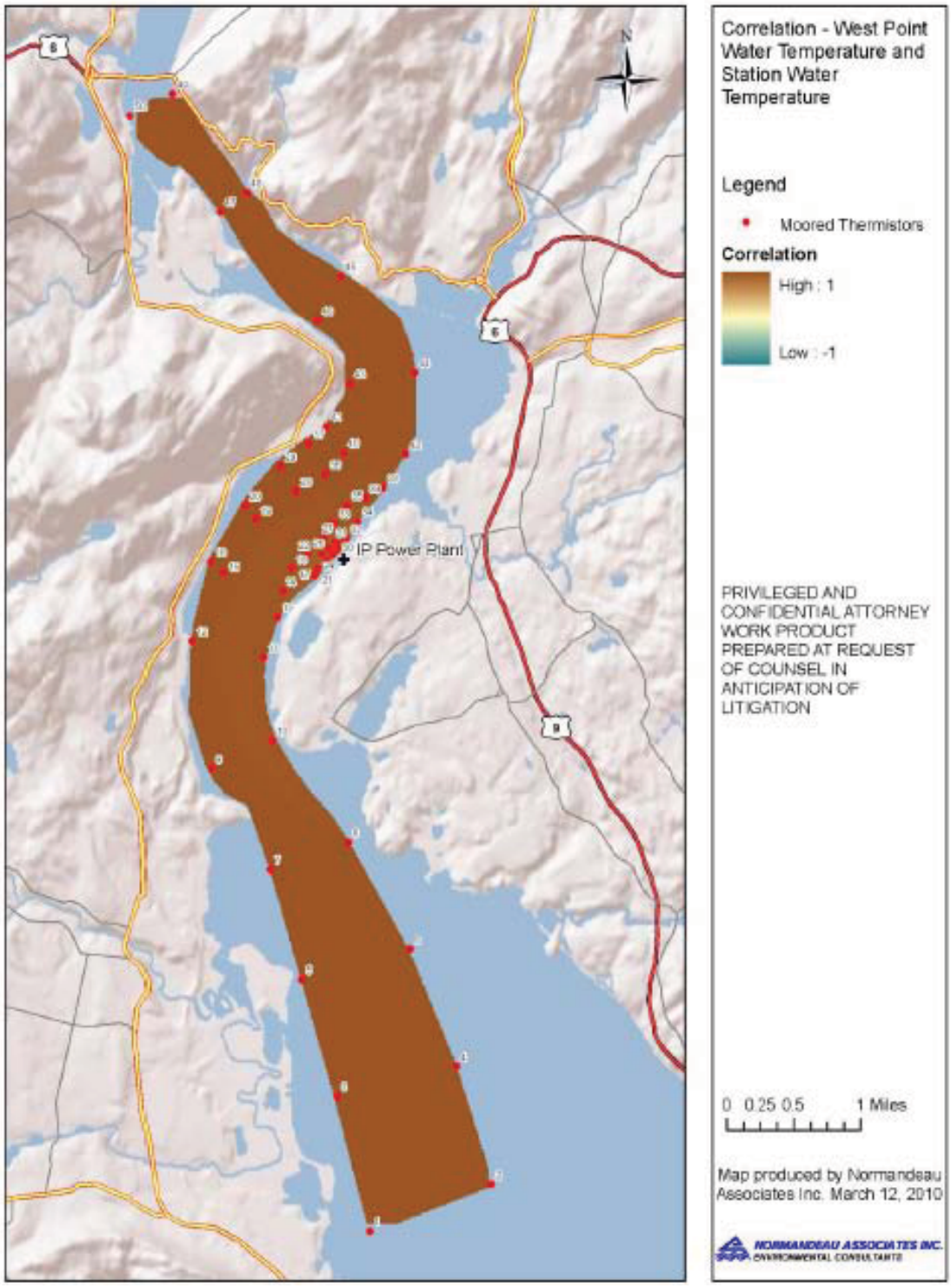

Figure 7-1 Contour plot of correlation values of thermistor water temperatures to water temperature at West Point.

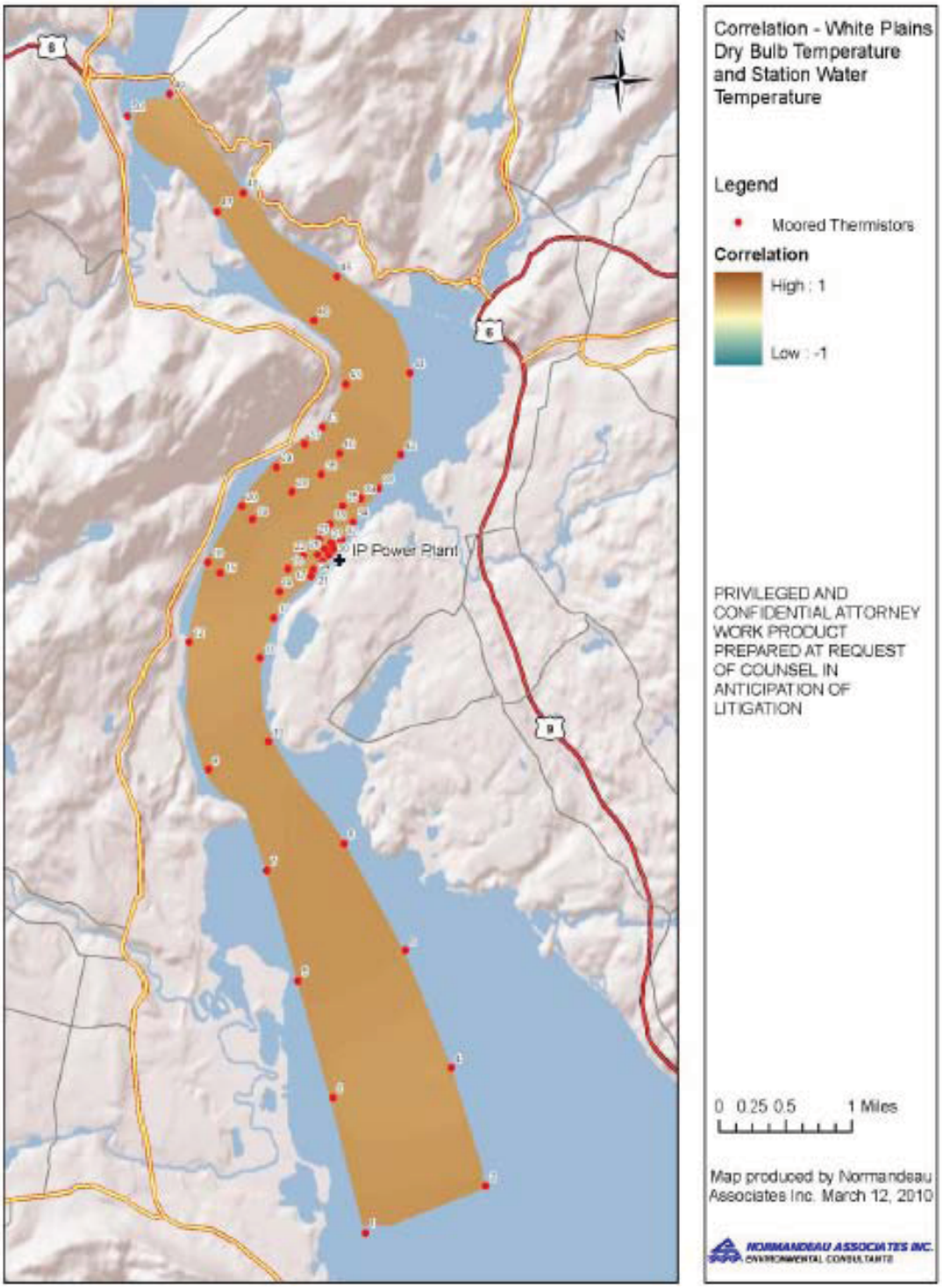

Figure 7-2 Contour plot of correlation values of thermistor water temperatures to air temperature at White Plains.

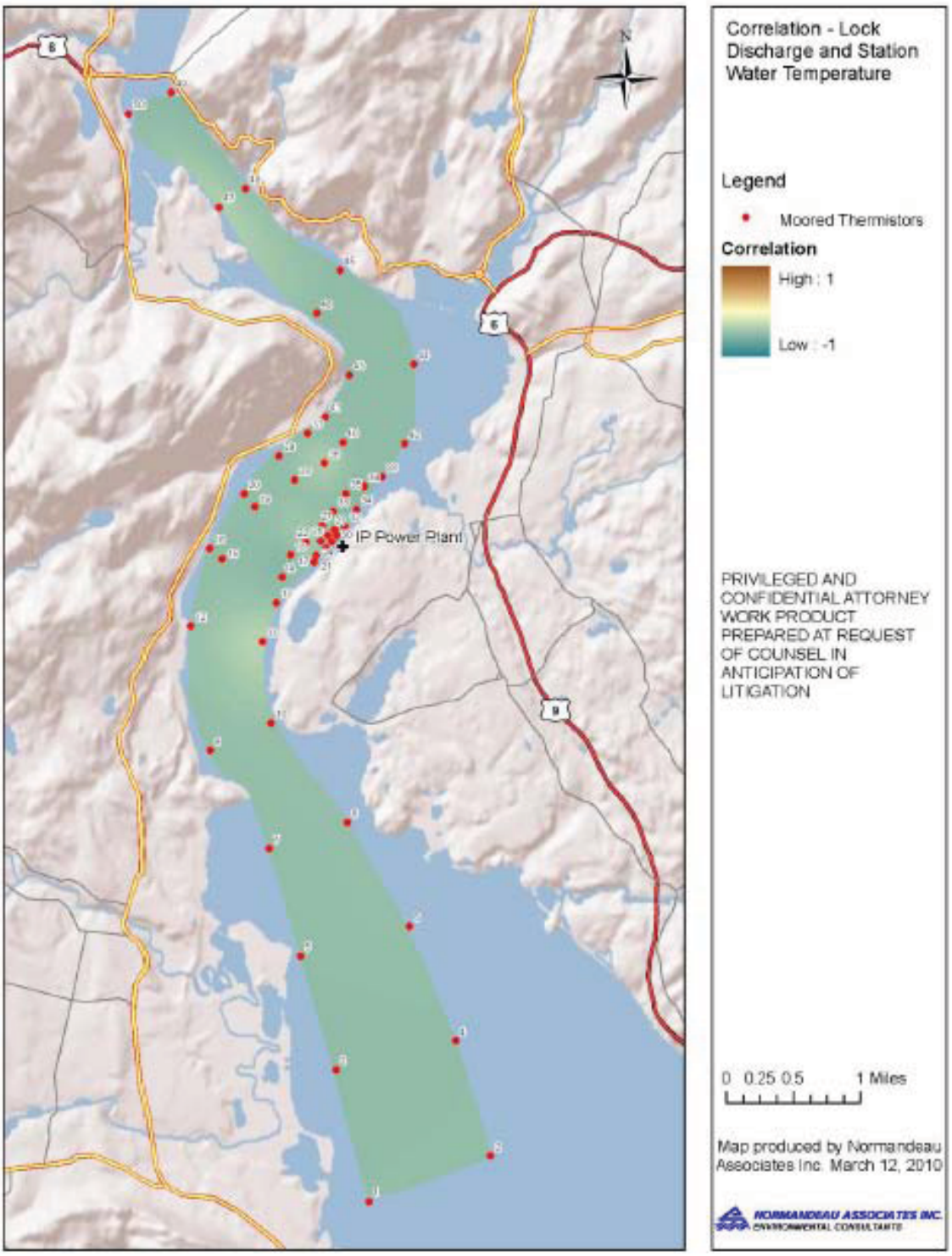

Figure 7-3 Contour plot of correlation values of thermistor water temperatures to River discharge at Lock 1.

Once the three most influential environmental factors correlating to temperature near the IPEC were identified, their joint probability of exceedance was estimated to identify their 50th, 90th, 95th and 99th exceedance probabilities, and the corresponding times of these joint occurrences in the ten

year period of record from the West Point USGS station. The three factors were the Lock 1 discharge, West Point water temperature and White Plains air temperature data for the most recent decade (2000 through 2009) of available USGS data, consisting of 83,028 hourly records. The three-way probability of exceedance values were calculated under the assumption that each of these factors were independent, meaning that their joint probabilities were considered multiplicative and estimated by their product. For example, at a probability of exceedance of 90% each for low Lock 1 discharge (probability of exceedance = 1.0 – 0.9 = 0.1), warm West Point water temperature (probability of exceedance = 1.0 – 0.9 = 0.1), and warm White Plains air temperature (probability of exceedance = 1.0 – 0.9 = 0.1), the joint probability of each of these three conditions occurring simultaneously within the same hour if all were independent can be estimated as a probability of exceedance of $(1\text{-}.90)^3$ or 1 hour out of every 1,000 hours. If these three factors were indeed independent, then we would expect, on average, 83 hours of occurrence of the joint probability of exceedance within the 83,028 hours found in the recent decade of record. The actual frequency (number of hours) of occurrence in the decade of record is a test of the assumption that these factors were truly independent, and an empirical estimate of their joint probability of exceedance in the decade of record. The dates and times of the joint probability of exceedance hours found in the decade of record identifies the actual conditions to model to represent the three way joint probability of exceedance of low Lock 1 discharge, high West Point water temperature, and high White Plains air temperature with the extreme rare occurrence of 1 hour out of every 1000 hours for the River near IPEC. The results presented in terms of hours per month for each percentile rank are summarized in Table 6-1. Note that the 50th percentile conditions occur only in months April through November, 90th percentile conditions occur only in months July through September, 95th percentile conditions occur only in July and August and that there is no record of joint probability of 99th percentile conditions naturally occurring (1 hour out of every 1,000,000 hours, if independent).

Table 7-1 Number of hours of exceedance of joint probability of air temperature, river flow, and river temperature during all April, May and June months of the decade 2000-2009 based on all 12 months of data.

		Probability			
		P=50	P=90	P=95	P=99
White Plains Air Temperature (°F)		52	74	79	86
West Point Water Temperature (°F)		54.34	77.42	79.41	81.71
Lock 1 (Troy) Discharge (cfs)		6419.8	2970.8	2409.46	1645.5
Total # Hours		83028	83028	83028	83028
April	2002	7			
	2006	16			
	2008	1			
May	2000	60			
	2001	401			
	2002	156			
	2003	229			
	2004	444			
	2005	292			
	2006	225			
	2007	311			
	2008	367			

		Probability			
		P=50	P=90	P=95	P=99
White Plains Air Temperature (°F)		52	74	79	86
West Point Water Temperature (°F)		54.34	77.42	79.41	81.71
Lock 1 (Troy) Discharge (cfs)		6419.8	2970.8	2409.46	1645.5
	2009	283			
June	2000	185			
	2001	137			
	2002	74			
	2003	465			
	2004	231			
	2005	434			
	2006	447			
	2007	650			
	2008	691			
	2009	371			
July	2000	428			
	2001	540	56		
	2002	635	116	14	
	2003	728			
	2004	519	3		
	2005	505	38	6	
	2006	445	15		
	2007	730	57	2	
	2008	597	52	7	
	2009	377			
August	2000	354			
	2001	744	210	44	
	2002	744	185	56	
	2003	24			
	2004	405			
	2005	743	130	29	
	2006	669	38	14	
	2007	743	171	24	
	2008	373	9		
	2009	422			
September	2000	576			
	2001	636	24		
	2002	698			
	2003	586			
	2004	397			
	2005	337	30		

		Probability			
		P=50	P=90	P=95	P=99
White Plains Air Temperature (°F)		52	74	79	86
West Point Water Temperature (°F)		54.34	77.42	79.41	81.71
Lock 1 (Troy) Discharge (cfs)		6419.8	2970.8	2409.46	1645.5
	2006	634			
	2007	678	46		
	2008	659			
	2009	515			
October	2000	300			
	2001	413			
	2002	333			
	2003	147			
	2004	317			
	2005	299			
	2006	131			
	2007	542			
	2008	349			
	2009	75			
November	2000	69			
	2001	116			
	2004	54			
	2007	57			
Total		26120	1180	196	0
Actual Joint Probability		0.3146	0.0142	0.002361	
Expected Joint Probability		0.125	0.001	0.000125	0.000001

As noted above, the joint probabilities presented here are multiplicative of the individual independent variable probabilities. The Expected Joint Probability shown at the bottom of Table 1 reveals that the 99th percentile joint probability occurs once in 1,000,000 hours.

The results in Table 6-1 imply that a single scenario timeframe should be chosen in July of 2002, 2005, 2007 or 2008 or August of 2001, 2002, 2005, 2006 or 2007. To determine which year best represents these extremes, the joint probability analysis was rerun based on the data from the period of record of summer months of July, August and September only. These results differ from the analysis using the entire 12-month (annual) period (83,028 hours), since these months will produce percentiles based only on the summer conditions (20,513 hrs) and therefore the value of the 50th percentile water temperature, for instance, will be higher (76.64°F) than the annual value (54.34°F). Table 7-2 summarizes the results of this analysis.

Table 7-2 Number of hours of exceedance of joint probability of air temperature, river flow, and river temperature during all July, August and September months of the decade 2000-2009 based on the three summer months of data.

		Probability			
		P=50	P=90	P=95	P=99
White Plains Air Temperature (°F)		70	80	83	89
West Point Water Temperature (°F)		76.64	80.66	81.5	82.83
Lock 1 (Troy) Discharge (cfs)		4171.7	2367.2	2015.6	1490.51
Total # Hours		20513	20513	20513	20513
July	2001	137			
	2002	332			
	2003	93			
	2004	55			
	2005	161	3	2	
	2006	104			
	2007	247			
	2008	238			
August	2001	460	16		
	2002	427	29		
	2003	1			
	2004	35			
	2005	453	19	6	
	2006	163			
	2007	373	5		
	2008	38			
	2009	35			
September	2001	104			
	2002	18			
	2005	58			
	2007	145			
	2008	75			
Total		3752	72	8	
Actual Joint Probability		0.1829	0.0035	0.0002	0
Expected Joint Probability		0.125	0.001	0.0001	0.000001

This summer joint probability analysis showed a frequency of occurrence in July 2005 (2 hrs) and August 2005 (6 hrs) at the P95 level and so 2005 is the preferred year. The procedure was again repeated using only input from all the August months over the decadal period of record for each variable. These results are summarized in Table 7-3.

Table 7-3 Number of hours of exceedance of joint probability of air temperature, river flow, and river temperature during all August months of the decade 2000-2009 based on the August months of data.

	Probability			
	P=50	P=90	P=95	P=99
Air Temperature >	72	82	85	91

Water Temperature >		79.19	81.995	82.59	83.255
Lock discharge <		4227.2	2235	1856	1301.533
Total # Hours		6673	6673	6673	6673
August	2001	322			
	2002	370			
	2005	359	12	1	
	2006	123			
	2007	223			
	2008	13			
Total		1410	12	1	
Actual Joint Probability		0.2113	0.0018	0.0001	0
Expected Joint Probability		0.125	0.001	0.0001	0.000001

The August joint probability analysis showed that August 2005 had the most extreme set of conditions with 12 hours reflective of 90th percentile of all August conditions and 1 hour reflective of 95th percentile of all August conditions. Based on this finding, the annual joint probability hourly detailed results were reviewed to see which hours in August 2005 had the highest water temperature and the scenario run period was chosen to encompass this time as well as those times that was reflective of the 50th and 90th percentiles as well. The actual period corresponds to a scenario timeframe of 1 through 15 August 2005.

7.2. Scenario Forcing

7.2.1. Lower River Boundary at Hastings during Scenario Timeframe

The downstream open boundary forcing used available USGS collected data at Hastings-on-Hudson. The site, designated as 01376304, measured water level, as well as temperature and conductivity at a depth of 10 ft. Data was provided at 15-min intervals and was processed to hourly averages and subsampled to the hour. The sensitivity of the model to water level forcing required that the original 15-min interval be used. Figure 7-4 shows the time history over the scenario period of water level, temperature and salinity. During this time period the average tidal amplitude is 2 ft with a neap tide occurring around 12 August, water temperatures vary between 80-85°F and the salinity varies between 7-17 psu; these values all measured at 10ft below the surface.

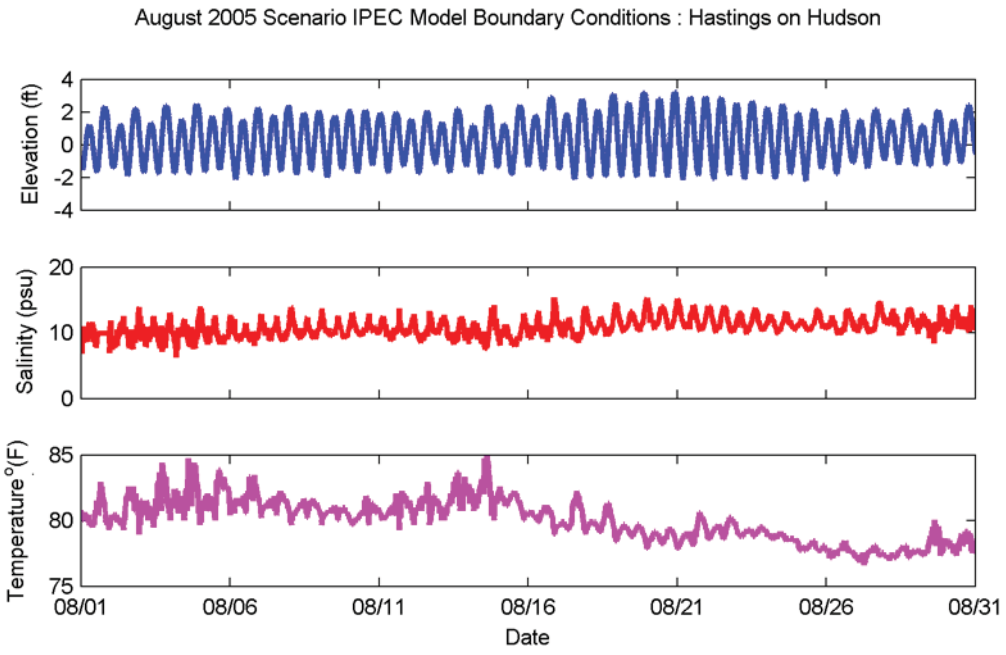

Figure 7-4 USGS water level, temperature and salinity for the scenario period from 1 August to 31 August 2009 measured at Hastings.

7.2.2. Upper River Boundary at Troy during Scenario Timeframe

The upstream open boundary forcing used available USGS collected data at two adjacent sites near the dam in Troy. The Lock 1 site, designated as 01335754, provided river flowrate data while Albany, designated as 01359139, provided water temperature (salinity was zero), both at 10-ft depths below the surface. Data was provided at 15-min intervals and was processed to hourly averages and subsampled to the hour. Figure 7-4 shows the time history over the scenario period of flowrate and temperature. River flow is relatively low, ranging between 1,000 and 6,500 cfs, and River temperatures are relatively high varying between 80-83°F during this timeframe.

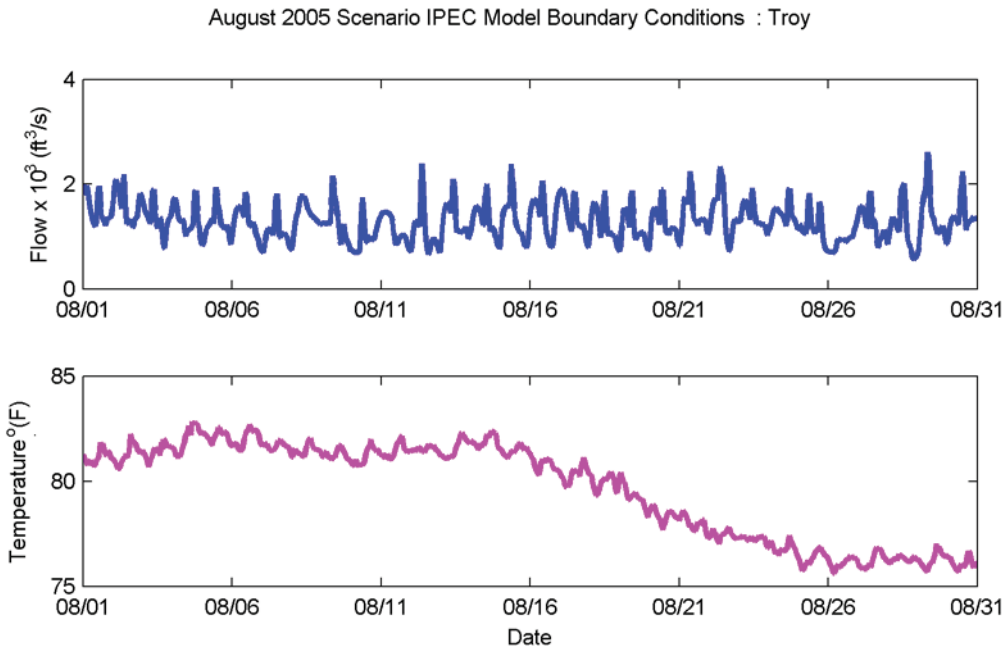

Figure 7-5 USGS flowrate and temperature for the calibration period from 1 August through 31 August 2005 measured at Lock 1 and Albany.

7.2.3. Meteorological Conditions at White Plains during Scenario Timeframe

The meteorological conditions used in the model were those from the White Plains Airport. The data consisted of air temperature, dew point, relative humidity, wind speed and direction, pressure and radiation. Figure 7-6 shows the time history of these variables during the scenario period.

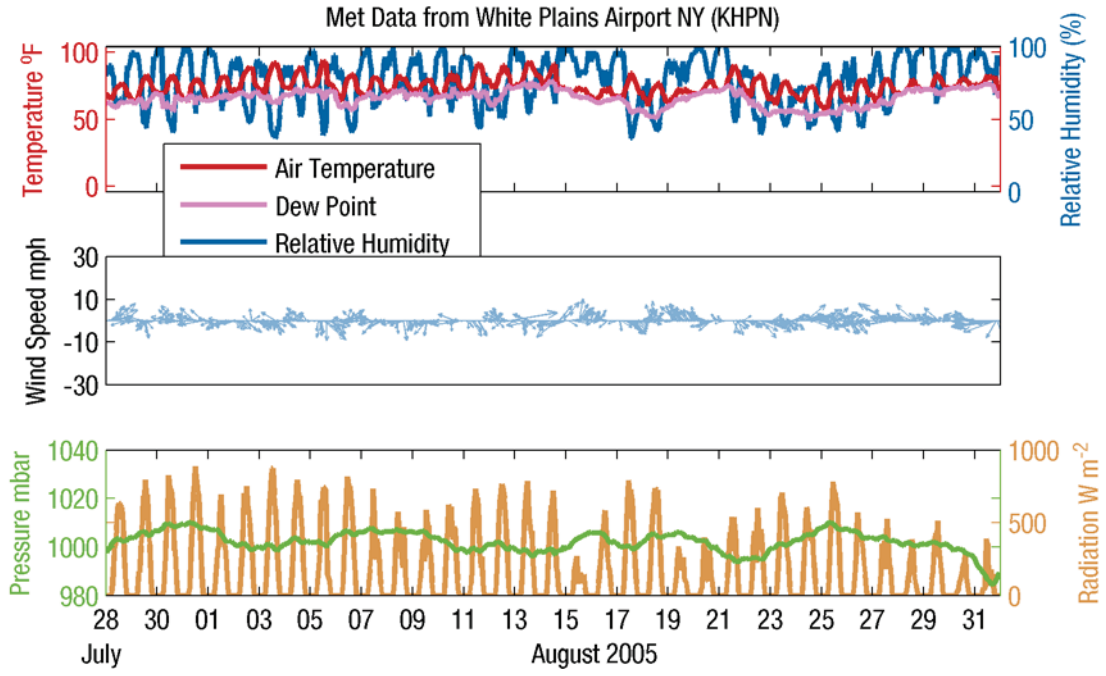

Figure 7-6 NRCC meteorological data for the scenario period from 1 August 2005 to 31 August 2005 measured at the White Plains Airport.

7.2.4. Plant Thermal Discharges during Scenario Timeframe

7.2.4.1 IPEC Operations

In order to determine the maximum potential thermal contribution, the plant representation in the model assumed that the plant was operating at maximum capacity; this equates to a constant flow rate of 1762.2 KGPM with a temperature differential between discharge and intake of 20°F representing a plant heat rejection to the cooling water of 5163.4 MW, note that this is a conservative estimate of heat rejection.

7.2.4.2 Other Plant Operations

Other plant operations data were unavailable during the scenario timeframe. However, such data were not considered necessary for the scenario simulations, since the evaluation was focused on the difference between model simulations with and without IPEC inputs in order to determine its thermal contribution. The contributions of other plants would be represented the same way during the scenario timeframe runs (with and without IPEC inputs) and therefore the difference between the two runs due to other plant contributions would be zero.

7.3. Scenario Results

Once the scenario timeframe was established, the calibrated model was then used to simulate this period for two cases: one with the plant operating at maximum capacity (5163.4 MW thermal with a flow rate of 1762.2 KGPM), and one simulating conditions with the plant not operating.

7.3.1. Comparison (Validation) of Model Predictions to Observations for Scenario Time Period

The model application to the August 2005 Scenario time frame was first compared to available observations during that period. This constitutes a qualitative model validation to a consistent but small independent data set. A comparison of the model predicted water surface elevations at West Point, Poughkeepsie and Albany is presented in Figure 7-7, where the observations are shown in blue and the model predictions are shown in red. The comparison indicates a similar response to the tidal forcing predicted in the calibration simulation, showing that the model has well represented the large variability in both tidal range and phase through the River system. A similar comparison for the model predicted surface water temperatures at the same USGS stations is presented in Figure 7-8. While the modeled and observed temperature signals at Poughkeepsie and Albany are relatively uneventful, the model clearly reproduces the combined diurnal and semi-diurnal temperature signals at West Point, nearest to the upstream end of the Indian Point study area.

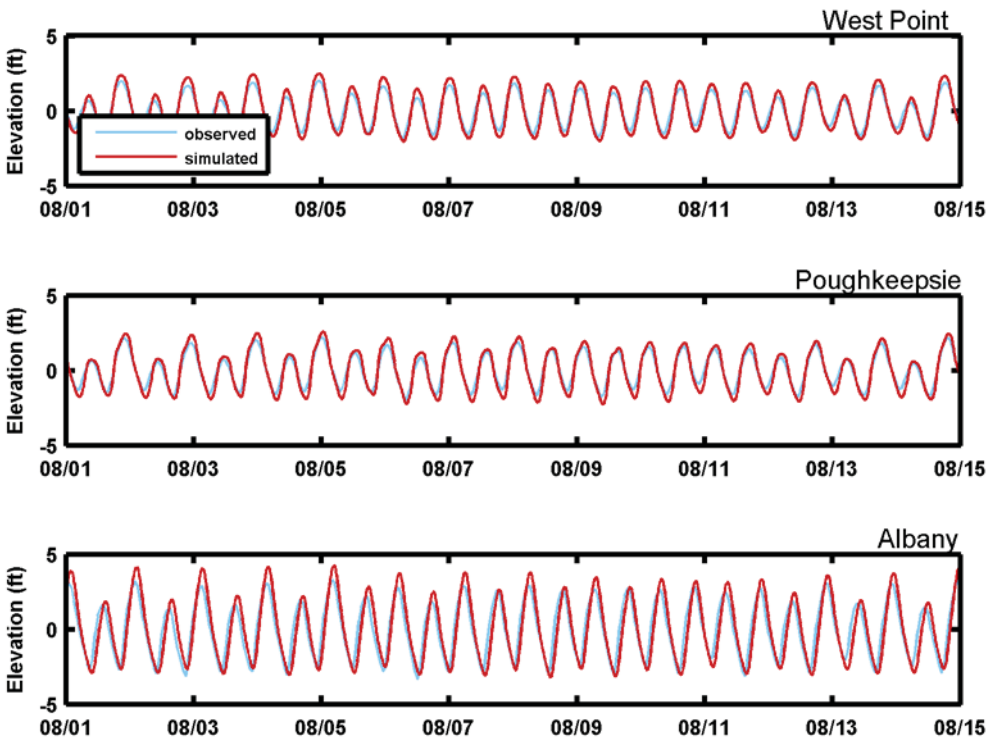

Figure 7-7 Model predicted water surface elevations compared to available observations for the Scenario time period.

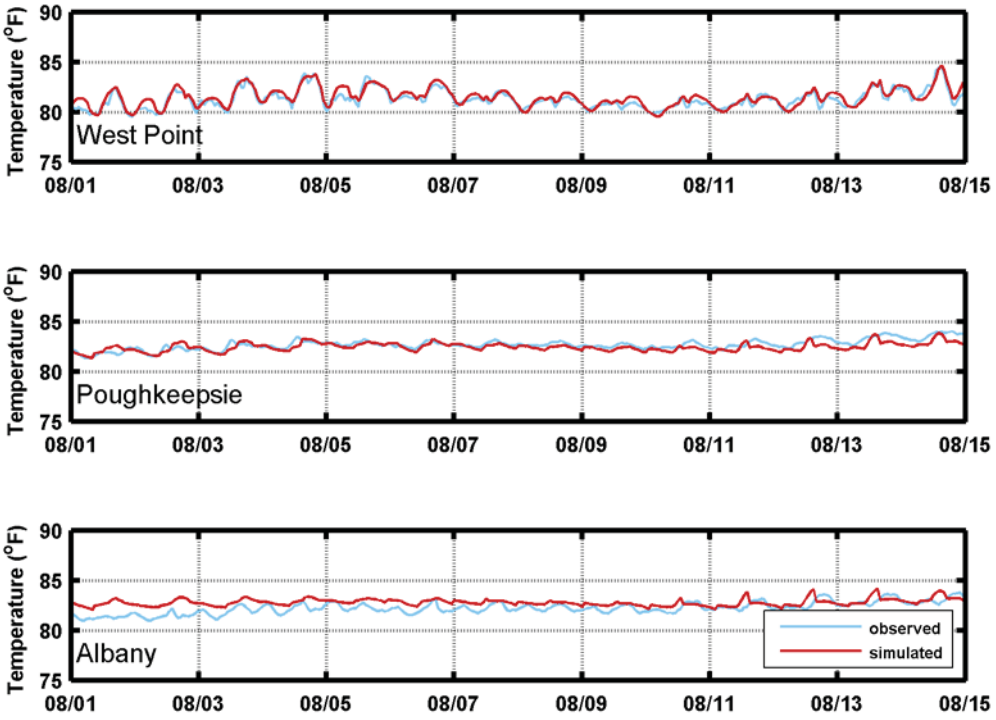

Figure 7-8 Model predicted surface water temperatures compared to available observations for the Scenario time period.

Plan view model predicted surface water temperatures, displayed as color coded contours on the map, are presented in Figure 7-9 and Figure 7-10. Figure 7-9 shows the downstream extent of the thermal plume at slack before flood and Figure 7-9 shows the upstream extent for slack before ebb for representative times during the Scenario period. As first observed in the thermistor data, and clearly shown in the figures, the thermal plume tends to hug the eastern shore of the river on both ebb and flood stages of the tide. During the slack tide stages, while transient, the currents are relatively small, allowing a buildup, or pooling of the thermal effluent, which is subsequently transported either upstream or downstream with the tidal flood or ebb, respectively. The higher temperatures tend to occur near the effluent canal during the slack tide pooling, but are rapidly dispersed with the energetic flood and ebb currents.

In addition to the thermal effluent effects in the river, there is a great deal of environmental heating and cooling, particularly in the shallower areas north of the plant in Peekskill Bay and south of the plant in Haverstraw Bay. On warmer and sunny days, these large shallow areas are rapidly heated providing a heat source to the cooler, deeper channel areas of the river. At night the opposite is true, where the large shallow areas provide a cooling the river water. The model simulation for the case with no plant in operation is used to isolate and evaluate the influence of the IPEC thermal effluent on the river from the environmental background variability.

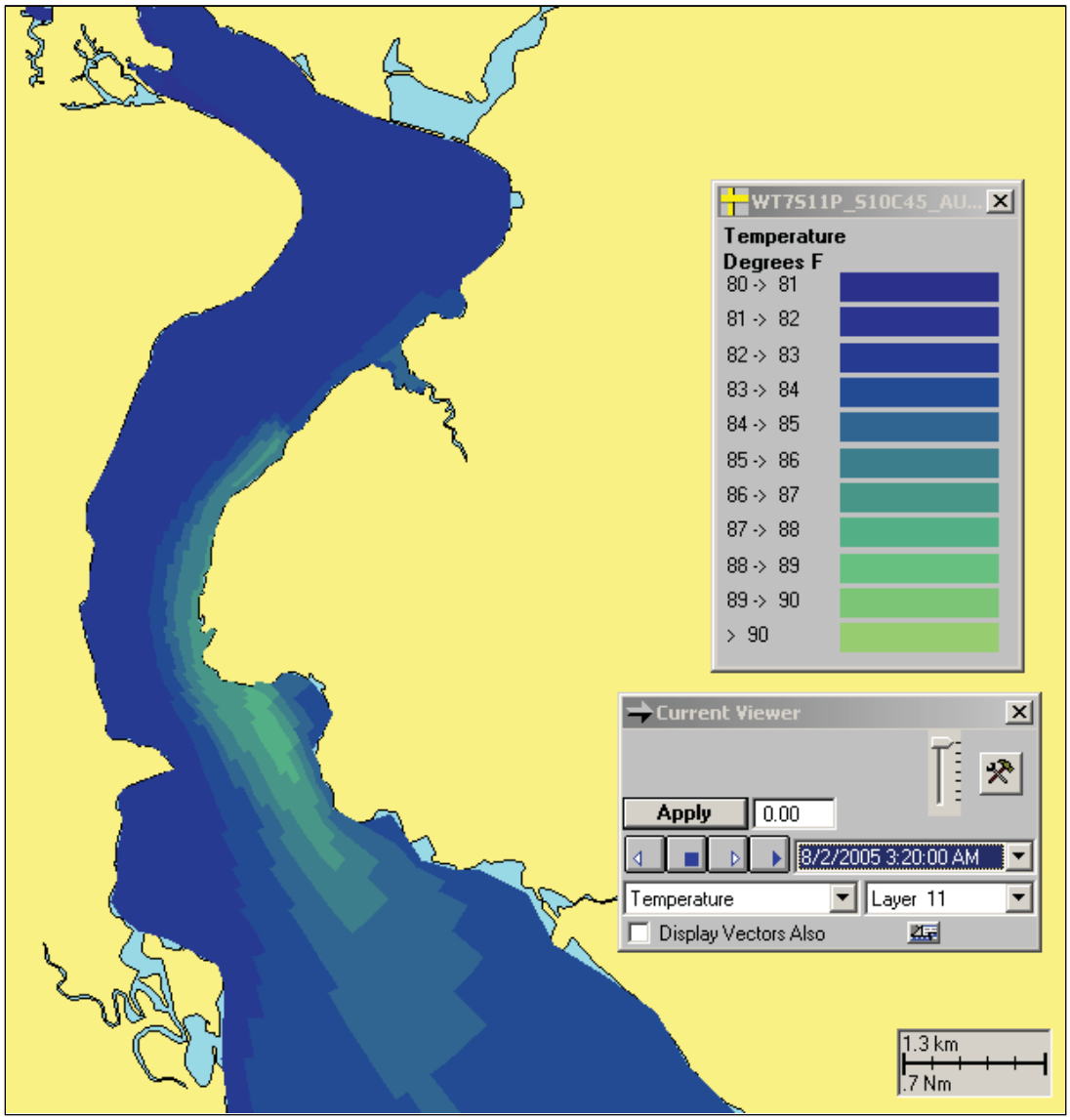

Figure 7-9 Plan view of the model predicted surface water temperatures showing the downstream extent of the plume at slack before flood during the Scenario time period.

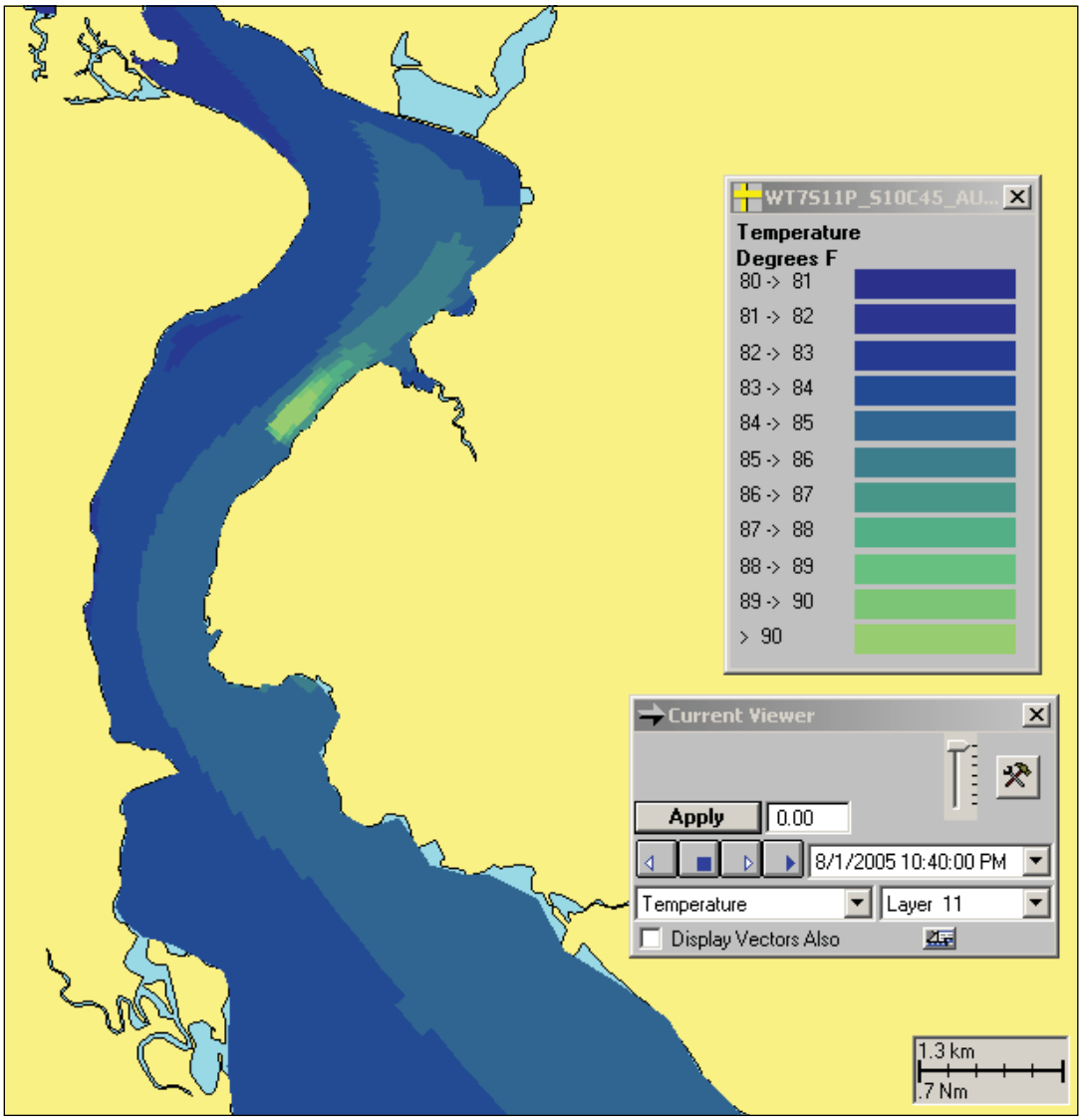

Figure 7-10 Plan view of the model predicted surface water temperatures showing the upstream extent of the plume at slack before ebb during the Scenario time period.

7.1.1. Scenario Analysis

The scenario temperature results were post-processed to determine if the plant-in-operation case showed any occurrence of water temperature greater than 90°F, the maximum allowable per WQS. The results of the 90oF analysis, presented in Figure 7-11, show that the surface area coverage is predominantly semi-diurnal (tidally driven), and remains under 35 acres during the simulation and is typically less than 20 acres. As a measure of the size of the 90°F coverage, the 35 acres is less that 0.5% of the study area (area of thermistor study deployment) and is only 0.05% of the modeled River area in general.

Figure 7-12 shows a plan view on the map, of the model predicted surface water temperatures for the Scenario time period with the largest surface area coverage greater than 90oF. The area greater than 90°F can be seen as a light green area extending offshore and north from the IPEC area. The shape of the plume is a result of the tidal stage which is at the end of the flood stage at slack water before ebb, allowing a thermal pool to build up just north of the outfall. A vertical cross sectional slice through the river and the thermal plume is also shown in the figure. A dotted black line on the map indicates the line along which the vertical section was drawn. In the section, it can be seen that the thermal plume is predominantly a surface feature again indicated by the green area in the upper right hand side of the section view.

NYSDEC has specified mixing zones in some SPDES permits for thermal discharges, whereas Indian Point has a calculation formula that infers a mixing zone, without specifying its areal extent. For instance, the Arthur Kill Generating Station, located on Staten Island and operating under SPDES Number NY-0005100, discharges a peak cooling water flow of 713 mgd and is allowed a mixing zone of 5,000,000 ft2 (115 ac). Since Indian Point (units 2 and 3 combined) discharges a maximum or design flow of 2,419 mgd, scaling by the ratio of the flows, would result in a mixing zone of 17,00,000 ft2 (390 ac). Another estimate of a mixing zone can use the ratio of heat discharged. In the absence of those numbers for each plant, the nameplate generating capacity could be used (which ignores the efficiency differences of the two stations). Assuming a 2,045 MW capacity for Indian Point and an 850 MW capacity for Arthur Kill, a mixing zone of 12,000,000 ft2 or 280 ac results.

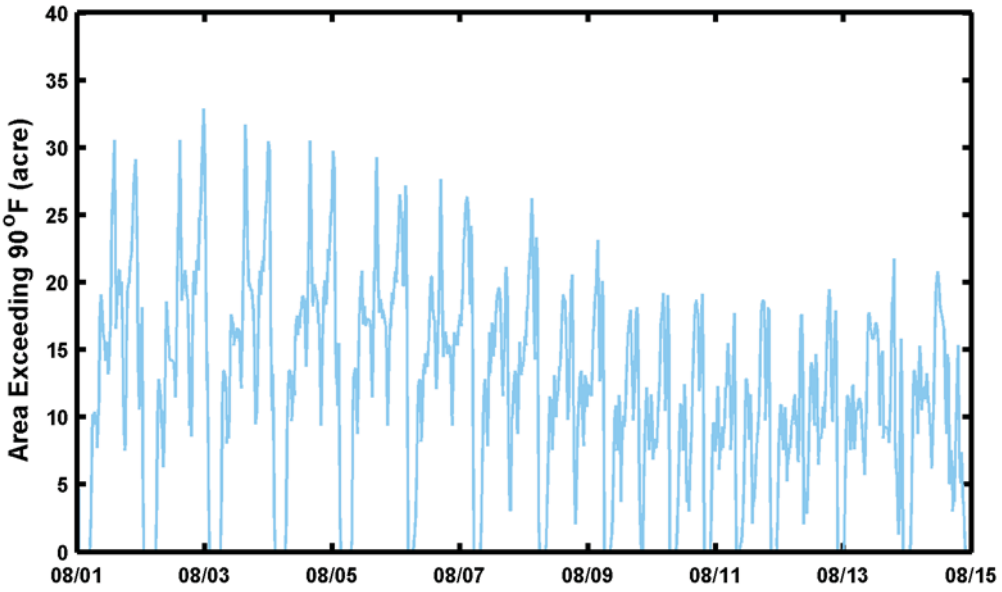

Figure 7-11 Model predicted surface area (in acres) for water temperatures greater than 90°F for the Scenario time period.

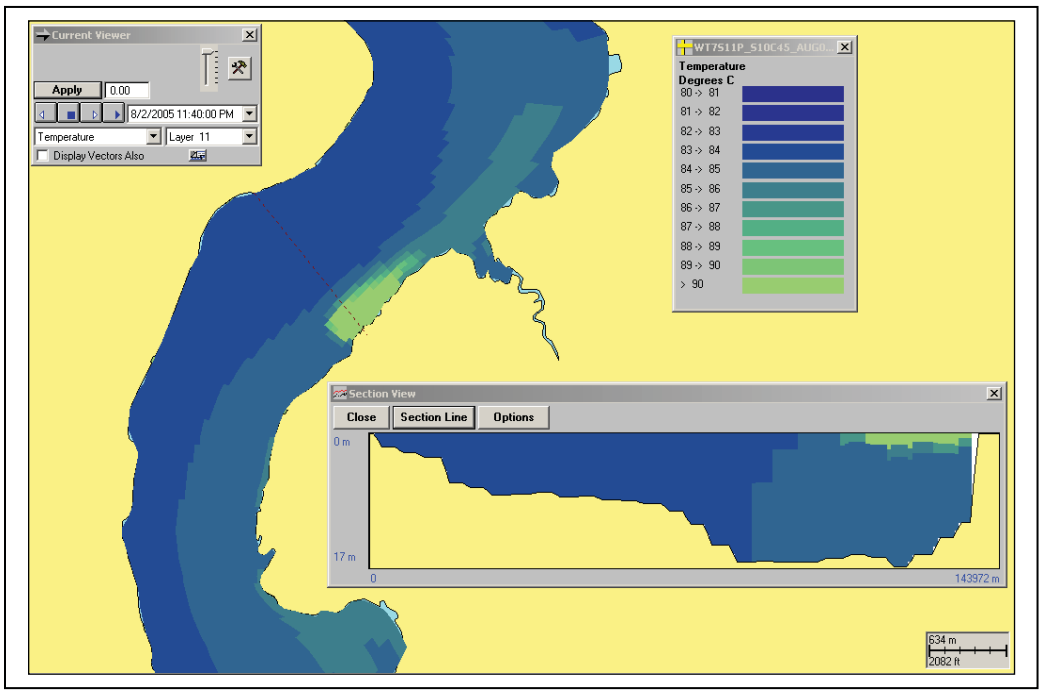

Figure 7-12 Plan view of the model predicted surface water temperatures for the Scenario time period with the largest surface area coverage greater than 90°F.

The results were further processed to determine the surface temperature difference for each model grid cell (totaling 4725 cells) between the two cases run, for every time step of the model run. This post-processing result represents the temperature rise between the IPEC's discharge and the environmental background (without the plant), thus isolating the IPEC thermal contribution. These

results were used to delineate the presence of a differential temperature greater than 4°F along representative cross sections of the River to determine either if the 67% cross-River distance or 50% cross sectional area requirements were in compliance. The transects chosen for evaluation of these metrics included one at IPEC, one at 3,000 ft (S2) and one at 1.5 miles (Stony Point) downstream from IPEC and one at 4,500 ft upstream (Charles Point) from IPEC as shown in Figure 7-13.

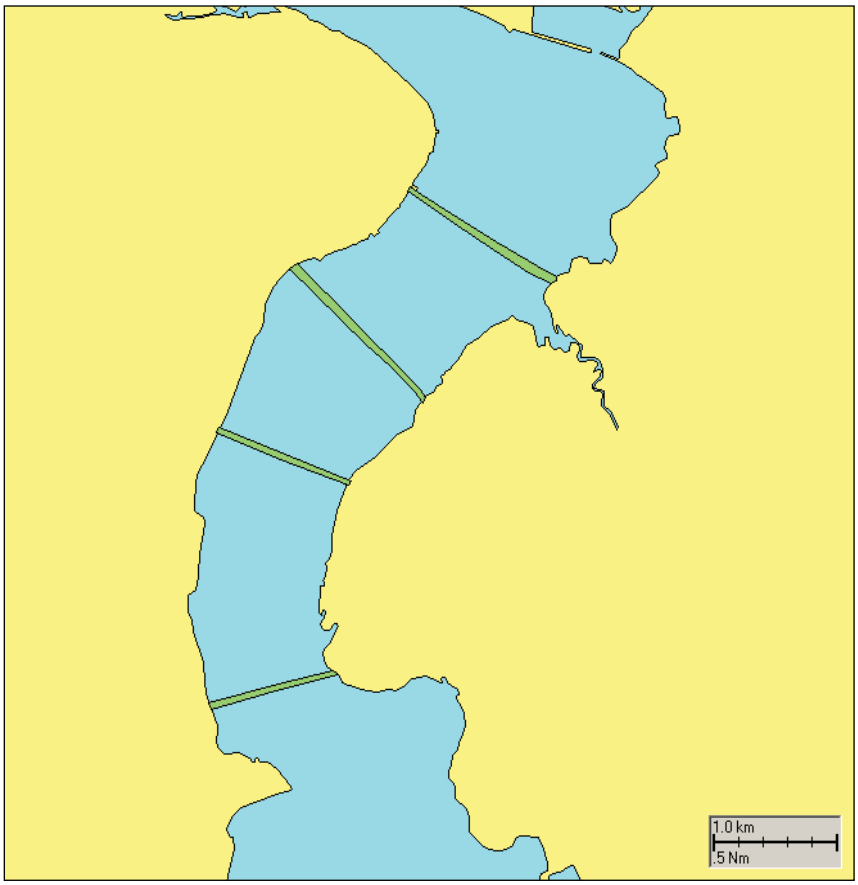

Figure 7-13 Map of the IPEC study area showing the Scenario analysis transects along the river.

A time series plot of the model predicted, percent cross-sectional area coverage of the 4°F temperature rise above ambient (without the IPEC in operation) as a function of time through the simulation period for each transect is presented in Figure 7-14. The cross-river distance of the 4°F isotherm at the surface for each transect is also presented. The model results for the simulation time period showed that the 4°F temperature rise covered less than 15% of the River vertical cross sectional area at the transects at all times during the simulation period, and generally covered less than 3% of the cross sectional area. The model results also showed that the 4°F temperature rise surface extent was less than 35% across the River at all times, and generally less than 20%. Thus, the model results show that the plant is in compliance with the NYSDEC thermal WQS set forth in 6 NYCRR §704.2(b)(5).

A plan view of the model predicted surface water delta temperature above the model predicted ambient at the time of the largest cross-sectional area coverage greater than 4°F is shown in Figure 7-15. A vertical section view of the 4°F delta temperature plume is also shown for the Stony Point transect, indicated with the dashed line on the map, where the largest cross-sectional area was

predicted. The figure illustrates the downstream, cross river and vertical extents of the 4°F plume at this critical point in time. While the plume does eventually extend farther south into the Haverstraw Bay area Figure 7-15 shows the maximum cross-sectional area and cross river surface distance.

In addition, the 1.5°F temperature rise above ambient was calculated for times when the ambient temperature exceeded 83°F within the timeframe designed in the Thermal WQS. In order to determine when the ambient River temperature exceeded the 83°F threshold, the environmental background case was evaluated at a representative station near IPEC (shown in Figure 7-16). The time when the ambient temperature exceeded 83 can clearly be seen. The exceedances occur on a daily schedule starting after mid day.

The 1.5°F temperature rise covered less than 40% of the River cross sectional area at all times, and generally covered less than 20 % of the cross sectional area (see Figure 7-17). The 1.5°F cross-river temperature rise extent at the surface was also less than 40% across the River at all times and generally less than 21%. Times of no data indicate that the ambient temperature is less than 83 F. All of these extents are consistent with the thermal WQS set forth in 6 NYCRR §704.2(b)(5).

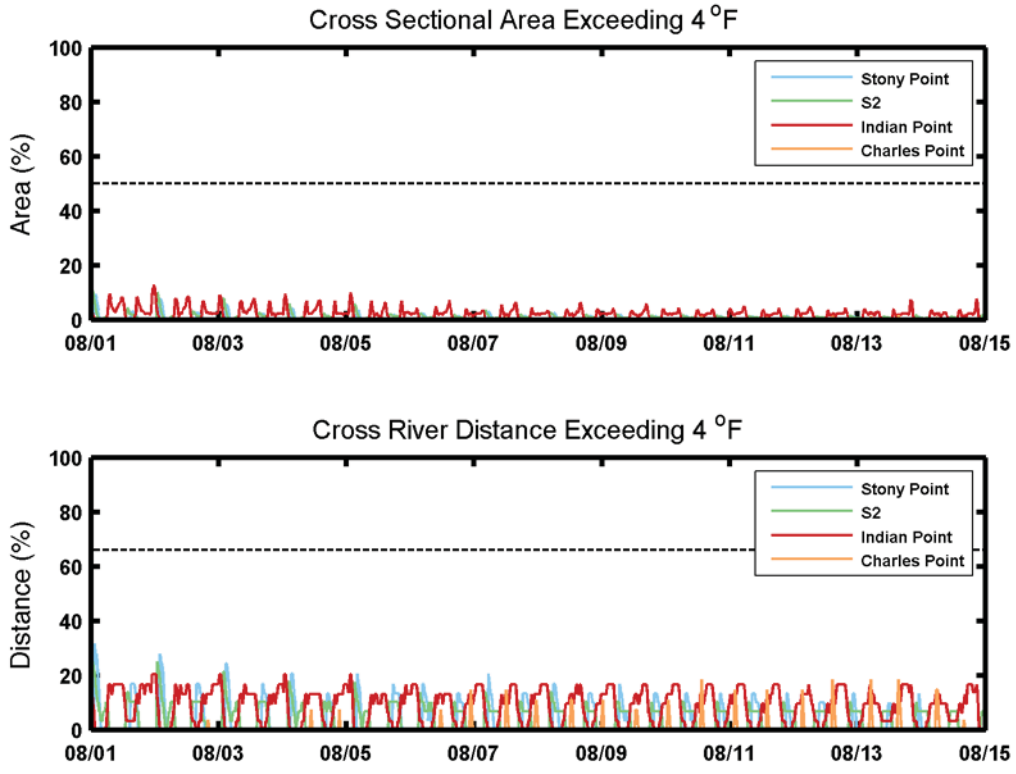

Figure 7-14 Thermal plume evaluation at the four transects for the 4°Fabove ambient isotherms for the Scenario time period. Top: cross-sectional area coverage. Bottom: cross-river distance along the surface.

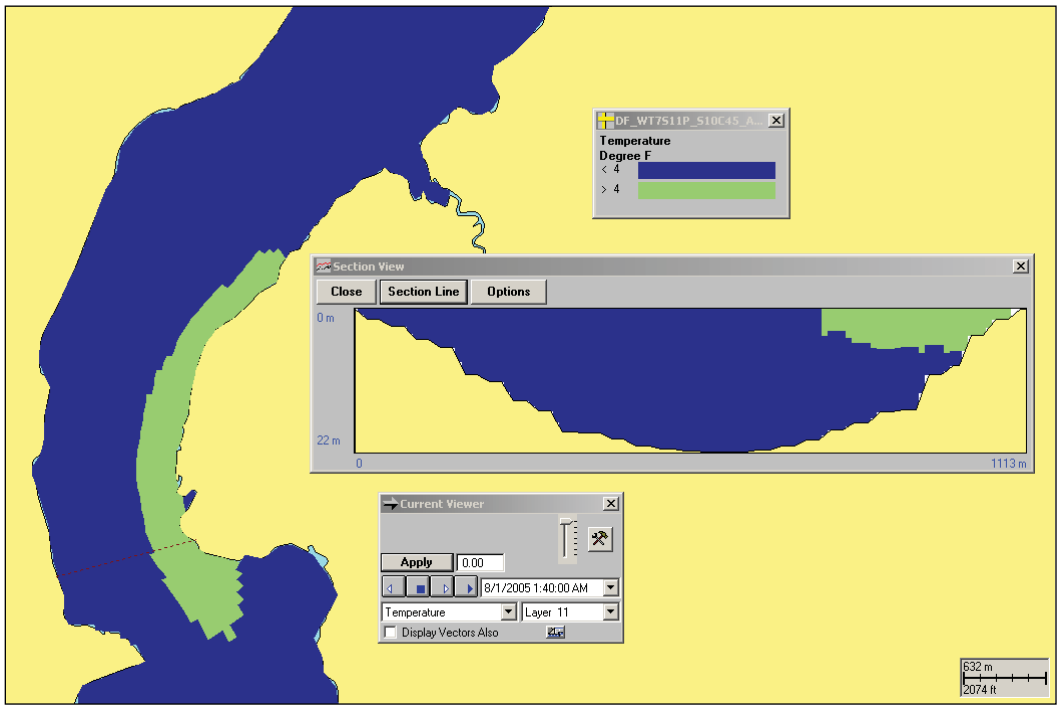

Figure 7-15 Plan view of the model predicted surface water delta temperature above model predicted ambient for the Scenario time period with the largest cross-sectional area coverage greater than 4°F.

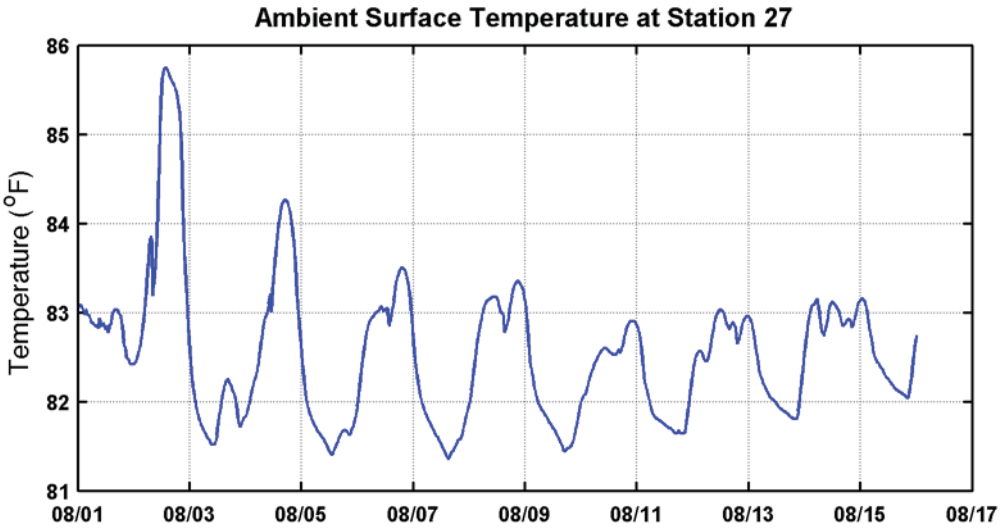

Figure 7-16 Model predicted ambient (without IPEC in operation) surface water temperature in the area of IPEC for the scenario time period.

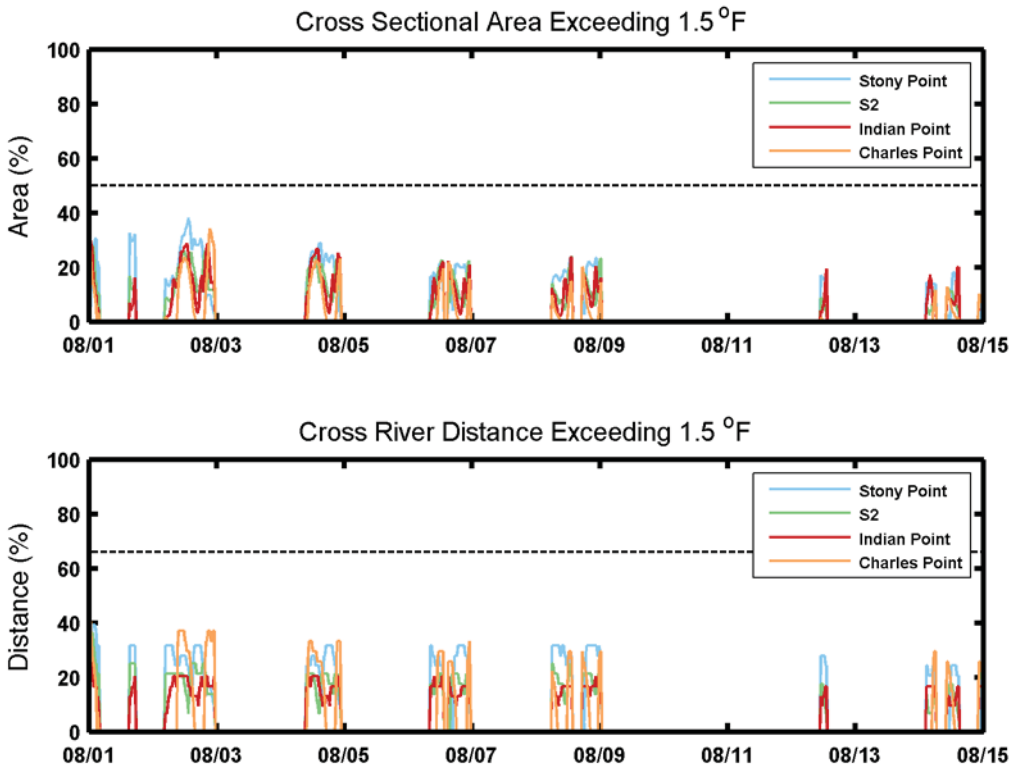

Figure 7-17 Thermal plume evaluation at the four transects for the 1.5°Fabove ambient isotherms for the Scenario time period. Top: cross-sectional area coverage. Bottom: cross-river distance along the surface.

8. Conclusions

This report describes the methodology and results of the thermal modeling component of a triaxial thermal study that consisted of a combination of field work, data analysis and numerical modeling. An initial report (Swanson et al., 2010), representing a summary of the empirical field work (Field Program), was submitted to NSYDEC on 12 February 2010, and established that IPEC's operations met Thermal WQS, as measured during the Field Program. This report focuses on the numerical modeling, which establishes that IPEC satisfies Thermal WQS during all average and extreme-case environmental conditions.

The Field Program, consisting of an fixed extensive thermistor array and mobile studies, was performed to monitor River temperatures and currents at various locations in the River from northern Haverstraw Bay (downstream) to the Bear Mountain Bridge (upstream) during a six-week period from 24 September through 3 November 2009. These data were analyzed, along with other publicly available River observations from the United States Geological Survey (USGS) and meteorological observations from the Northeast Regional Climate Center (NRCC), to first assess the dynamics of the thermal plume resulting from the IPEC discharge, and then to understand the response of the plume to various environmental forcing factors, such as tides, River water temperature and currents, as well as meteorological conditions that substantially effect thermal regimes.

The long term, fixed mooring field program used a sufficient number of thermistors (i.e., 300 thermistors on 50 moorings) to characterize the thermal structure in the River in the extended vicinity of Indian Point, accounting for the fact that the River's thermal structure varies with location, as well as with seasonal, daily, and tidal time scales. In addition, the flow data from two fixed current meters, at Indian Point and Stony Point, captured the physical dynamics – including velocity and water elevation over time -- in this area, which also influence the thermal regime. The relative contributions of different forcing mechanisms, including River flow, tide and estuarine circulation, cause temporal and spatial variability of the flow patterns. In general, bi-directional tidal flow with a period of 12.42 hours is dominant. The combined effect of River flow and salt intrusion resulted in estuarine circulation, where the surface flow was stronger during ebb while the bottom flow was stronger during flood. Also, the distinctive signal of the bi-weekly spring-neap cycle was observed at both Indian Point and Stony Point stations. In addition there are infrequent storm surge events that cause River elevations to rise and affect the regular flood and ebb tidal cycle, sometimes dramatically (e.g., elimination of the flood tide during one event). Nonetheless, during the deployment period, the combination of the surface temperatures at the upstream and downstream boundaries appears to be a reasonable proxy for surface ambient conditions.

As noted above with respect to the Field Program and as confirmed in the 12 February 2010 Report (Swanson et al., 2010), the in-River thermal monitoring data collected during the deployment period, 9 September through 1 November 2009, showed Indian Point to be in compliance with 6 NYCRR §704.2(b)(5). The surficial extent of the plume did not exceed 67% of the cross River distance, and the areal extent of the plume did not exceed 50% of the River cross sectional area. Based on the Field Program data, the thermal plume was restricted to the surface and mid depth layers in the River, never extending to the bottom layers. The Field Program was performed, consistent with a protocol provided to New York State Department of Environmental Conservation (Department) staff.

Also consistent with the protocol submitted to Department staff, the field observations and insight gained from the Field Program were then used to develop and calibrate a three dimensional hydrothermal model of an area that covered a spatial extent from Hastings on Hudson, approximately 20 miles north of the Battery, to the upstream dam at Troy (Study Area). The model domain longitudinal extent spans approximately 130 miles, the lateral extent follows the varying width of the River cross section, and the vertical extent was captured by assigning a depth to each model grid cell, which was represented in eleven vertical layers, based on bathymetric analysis. A total of 51,909 cells were used in the model calculation consisting of 4,719cells in 11 levels.

The model application used water surface elevation (tides), water temperature and salinity at the southern boundary (Hastings on Hudson), and River flow and water temperature at the northern boundary (the dam at Troy)]. Meteorological forcing, including winds, solar radiation and air temperatures, was applied at the water surface. Plant forcing data consisted of intake and discharge temperatures, as well as cooling water flows.

The model calibration was successfully performed with both qualitative and quantitative methods that represent the industry standard, providing confidence in model results. Time series comparisons of model vs. observations at the monitoring station locations were successfully established, as well as calculation of quantitative statistics, including relative mean error (RME), error coefficient of variation (ECV), square coefficient of variation (R^2) and model skill. The parameters that were evaluated in the model calibration phase were water surface elevations, currents and temperatures. Specifically, the time series of observations vs. model predictions showed that the model captured both the surface elevation variations and currents with respect to phase and amplitude. The model was able to successfully simulate the current velocities with respect to the important tidal signals in the River including semi-diurnal bi-directional flow, diurnal inequality and bi-weekly spring-neap cycle. Most importantly, the model was able to simulate both the long-term trend of decreasing water temperature, due to the changing seasons and the short-term water temperature fluctuations, due to tidal flow observed at the thermistor mooring locations.

Table 8-1 summarizes the three averaged calibration statistic metrics for water surface, current velocities, and temperature. The summary shows that the model does well at achieving the goal metrics with the water surface elevation meeting three guidance values and only slightly exceeding the fourth; the current velocities meet two of the guidance values and slightly exceed two; and, most importantly, the temperature meets all guidance values. Those metrics that are met are shown with bolded font.

Table 8-1 Model averaged calibration statistics summary.

Parameter	RME (%)	RME Goal	ECV (%)	ECV Goal	R^2	R^2 Goal	Skill	Skill Goal
Water Surface Elevation	**3**	<30	**9**	<10	0.90	>0.94	**0.96**	>0.85
Current Velocity	**6**	<30	14	<10	0.83	>0.94	**0.93**	>0.92
Temperature	**0**	<25	**1**	<45	**0.93**	>0.84	**0.94**	>0.85

Once the model was successfully calibrated, it was used with confidence to run other time periods, including extreme environmental conditions, employing the same methodology of model forcing and modeling coefficients. To do so, the model scenario timeframe for simulations was developed,

using a ten-year dataset of information based on observations compiled by USGS and NRCC. The goal of developing the scenario timeframe was to ensure that critical environmental conditions which have the largest influence on River temperature (particularly, with respect to the water quality criteria pertaining to spatial extent of the thermal plume) are captured. There were two steps in determining the time in which the influence of IPEC on the River would be most significant: a correlation analysis to determine the most influential environmental forcing factors on temperature in the River, and a joint probability analysis to determine the times at which the top three influential environmental factors synoptically occur at their individual 50^{th}, 90^{th}, 95^{th} and 99^{th} percentile values. The correlation analysis showed that the water temperatures near IPEC are most influenced by upstream River flow, water temperature and air temperature. The joint probability analysis showed that these parameters more frequently reach their higher percentile values during summer months, even more specifically during the month of August. Based on the detailed results of the joint probability analysis, the critical environmental conditions scenario timeframe was determined to be 1 August through 15 August 2005. This timeframe captures hourly occurrences of the three-way joint probability 50^{th}, 90^{th} and 95^{th} percentile conditions The 99^{th} percentile joint conditions were not found to occur naturally anytime during the 10 years of data analyzed.

Once the scenario timeframe was established, the calibrated model was then used to simulate this period for two cases; one with the plant operating at maximum capacity (5163.4 MW thermal with a flow rate of 1762.2 KGPM), and one simulating conditions with the plant not operating. The model application to the August 2005 Scenario time frame was first compared to available observations during that period. This constitutes a qualitative model validation to a consistent but small independent data set. A comparison of the model predicted water surface elevations at West Point, Poughkeepsie and Albany was made. A similar comparison for the model predicted surface water temperatures at the same USGS stations. While the modeled and observed temperature signals at Poughkeepsie and Albany are relatively uneventful, the model clearly reproduced the combined diurnal and semi-diurnal temperature signals at West Point, nearest to the upstream end of the Indian Point study area.

The scenario temperature results were post-processed to determine if the plant-in-operation case showed any occurrence of water temperature greater than 90°F, the maximum allowable per WQS. The results of the 90 °F analysis showed that the surface area coverage is predominantly semi-diurnal (tidally driven) and remains under 35 acres during the simulation period and is typically less than 20 acres. This area compares favorably to (is significantly smaller than) permitted mixing zones at other power stations along the river.

The results were further processed to determine the surface temperature difference for each model grid cell (totaling 51,909 cells) between the two cases run, for every time step of the model run. This post-processing result represents the temperature rise between the IPEC's discharge and the environmental background (without the plant), thus isolating the IPEC thermal contribution. These results were used to delineate the presence of a differential temperature greater than 4°F along representative cross sections of the River to determine either if the 67% cross-River distance or 50% cross sectional area requirements were in compliance. The transects chosen for evaluation of these metrics included one at IPEC, one at 3,000 ft (S2) and one at 1.5 miles (Stony Point) downstream from IPEC and one at 4,500 ft upstream (Charles Point).

The model results for the simulation time period showed that the 4°F temperature rise covered less than 15% of the River vertical cross sectional area at the transects at all times during the simulation period, and generally covered less than 3% of the cross sectional area. The model results also

showed that the 4°F temperature rise surface extent was less than 35% across the River at all times, and generally less than 20%. Thus the model results show that the plant is in compliance with the NYSDEC thermal WQS.

In addition, the 1.5°F temperature rise above ambient was calculated for times when the ambient temperature exceeded 83°F within the timeframe designed in the Thermal WQS. In order to determine when the ambient river temperature exceeded the 83°F threshold, the environmental background case was evaluated at a representative station near the plant. The 1.5°F temperature rise covered less than 40% of the River cross sectional area at all times, and generally covered less than 20 % of the cross sectional area. The 1.5°F cross-river temperature rise extent at the surface was also less than 40% across the River at all times and generally less than 21%. All of these extents are consistent with the thermal WQS set forth in 6 NYCRR §704.2(b)(5).

In conclusion, a field program was established to monitor the thermal plume from IPEC which was subsequently used to calibrate a numerical model representing the study area. This successfully calibrated model was then used to model extreme environmental conditions during both maximum IPEC heat rejection and a no plant heat load scenario representing ambient conditions. The results taken from the differential of these two model runs isolated the influence of IPEC on the thermal structure in the River. These results, as well as the analysis of the field data, established that the thermal plume conforms to Thermal WQS, and, therefore, that there are reasonable assurances that IPEC will operate in compliance with applicable thermal criteria during the license renewal period.

9. References

Chant, R.J. and Wilson, R.E., 2001, Secondary circulation in a highly stratified estuary, Journal of Geophysical Research, v. 102, p. 23,207 – 23,215.

EAI (Epsilon Associates, Inc.), MRI (Marine Research, Inc.) and ASA (Applied Science Associates, Inc.), 1998. Fore River station thermal discharge technical information document. Submitted on behalf of Sithe Edgar Development, LLC, ASA Project 98-018.

Enercon Services, Inc. 2009., Draft Evaluation of Alternative Intake Technologies at Indian Point Units 2&3. Report prepared for Entergy Nuclear Indian Point 2, LLC, and Entergy Nuclear Indian Point 3.

Geyer, W.R. and Chant, R.J., 2006, The physical oceanography processes in the Hudson River estuary, In: The Hudson River estuary edited by Levinton, J.S. and Waldman, J.R., p. 24-38.

Geyer, W.R., Trowbridge, J.H. and Bowen, M., 2000, The dynamics of a partially mixed estuary, Journal of Physical Oceanography, v. 30, p. 2035 – 2048.

Hudson Engineers Inc., 2009. River Water Intake Surveys. Report prepared for Entergy Nuclear.

Kim, Y.H. and Voulgaris, G., 2008, Lateral circulation and suspended sediment transport in a curved estuarine channel: Winyah Bay, SC., Journal of Geophysical Research, v. 113, C09006, doi: 10.1029/2007JC004509.

Lacy, J.R. and Monismith, S.G., 2001, Secondary currents in a curved stratified, estuarine channel, Journal of Geophysical Research, v. 106, p. 31283 – 31302.

Mendelsohn, D., 1998. A thermal environmental model for WQMAP. ASA 1998.

Neter, J. and W. Wasserman. 1974. Applied Linear Statistical models. Chapter 11, pages 371-392. Published by Richard D. Irwin, Inc., Homewood, Illinois. 842 pp.

PBR (Pritchard Al-Bassam Co. Ltd.), NAI (Normandeau Associates, Inc.) and ASA (Applied Science Associates, Inc.), 2002. Environmental impact study of seawater cooling discharges. Prepared for Royal Commission for Jubail and Yanbu, ASA Project 01-158.

Ralston,K.D., Geyer,W.R.,and Lerczak,J.A.,2007, Subtidal Salinity and Velocity in the Hudson River Estuary: Observations and Modeling. , Journal of Physical Oceonography, v. 38 no.4, p. 753-770.

Sankaranarayanan, S. 2005. A 3D boundary-fitted baratropic hydrodynamic model for the New York Harbor region. Continental Shelf Research. V25, p2233-2260.

Shahriar, E., Y. Mussalli, A. Pembroke, and J.C. Swanson. 2003. Environmental impact of heated seawater discharges in the Gulf. The 4th Middle East Refining and Petrochemicals Exhibition and Conference (Petrotech 2003), 29 September – 1 October 2003.

Swanson, C. and T. Isaji, 2001. Preliminary modeling of the RESCO facility thermal plume in the Saugus River. Report prepared for Environmental Strategic Systems, Inc., May 2001, 15 p.

Swanson, C., D. Mendelsohn, 2000. Canal station thermal plume modeling. Prepared for TRC Environmental Corporation, Lowell, MA, ASA Project 99-031.

Swanson, C., D. Mendelsohn, H. Rines, and H. Schuttenberg, 1998. Mt. Hope Bay hydrodynamic model calibration and confirmation. Submitted to New England Power Company, Westborough, MA, ASA #96-076.

Swanson, C., H.-S. Kim, and S. Sankaranarayanan, 2006. Modeling of temperature distributions in Mount Hope Bay due to thermal discharges from the Brayton Point Station. In Natural and Anthropogenic Influences on the Mount Hope Bay Ecosystem, Northeastern Naturalist, Vol 13, Special Issue 4, 145-172.

Swanson, J. C., H.-S. Kim, S. Subbayya, P. Hall, and J. Patel. 2004 (Revised). Hydrothermal Modeling of the Cooling Water Discharge from the Vermont Yankee Power Plant to the Connecticut River, Prepared for Normandeau Associates, Inc., Bedford, NH, ASA Project 02-088, 84 p. plus appendices, Applied Science Associates, Narragansett, RI.

Swanson, C., Y. Kim, D. Mendelsohn, D. Crowley and M. Mattson, 2010, Pliminary Analysis of Hudson River Thermal Data, ASA report #09-167-1. South Kingstown, RI.

Texas Instruments, 1976. A synthesis of available data pertaining to major physicochemical variables within the Hudson River Estuary emphasizing the period from 1972 to 1975. Prepared by Texas Instruments Incorporated Ecological Services, Dallas, TX. Prepared for Consolidated Edison Company of New York, Inc., New York, NY, November 1976.

United States Geological Survey . NATIONAL WATER QUALITY ASSESSMENT PROGRAM - The Hudson River Basin. 1991. http://ny.water.usgs.gov/. March 2010.

Yassuda, E., M.A. Corrêa, A.C.R. Lammardo, C.E. Simão, C. Swanson, and S. Subbayya, 2005.Hydrothermal Modeling of the Cooling Water Discharge from the Rafael Urdaneta Thermo Power Plant to the Maracaibo System. Prepared for Tecnoconsult S.A., Caracas, Venezulea, ASA Project 04-207, 49 p. plus appendices. ASA Inc. and ASA South America.

Warner, J.,Geyer, and W.R, Lerczack,J. 2005.Numerical modeling of an estuary: A comprehensive skill assessment. Journal of Geophysical Research, v. 110, C05001, doi:10.1029/2004JC0026

Appendix A: Hydrodynamic Model Description (Muin and Spaulding, 1997)

THREE-DIMENSIONAL BOUNDARY-FITTED CIRCULATION MODEL

By Muslim Muin[1] and Malcolm Spaulding[2]

ABSTRACT: A spherical coordinate, three-dimensional, nonorthogonal, boundary-fitted circulation model (contravariant formulation) for application to estuarine, coastal sea, and continental shelf waters is presented. The model employs a split mode technique where the equations are decomposed into exterior and interior modes. The exterior mode (vertically averaged) described in an earlier paper (Muin and Spaulding 1996) is solved using a semiimplicit solution technique. The interior mode (vertical structure) is solved explicitly, except for the vertical diffusion terms that are solved implicitly. The temporally and spatially varying eddy viscosity and diffusivity are determined from a turbulent kinetic energy equation and an empirically specified length scale. A series of tests are presented to evaluate model performance where analytical solutions or other numerical solutions are available for comparison. The model's ability to predict the point vertical structure of tidal flow is tested against analytic solutions employing (1) constant viscosity; and (2) an eddy viscosity varying linearly with depth with a no-slip bottom boundary condition. The ability of the model to simulate three-dimensional tidal flow was tested against an exact solution for an annular section channel with quadratically varying bathymetry. The model was also tested against analytic solutions for steady residual flow generated by density gradient, wind, and river flow in a channel. The model predicted turbulent energy distributions generated from a bottom boundary were compared to those from a previous numerical study by Davies and Jones (1990). No-slip and bottom stress formulations at the sea bed, and their effect on the vertical structure of the flow are analyzed. The model was used to predict the salinity distribution in a simple rectangular channel identical to the Rotterdam Waterway. The computational method is very economical, stable, and accurate with the CFL stability condition up to 100.

INTRODUCTION

Numerical modeling techniques are routinely used to study circulation and pollutant transport in estuarine and coastal waters. The majority of models employ finite-difference techniques on square grid systems. While this has proven useful in various applications, it becomes expensive when the study region is geometrically and bathymetrically complex. Such difficulties motivate the use of alternative solution approaches that allow flexibility in the grid specification, for example finite elements (Lynch and Werner 1987) and boundary-fitted coordinates (Johnson 1980; Spaulding 1984; Sheng 1986; Swanson 1986; Muin and Spaulding 1996).

This paper presents the extension of a two-dimensional (2D) vertically averaged, boundary fitted, spherical coordinate circulation model developed by Muin and Spaulding (1996) to three dimensions. The paper first presents the governing equations in spherical coordinates with appropriate assumptions and boundary conditions. The equations are further transformed to a σ-coordinate. This is followed by presentations of the governing equations in a generalized curvilinear coordinate system, turbulence parameterization, the solution methodology, and model testing for which analytic (linear problems) solutions or other numerical solutions are readily available. Testing emphasizes calculations of the vertical structure of the flow. Testing of the 2D vertically averaged version of the model for a series of horizontal flow problems (see Lynch and Gray 1978) was presented in Muin and Spaulding (1996).

GOVERNING EQUATIONS

Using a spherical coordinate system, where ϕ = longitude positive east; θ = latitude positive north; and r = positive up, the equations of continuity, momentum, and conservation of substance can be written as

Continuity

$$\frac{1}{r\cos\theta}\frac{\partial u}{\partial \phi}+\frac{1}{r}\frac{\partial v}{\partial \theta}-\frac{v}{r}\tan\theta+\frac{1}{r^2}\frac{\partial r^2 w}{\partial r}=0 \tag{1}$$

Momentum

ϕ-direction

$$\frac{\partial u}{\partial t}+\frac{u}{r\cos\theta}\frac{\partial u}{\partial \phi}+\frac{v}{r}\frac{\partial u}{\partial \theta}-\frac{uv}{r}\tan\theta+w\frac{\partial u}{\partial r}+\frac{uw}{r}-fv = -\frac{1}{\rho_o r\cos\theta}\frac{\partial p}{\partial \phi}+\frac{\partial}{\partial r}\left(A_v\frac{\partial u}{\partial r}\right) \tag{2}$$

θ-direction

$$\frac{\partial v}{\partial t}+\frac{u}{r\cos\theta}\frac{\partial v}{\partial \phi}+\frac{v}{r}\frac{\partial v}{\partial \theta}+\frac{uu}{r}\tan\theta+w\frac{\partial v}{\partial r}+\frac{vw}{r}+fu = -\frac{1}{\rho_o r\cos\theta}\frac{\partial p}{\partial \theta}+\frac{\partial}{\partial r}\left(A_v\frac{\partial v}{\partial r}\right) \tag{3}$$

r-direction

$$\frac{\partial p}{\partial r}=-\rho g \tag{4}$$

Conservation of Substance

$$\frac{\partial q}{\partial t}+\frac{u}{r\cos\theta}\frac{\partial q}{\partial \phi}+\frac{v}{r}\frac{\partial q}{\partial \theta}+w\frac{\partial q}{\partial r}=\frac{\partial}{\partial r}\left[D_v\left(\frac{\partial q}{\partial r}\right)\right]+\frac{D_h}{r^2}\left[\frac{\partial^2 q}{\cos^2\theta\,\partial\phi^2}+\frac{\partial^2 q}{\partial\theta^2}\right] \tag{5}$$

Equation of State of Sea Water

$$\rho=f(S,\Theta) \tag{6}$$

where t = time; u, v and w = velocity components in ϕ, θ, and r directions, respectively; f = Coriolis parameter; p = pressure; g = gravity; ρ = water density; ρ_o = basin-averaged water density; A_v = vertical eddy viscosity; D_v = vertical eddy diffusiv-

[1]Jurusan Teknik Sipil, Institut Teknologi Bandung, Bandung, Indonesia.

[2]Prof. and Chair., Dept. of Oc. Engrg., Univ. of Rhode Island, Narragansett Bay Campus, Narragansett, RI 02882.

Note. Discussion open until June 1, 1997. Separate discussions should be submitted for the individual papers in this symposium. To extend the closing date one month, a written request must be filed with the ASCE Manager of Journals. The manuscript for this paper was submitted for review and possible publication on January 10, 1994. This paper is part of the *Journal of Hydraulic Engineering*, Vol. 123, No. 1, January, 1997. ISSN 0733-9429/97/0001-0002–0012/$4.00 + $.50 per page. Paper No. 7655.

ity; D_h = horizontal eddy diffusivity; Θ = temperature °C; S = salinity (ppt); and q = concentration of a conservative substance such as Θ or S.

The equations described previously assume the following: the flow is incompressible, density differences are neglected unless multiplied by gravity (Boussinesq approximation), the vertical acceleration is very small compared to gravity (hydrostatic assumption), and the horizontal stresses are neglected.

Boundary Conditions

The land boundaries are assumed impermeable where the normal component of velocity is set to zero

$$\vec{V}\cdot\vec{n} = 0 \tag{7}$$

On river boundaries, the velocities are specified and the pressure gradient is set to zero. At open boundaries the water elevation or vertically varying velocity as a function of time is known from field observations or otherwise specified.

At closed boundaries the transport of substance is zero. At an open boundary the concentration must be specified during inflow. On outflow the substance is advected out of the model domain according to

$$\frac{\partial q}{\partial t} + \frac{u}{r\cos\theta}\frac{\partial q}{\partial \phi} = 0 \tag{8a}$$

$$\frac{\partial q}{\partial t} + \frac{v}{r}\frac{\partial q}{\partial \theta} = 0 \tag{8b}$$

At the surface, the wind stress is specified as

$$\tau_{s\phi} = \rho_a C_a W_\phi \sqrt{W_\phi^2 + W_\theta^2}, \quad \tau_{s\theta} = \rho_a C_a W_\theta \sqrt{W_\phi^2 + W_\theta^2} \tag{9}$$

where W_ϕ and W_θ = wind speeds in the ϕ and θ directions, respectively; ρ_a = density of air; and C_a = drag coefficient at the surface.

The kinematic free surface boundary condition is given as

$$w = \frac{\partial \zeta}{\partial t} + \frac{u}{r\cos\theta}\frac{\partial \zeta}{\partial \phi} + \frac{v}{r}\frac{\partial \zeta}{\partial \theta} \tag{10}$$

Two options are available to specify the bottom boundary condition

1. Bottom stress condition

$$\tau_{b\phi} = \rho_o C_b u_b \sqrt{u_b^2 + v_b^2}, \quad \tau_{b\theta} = \rho_o C_b v_b \sqrt{u_b^2 + v_b^2} \tag{11}$$

   where C_b = bottom drag coefficient; and u_b and v_b = velocity components at the bottom in the ϕ and θ directions, respectively.
2. No-slip condition

$$u_b = 0 \quad \text{and} \quad v_b = 0 \tag{12}$$

At the bottom boundary, no momentum flux is allowed and the kinematic condition is specified

$$w = -u_b\frac{1}{r\cos\theta}\frac{\partial h}{\partial \phi} - v_b\frac{1}{r}\frac{\partial h}{\partial \theta} \tag{13}$$

The governing equations are transformed to a σ-coordinate system to resolve bathymetric variations with a constant number of grids. The transformation is defined as

$$\phi = \phi', \quad \theta = \theta', \quad r = R + \zeta + (\sigma - 1)(\zeta + h)/2, \quad t = t' \tag{14}$$

The governing equations now become (dropping the primes for convenience)

Continuity

$$\frac{\partial \zeta}{\partial t} + \frac{1}{r\cos\theta}\frac{\partial uD}{\partial \phi} + \frac{1}{r}\frac{\partial vD}{\partial \theta} - \frac{vD}{r}\tan\theta + \frac{\partial \omega D}{\partial \sigma} = 0 \tag{15}$$

Momentum

ϕ-direction

$$\frac{\partial uD}{\partial t} + \frac{1}{r\cos\theta}\frac{\partial uuD}{\partial \phi} + \frac{1}{r}\frac{\partial uvD}{\partial \theta} - \frac{2uvD}{r}\tan\theta + \frac{\partial u\omega D}{\partial \sigma} - fvD$$
$$= -\frac{gD}{2\rho_o r\cos\theta}\left\{[\lambda + (\rho_s - 2\rho)(1-\sigma)]\frac{\partial D}{\partial \phi} + (4\rho - 2\rho_s)\frac{\partial \zeta}{\partial \phi} + D\frac{\partial \lambda}{\partial \phi}\right\} + \frac{4}{D}\frac{\partial}{\partial \sigma}\left(A_v\frac{\partial u}{\partial \sigma}\right) \tag{16}$$

θ-direction

$$\frac{\partial vD}{\partial t} + \frac{1}{r\cos\theta}\frac{\partial uvD}{\partial \phi} + \frac{1}{r}\frac{\partial vvD}{\partial \theta} - \frac{uu - vv}{r}D\tan\theta + \frac{\partial v\omega D}{\partial \sigma} + fuD = -\frac{gD}{2\rho_o r}\left\{[\lambda + (\rho_s - 2\rho)(1-\sigma)]\frac{\partial D}{\partial \theta} + (4\rho - 2\rho_s)\frac{\partial \zeta}{\partial \theta} + D\frac{\partial \lambda}{\partial \theta}\right\} + \frac{4}{D}\frac{\partial}{\partial \sigma}\left(A_v\frac{\partial v}{\partial \sigma}\right) \tag{17}$$

σ-direction

$$\frac{2}{D}\frac{\partial p}{\partial \sigma} = -\rho g \tag{18}$$

Conservation of Substance

$$\frac{\partial q}{\partial t} + \frac{u}{r\cos\theta}\frac{\partial q}{\partial \phi} + \frac{v}{r}\frac{\partial q}{\partial \theta} + \omega\frac{\partial q}{\partial \sigma} = \frac{4}{D^2}\frac{\partial}{\partial \sigma}\left[D_v\left(\frac{\partial q}{\partial \sigma}\right)\right] + \frac{D_h}{r^2}\left(\frac{\partial^2 q}{\cos^2\theta\,\partial\phi^2} + \frac{\partial^2 q}{\partial \theta^2}\right) \tag{19}$$

where

$$\lambda = \int_\sigma^1 \rho\, d\sigma \tag{20a}$$

$$\omega = -\frac{1}{D}(1+\sigma)\frac{\partial \zeta}{\partial t} + \gamma_\phi u + \gamma_\theta v + \frac{2}{D}w \tag{20b}$$

$$\gamma_\phi = \frac{1}{D}\left[\frac{1-\sigma}{r\cos\theta}\frac{\partial h}{\partial \phi} - \frac{1+\sigma}{r\cos\theta}\frac{\partial \zeta}{\partial \phi}\right] \tag{20c}$$

$$\gamma_\theta = \frac{1}{D}\left[\frac{1-\sigma}{r\cos\theta}\frac{\partial h}{\partial \theta} - \frac{1+\sigma}{r\cos\theta}\frac{\partial \zeta}{\partial \theta}\right] \tag{20d}$$

where $D = h + \zeta$ = total water depth.

The horizontal velocities and independent variables are next transformed to a curvilinear coordinate system. The equations of motion and continuity equation in a curvilinear coordinate system (ξ, η), in terms of the contravariant velocity components, are as follows:

Continuity

$$Jr\cos\theta\frac{\partial \zeta}{\partial t} + \frac{\partial}{\partial \xi}(\cos\theta Ju^c D) + \frac{\partial}{\partial \eta}(\cos\theta Jv^c D) + Jr\cos\theta\frac{\partial(\omega D)}{\partial \sigma} = 0 \tag{21}$$

Momentum Equation

ξ-direction

$$\frac{\partial u^c D}{\partial t} = -\frac{\theta_\eta\theta_\eta + \cos^2\theta\phi_\eta\phi_\eta}{J^2\rho_o r\cos^2\theta}\frac{Dg}{2}\left\{[\lambda + (\rho_s - 2\rho)(1-\sigma)]\frac{\partial D}{\partial \xi} + (4\rho - 2\rho_s)\frac{\partial \zeta}{\partial \xi} + D\frac{\partial \lambda}{\partial \xi}\right\} + \frac{\theta_\xi\theta_\eta + \cos^2\theta\phi_\xi\phi_\eta}{J^2\rho_o r\cos^2\theta}\frac{Dg}{2} \cdot\left\{[\lambda + (\rho_s - 2\rho)(1-\sigma)]\frac{\partial D}{\partial \eta} + (4\rho - 2\rho_s)\frac{\partial \zeta}{\partial \eta} + D\frac{\partial \lambda}{\partial \eta}\right\} - \frac{\theta_\eta}{J^2 r\cos^2\theta}\left[\frac{\partial}{\partial \xi}(\phi_\xi\cos^2\theta J u^c u^c D + \phi_\eta\cos^2\theta J u^c v^c D) + \frac{\partial}{\partial \eta}(\phi_\xi\cos^2\theta J u^c v^c D + \phi_\eta\cos^2\theta J v^c v^c D)\right] + \frac{\phi_\eta}{J^2 r\cos^2\theta}\left[\frac{\partial}{\partial \xi}(\theta_\xi\cos^2\theta J u^c u^c D + \theta_\eta\cos^2\theta J u^c v^c D) + \frac{\partial}{\partial \eta}(\theta_\xi\cos^2\theta J u^c v^c D + \theta_\eta\cos^2\theta J v^c v^c D)\right] - \frac{\partial}{\partial \sigma}(\omega u^c D) + \frac{fD}{J\cos\theta}[(\theta_\xi\theta_\eta + \cos^2\theta\phi_\xi\phi_\eta)u^c + (\theta_\eta\theta_\eta + \cos^2\theta\phi_\eta\phi_\eta)v^c] + \frac{4}{D}\frac{\partial}{\partial \sigma}\left(A_v\frac{\partial u^c}{\partial \sigma}\right) \tag{22}$$

η-direction

$$\frac{\partial v^c D}{\partial t} = \frac{\theta_\eta\theta_\xi + \cos^2\theta\phi_\eta\phi_\xi}{J^2\rho_o r\cos^2\theta}\frac{Dg}{2}\left\{[\lambda + (\rho_s - 2\rho)(1-\sigma)]\frac{\partial D}{\partial \xi} + (4\rho - 2\rho_s)\frac{\partial \zeta}{\partial \xi} + D\frac{\partial \lambda}{\partial \xi}\right\} - \frac{\theta_\xi\theta_\xi + \cos^2\theta\phi_\xi\phi_\xi}{J^2\rho_o r\cos^2\theta}\frac{Dg}{2} \cdot\left\{[\lambda + (\rho_s - 2\rho)(1-\sigma)]\frac{\partial D}{\partial \eta} + (4\rho - 2\rho_s)\frac{\partial \zeta}{\partial \eta} + D\frac{\partial \lambda}{\partial \eta}\right\} + \frac{\theta_\xi}{J^2 r\cos^2\theta}\left[\frac{\partial}{\partial \xi}(\phi_\xi\cos^2\theta J u^c u^c D + \phi_\eta\cos^2\theta J u^c v^c D) + \frac{\partial}{\partial \eta}(\phi_\xi\cos^2\theta J u^c v^c D + \phi_\eta\cos^2\theta J v^c v^c D)\right] - \frac{\phi_\xi}{J^2 r\cos^2\theta}\left[\frac{\partial}{\partial \xi}(\theta_\xi\cos^2\theta J u^c u^c D + \theta_\eta\cos^2\theta J u^c v^c D) + \frac{\partial}{\partial \eta}(\theta_\xi\cos^2\theta J u^c v^c D + \theta_\eta\cos^2\theta J v^c v^c D)\right] - \frac{\partial}{\partial \sigma}(\omega v^c D) - \frac{fD}{J\cos\theta}[(\theta_\xi\theta_\xi + \cos^2\theta\phi_\xi\phi_\xi)u^c + (\theta_\xi\theta_\eta + \cos^2\theta\phi_\xi\phi_\eta)v^c] + \frac{4}{D}\frac{\partial}{\partial \sigma}\left(A_v\frac{\partial v^c}{\partial \sigma}\right) \tag{23}$$

Conservation of Substance

$$\frac{\partial q}{\partial t} + \frac{u^c}{r}\frac{\partial q}{\partial \xi} + \frac{v^c}{r}\frac{\partial q}{\partial \eta} + \omega\frac{\partial q}{\partial \sigma} = \frac{4}{D^2}\frac{\partial}{\partial \sigma}\left(D_v\frac{\partial q}{\partial \sigma}\right) + \frac{D_h}{r^2 J^2} \cdot\left[\left(\frac{\theta_\eta\theta_\eta}{\cos^2\theta} + \phi_\eta\phi_\eta\right)\frac{\partial^2 q}{\partial \xi^2} - 2\left(\frac{\theta_\xi\theta_\eta}{\cos^2\theta} + \phi_\xi\phi_\eta\right)\frac{\partial^2 q}{\partial \xi\partial \eta} + \left(\frac{\theta_\xi\theta_\xi}{\cos^2\theta} + \phi_\xi\phi_\xi\right)\frac{\partial^2 q}{\partial \eta^2}\right] \tag{24}$$

where u^c and v^c = contravariant velocities in the (ξ, η) directions, respectively; ζ = water elevation; $D = \zeta$ + depth; and the Jacobian, $J = \phi_\xi\theta_\eta - \phi_\eta\theta_\xi$. The relationship between the contravariant velocities (u^c, v^c) and velocities in spherical coordinates (u, v) is given by

$$u = \cos\theta\phi_\xi u^c + \cos\theta\phi_\eta v^c \tag{25a}$$

$$v = \theta_\xi u^c + \theta_\eta v^c \tag{25b}$$

TURBULENCE PARAMETERIZATION

The turbulence parameterization is a key model component for predicting flow and mixing processes in stratified fluids. There is, however, no universally accepted procedure to represent turbulence (ASCE 1988; Cheng and Smith 1990). In this study, we employ a one equation turbulent kinetic energy model to calculate the vertical eddy viscosity and diffusivity. The length scale is specified using the approach suggested by Blackadar (1962) that has been successfully used in modeling turbulence for tidal problems (Davies and Jones 1990). The effect of stratification is accounted for by using an empirical relationship similar to the ones employed for the mixing length approach. This model accounts for the convection, diffusion, and time history of turbulent kinetic energy in unsteady flows.

Turbulent Energy

The turbulence kinetic energy equation in spherical and σ-coordinates is given as follows:

$$\frac{\partial b}{\partial t} + \frac{u}{r\cos\theta}\frac{\partial b}{\partial \phi} + \frac{v}{r}\frac{\partial b}{\partial \theta} + \omega\frac{\partial b}{\partial \sigma} = \frac{4}{D^2}\frac{\partial}{\partial \sigma}\left(\frac{A_v}{\sigma_b}\frac{\partial b}{\partial \sigma}\right) + A_v\left[\left(\frac{2}{D}\frac{\partial u}{\partial \sigma}\right)^2 + \left(\frac{2}{D}\frac{\partial v}{\partial \sigma}\right)^2\right] + \beta g\frac{2A_v}{D\sigma_t}\frac{\partial \Phi}{\partial \sigma} - \varepsilon \tag{26}$$

where b = kinetic energy.

After transformation to curvilinear coordinates (ξ, η), the preceding equation can be written as

$$\frac{\partial b}{\partial t} + \frac{u^c}{r}\frac{\partial b}{\partial \xi} + \frac{v^c}{r}\frac{\partial b}{\partial \eta} + \omega\frac{\partial b}{\partial \sigma} = \frac{4}{D^2}\frac{\partial}{\partial \sigma}\left(\frac{A_v}{\sigma_b}\frac{\partial b}{\partial \sigma}\right) + A_v\left[\left(\frac{2}{D}\frac{\partial u}{\partial \sigma}\right)^2 + \left(\frac{2}{D}\frac{\partial v}{\partial \sigma}\right)^2\right] + \beta g\frac{2A_v}{D\sigma_t}\frac{\partial \Phi}{\partial \sigma} - \varepsilon \tag{27}$$

where β = volumetric expansion coefficient; σ_b = empirical diffusion constant; σ_t = Schmidt number; Φ = mean scalar quantity; and ε = dissipation. In this study the interchange between turbulent kinetic energy and potential energy or production/dissipation by buoyant forces is neglected. It is assumed that the turbulent kinetic energy is advected and diffused in a homogeneous fluid while the effect of stratification is accounted for by an empirical formula using a Richardson number (damping function). As argued by Abraham (1988), the reproduction of internal mixing at tidal slack is beyond the capability of present turbulence models and, hence, they should not be used where this aspect is important.

Eddy Viscosity and Diffusivity Relationships

Based on dimensional reasoning the eddy viscosity is related to the kinetic energy b and mixing length L_m by

$$A_v = C_\mu L_m\sqrt{b} \tag{28}$$

where C_μ = empirical constant.

In homogeneous water, the vertical eddy viscosity and diffusivity are considered to be equal, $A_v = D_v$. In the presence of a stable vertical density gradient, both A_v and D_v are lower than their homogeneous values. The magnitude of A_v is always greater than the corresponding value of D_v.

The general form for the eddy viscosity and diffusivity are given as

$$A_v = f(R_i) C_\mu L_m \sqrt{b} \tag{29a}$$

$$D_v = g(R_i) C_\mu L_m \sqrt{b} \tag{29b}$$

Several semiempirical relations for $f(R_i)$ and $g(R_i)$ have been proposed by Munk and Anderson (1948) and Officer (1976).

Munk and Anderson (1948)

$$f(R_i) = (1 + 10.0R_i)^{-1/2} \tag{30a}$$

$$g(R_i) = (1 + 3.33R_i)^{-3/2} \tag{30b}$$

Officer (1976)

$$f(R_i) = (1 + R_i)^{-1} \tag{31a}$$

$$g(R_i) = (1 + R_i)^{-2} \tag{31b}$$

where the Richardson number, R_i, is defined by

$$R_i = -\frac{2g}{\rho D} \frac{\dfrac{\partial \rho}{\partial \sigma}}{\left[\dfrac{\partial(u)}{\partial \sigma}\right]^2 + \left[\dfrac{\partial(v)}{\partial \sigma}\right]^2} \tag{32}$$

Dissipation

From dimensional analysis the expression for dissipation, in terms of the turbulent kinetic energy and mixing length, is given by

$$\varepsilon = C_d (b^{3/2}/L_m) \tag{33}$$

where C_d = empirical constant.

Mixing Length

The mixing length formulation proposed by Blackadar (1962) is

$$L_m = \frac{KD[1 + (\sigma - 1)/2]}{1 + \dfrac{KD[1 + (\sigma - 1)/2]}{L_o}} \tag{34}$$

where K = Von Karman's constant; D = total water depth and in which the mixing length, L_m, increases from the sea bottom to the surface and the value of L_o is determined by the vertical distribution of the turbulent energy as follows:

$$L_o = \gamma D \frac{\displaystyle\int_{-1}^{1} b^{1/2}[1 + (\sigma - 1)/2]\, d\sigma}{\displaystyle\int_{-1}^{1} b^{1/2}\, d\sigma} \tag{35}$$

The constant γ determines the vertical extent of the boundary layer and vertical eddy viscosity, and is adjusted to match field observations. The viscosity increases rapidly with increasing γ in both amplitude and vertical extent (Mofjeld and Lavelle 1983). The constant γ typically ranges from 0.05 to 0.3. The coefficients in (28), (34), and (35) have values C_μ = 0.463; C_d = 0.1; σ_b = 1.37; and K = 0.4 (Davies and Jones 1990).

Boundary Conditions

The boundary condition at the surface is specified as

$$\frac{2\alpha_b A_v}{D} \frac{\partial b}{\partial \sigma} = \alpha_w U_{*_s}^3 \tag{36}$$

where U_{*_s} = friction velocity due to the wind stress and α_b, α_w are coefficients. A similar boundary condition is used by Davies and Jones (1988) in which α_b = 0.73, and α_w = 2.6. In the absence of wind forcing the flux of turbulence at the surface disappears.

For a no-slip bottom boundary condition, the turbulent kinetic energy flux into the sea bed is zero (Davies and Jones 1988) and, therefore

$$\frac{\partial b}{\partial \sigma} = 0 \tag{37}$$

For the bottom stress boundary condition, the bottom boundary layer is not resolved in detail. The turbulent kinetic energy, b, at the first grid point near the wall (where the turbulence is assumed in equilibrium and the velocity follows the log-law) is given as follows:

$$b = U_{*_b}^2 / \sqrt{C_\mu C_d} \tag{38}$$

where U_{*_b} = friction velocity associated with the bottom stress. While this boundary condition is not always rigorously satisfied under unsteady conditions (Celik and Rodi 1985), it is used as a first-order approximation.

SOLUTION TECHNIQUE

The basic approach is to transform the dependent, as well as independent, variables in spherical coordinates to a curvilinear coordinate system. The equation of motion is split into exterior and interior modes to increase the allowable time step and, hence, reduce the computational time.

The velocity is decomposed into

$$u^c = U^c + u^{c\prime} \tag{39a}$$

$$v^c = V^c + v^{c\prime} \tag{39b}$$

where (U^c, V^c) and $(u^{c\prime}, v^{c\prime})$ = vertically averaged velocities and deviation velocity (from the vertically averaged velocity) in (ξ, η) directions, respectively. Solution of the exterior mode using a semiimplicit (space staggered grid) solution, methodology, and presentations of the approach used to generate the boundary conforming grid are presented by Muin and Spaulding (1996). The focus here is on three-dimensional (3D) aspects, including the deviation velocity and the turbulence equation.

Subtracting the vertically averaged momentum equations from the 3D momentum equations gives the vertical deviation velocity equations of motion

$$\frac{\partial u^{c\prime} D}{\partial t} = \frac{4}{D} \frac{\partial}{\partial \sigma} \left(A_v \frac{\partial u^{c\prime}}{\partial \sigma} \right) + A \tag{40a}$$

$$\frac{\partial v^{c\prime} D}{\partial t} = \frac{4}{D} \frac{\partial}{\partial \sigma} \left(A_v \frac{\partial v^{c\prime}}{\partial \sigma} \right) + B \tag{40b}$$

where A and B = nonbarotropic terms in the equations of motion. These terms are solved explicitly. The diffusion term in (40) is solved implicitly using a three-level scheme to damp out spurious oscillations (Fletcher 1988). The algorithm is second-order accurate both in time and spece. A tridiagonal set of equations in the unknown velocity deviation is solved using a Thomas algorithm. Both the exterior and interior modes are solved at the same time step.

The finite difference procedure used to solve the turbulent kinetic energy equations has been described by Davies and Jones (1990). In the present study, a three-level time discretization (Fletcher 1988) is used instead of the Crank-Nicholson method of Davies and Jones (1990). A nonstaggered grid is used in the vertical. The C form of Davies and Jones' (1990) numerical scheme is employed to calculate the dissipation term

in the energy equation to ease the time step restriction. No iteration or filtering is employed. The time step is restricted by the horizontal advection term. As will be shown in model testing, a CFL equal to 100 can be used to predict the vertical structure of tidally induced flows.

The transport model (24) is solved by a simple explicit technique, except for the vertical diffusion that is solved by an implicit scheme to ease the time step restriction due to the small vertical length scale. In the present model, two options are available to solve the advection term. The first option is a Lax-Wendroff scheme, which is consistent with a second-order truncation error (Fletcher 1988). The second option is an upwind-differencing scheme (first-order accurate) that introduces artificial diffusivity. The horizontal diffusion term is solved by a centered-in-space, explicit technique. The diffusive and advective stability criteria in these numerical techniques are $\Delta t < \Delta s^2/(2D_h)$, and $\Delta t < \Delta s/U_s$, where Δs and U_s = horizontal grid size and velocity, respectively. To avoid spatial oscillations, the Lax-Wendroff scheme requires $D_h > U_s\Delta s/2$. This gives approximately the same amount of artificial viscosity as inherent in the upwind scheme.

MODEL TESTING

Model formulation and implementation, in computer code, were compared to analytical solutions in which the nonlinear convective acceleration and Coriolis terms were removed and the governing equations solved on a spherical coordinate system, which because of the limited domain approximated a Cartesian grid. Additional test simulations were performed to confirm the operation of the turbulent closure equations to predict the vertical structure of tidal flow and compared to a previous numerical study by Davies and Jones (1990). The model was tested in an application to salinity intrusion in a simple rectangular channel representative of the Rotterdam Waterway.

Residual Flow

The ability of the model to predict residual flow was tested for a basin with vertically constant density and viscosity. The surface boundary was forced by a constant wind stress if wind forcing was used. The test was performed in a simple, rectangular, and constant depth channel open at one end (west). The model was run for two bottom boundary conditions: (1) no-slip condition; and (2) bottom stress condition.

Following Officer's (1976) approach and neglecting advection, the horizontal diffusion of momentum, and the cross channel terms (equations laterally averaged), the steady-state expression for the vertical velocity profiles with linearized bottom friction can be given as follows

$$u = -g\Lambda\left(\frac{z^3}{6\rho A_v} + \frac{h^2}{2\rho k} + \frac{h^3}{6\rho A_v}\right) - g\iota\left(\frac{h}{k} + \frac{h^2}{2A_v} - \frac{z^2}{2A_v}\right) + \frac{\tau_s}{\rho}\left(\frac{1}{k} + \frac{h}{A_v} + \frac{z}{A_v}\right) \quad (41)$$

where

$$g\iota = \frac{\left[-g\Lambda\left(\frac{h^3}{2\rho k} + \frac{h^4}{8\rho A_v}\right) + \frac{\tau_s}{\rho}\left(\frac{h}{k} + \frac{h^2}{2A_v}\right) - hu_o\right]}{\left(\frac{h^2}{k} + \frac{h^3}{3A_v}\right)} \quad (42)$$

where Λ = horizontal density gradient; g = gravity; ι = water elevation slope; τ_s = wind stress; u_o = river flow per width; and k = linearized bottom friction. A similar equation for a no-slip condition at the bottom is given on page 120 of Officer (1976).

Three separate simulations with different forcings were studied: (1) density gradient flow; (2) wind driven flow; and (3) density gradient, wind, and river-induced flow. In these simulations, the following conditions were assumed: the density increases linearly from the head (closed end) to the mouth (open end) $\Lambda = -0.00036$ kg/m^4; wind stress $\tau_s = 0.01$ N/m^2 (1 dyne/cm^2); river flow $u_o = -0.1$ m/s; depth $h = 10$ m; vertical viscosity $A_v = 10$ cm^2/s; and linearized bottom friction $k = 0.05$ cm/s. Depending on the case the appropriate forcing parameters were used. Testing was performed using five, 10, and 20 vertical levels. The model was started with zero velocities and elevation. The density gradient was applied gradually until a steady state was achieved.

Density Gradient Forcing

Fig. 1(a) shows a comparison of the model prediction to analytic solution for the bottom stress formulation under density gradient forcing. Model predictions approach the analytic solution as the grid resolution is increased. The model overpredicts the currents near the bottom and surface at low grid resolution. The maximum errors are about 7% for five levels, 2% for 10 levels, and less than 1% for 20 levels. The model was also run with a no-slip bottom boundary condition, as shown in Fig. 1(b). When the surface boundary condition was specified using a second-order accurate representation, the model never reached steady state even with 80 levels. This problem may be caused by an underestimate of the bottom friction, which is only first-order accurate. The model, however, reached steady state when the surface boundary was reduced to first order. For this approximation the model overpredicted the velocity near the surface by 20% [Fig. 1(b)] independent of the number of the vertical levels.

Wind Forcing

Comparison of model predictions with the analytic solution under constant wind forcing with a bottom stress condition is

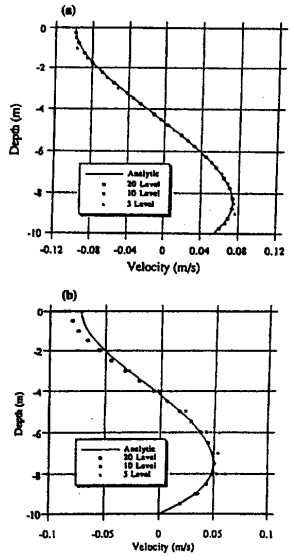

FIG. 1. Comparison of Model Predicted Vertical Structure of Velocity with Analytic Solution for Density-Induced Forcing (A_v = 10 cm^2/s, $\Lambda = -0.00036$ kg/m^4, $k = 0.05$ cm/s) for: (a) Bottom Stress; and (b) No-Slip Bottom Boundary Condition (Model Results Are Presented for 5, 10, and 20 Vertical Levels)

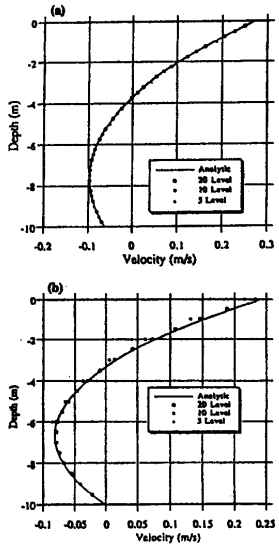

FIG. 2. Comparison of Model Predicted Vertical Structure of Velocity with Analytic Solution for Wind Driven Flow (A_v = 10 cm²/s, τ_s = 0.1 N/m² (1 dyne/cm²), k = 0.05 cm/s) for: (a) Bottom Stress; and (b) No-Slip Bottom Boundary Condition (Model Results Are Presented for 5, 10, and 20 Vertical Levels)

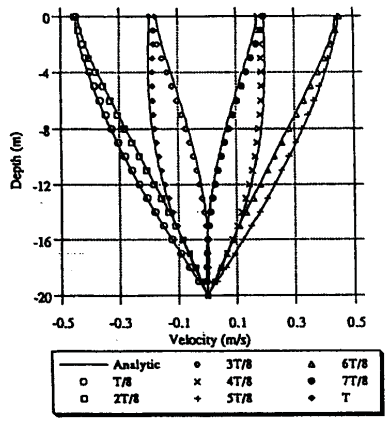

FIG. 3. Comparison of Model Predicted Velocity Structure with Analytic Solution for Tidally Driven Flow (Imposed Pressure Gradient of 0.058 N/m³) with Constant Vertical Viscosity, A_v = 0.011 m²/s at 1/8 Time Intervals Through One Tidal Cycle (Time Step, Δt = 279.45 s)

shown in Fig. 2(a). It can be seen that as the resolution increases the model predictions approach the analytic solution, especially near the bottom. The model represents the vertical velocity structure more accurately than for the density induced flow problem. The maximum errors are about 2% for five levels, 0.6% for 10 levels, and 0.2% for 20 levels. A similar problem, as in the density-induced flow, was found for the no-slip condition at the bottom and the boundary condition at the surface was modified to first order. The results are shown in Fig. 2(b). Again model prediction for this case is more accurate than in the baroclinic forcing problem.

Density Gradient Wind and River Forcing

The last test case considered flow driven by a combination of density gradient, wind, and river flow. The model was run using 20 levels. The results, not shown here, were simulated for bottom stress and no-slip bottom specifications, respectively. The agreement is excellent (<0.5%) for the bottom stress bottom boundary condition. The model underpredicts the velocity by about 5% in the mid-depth region for the no-slip bottom boundary condition.

Tidal Driven Flow

Two tests were employed to check the model's ability to simulate the vertical structure of tidal flow. The first test case is a point model in which the bottom boundary is specified using a no-slip condition, and the water slope is assumed known. The model was tested against constant and linearly varying vertical eddy viscosities. In the second test a bottom stress condition was employed at the sea bed. The bottom friction was linearized and related to the vertically averaged velocity.

Point Model Test

Constant Viscosity

The analytic solution for this problem was given in article 347 in Lamb (1945). The following data are used in model testing. The imposed pressure gradient was 0.058 N/m³; period T = 12.42 h; depth h = 20 m; vertical viscosity A_v = 0.011 m²/s; and time step Δt = 279.45 s (160 steps per cycle). The test was performed using 20 levels. The model was started with zero velocities. The water slope was applied gradually (linear ramp over 4 cycles) until a steady state was achieved. Comparison between the analytic solution and the model prediction is shown in Fig. 3. The agreement is excellent throughout the water column.

Viscosity Varying Linearly with Height

Two simulations were studied with viscosity; one increasing and one decreasing linearly from the sea bed to the sea surface. The analytic solution is presented in Prandle (1982). Simulations were performed using the same depth, grid size, period, time step, sea surface slope, and initial condition as the constant viscosity test case.

In the case of viscosity increasing linearly from the bottom (sea surface), the viscosity at the sea bed (surface) is set at A_v = 0.001 m²/s; and the viscosity at the sea surface (bed) A_v = 0.021 m²/s. The results of these simulations are in excellent agreement with the analytic solutions. The boundary layer in the linearly increasing case is (referenced from the sea bed) thinner than the constant viscosity case due to the lower viscosity near the bottom. The boundary layer for the linearly decreasing case is thicker than for the constant viscosity case and occupies the whole water column due to the fact that the vertical viscosity at the bottom is higher than in the two previous cases.

3D Testing

Lynch and Officer (1985) derived an analytic solution for the 3D flow driven by periodic forcing, with linearized bottom stress (ku_b, kv_b) and linked to the vertically averaged solution for an annular channel. The solutions were assembled from one-dimensional (1D) vertical diffusion and 2D vertically averaged solutions of the governing equations.

Consider the quarter-circle geometry with quadratically varying bathymetry $h = h_o r^2$. Note r refers to the radius of the annual channel. The sketch of geometry, bathymetry, and grid configuration are shown in Fig. 4. The viscosity is constant throughout the depth. The analytic solution, however, requires that $A_v/(\Omega h^2)$ and kh/A_v be constant, and hence A_v and k must

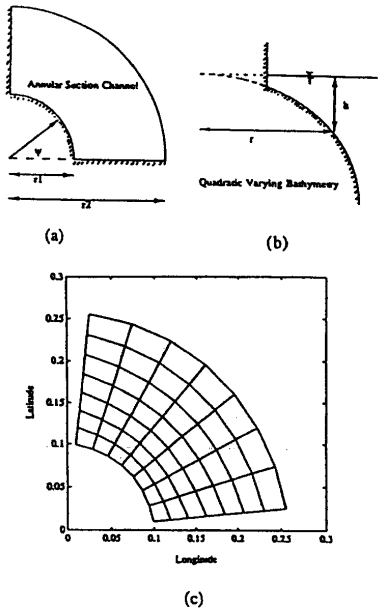

FIG. 4. Three-Dimensional Tidally Driven Model Test for: (a) Geometry; (b) Bathymetry; and (c) Grid Configuration [$r_1 = 9{,}950$ m; $r_2 = 31{,}250$ m; $h = 5\,(r/r_1)^2$]

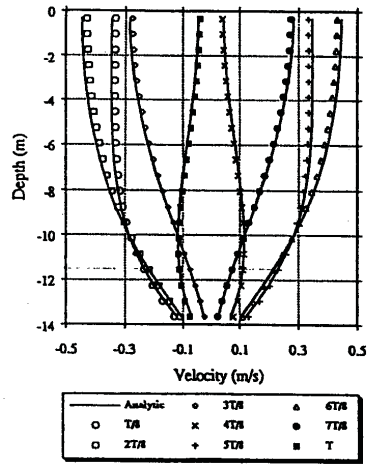

FIG. 5. Vertical Structure of Velocity at Increments of 1/8 of M_2 Tidal Period at $r = 16{,}660$ m and $\Psi = 39.4°$ for Three-Dimensional Model Test in Annular Section Channel, $r_1 = 9{,}950$ m; $r_2 = 31{,}250$ m; $A_v/(\Omega h^2) = 0.1$; $kh/A_v = 10$; $\Delta t = 558.9$ s

vary horizontally. Model tests were performed using a coarse, slightly nonorthogonal 7 × 7 grid system. The following parameters were used: inner radius $r_1 = 9{,}950$ m; outer radius $r_2 = 31{,}250$ m; $\Omega = 1.4 \times 10^{-4}$ s^{-1}; $kh/A_v = 10$; $A_v/(\Omega h^2) = 0.1$; and $h_o = 5/r_1^2$ m^{-1}. The open boundary was specified by varying the tidal amplitude $\zeta_o = 0.1 \cos(2\psi)$ m, where ψ = rotation angle. The model was run using eight and 20 levels in the vertical and time steps of 279.45, 558.9, and 1117.8 s.

Comparison of the model and analytical solution at point (5, 5) or at radius 16,660 m and $\psi = 39.375°$ for 20 levels with a time step of 558.9 s at one-eighth period increment is shown in Fig. 5. The agreement is very good. The largest errors (<10%) are near the surface area.

Sensitivity of the model predicted near surface currents (at *T*/8, *T*/4, 3*T*/8, *T*/2) to grid resolution and time step in the near surface region is shown in Table 1. The maximum errors occur at slack tide (at *T*/2). The model predicted errors decrease with decreasing time step. Model errors using eight vertical levels are approximately the same as those using 20 vertical levels.

A vector plot of the velocity field at the surface at *T*/4 (not presented) shows that the agreement between model predictions and analytic solution is excellent, even though the grid was relatively coarse and slightly nonorthogonal. The errors are less than 5%, except at the corner point of the inner radius $r = r_1$. Here they are about 10% due to the fact that the velocity is very small at this location. The errors become much smaller (<0.6%) at the outer radius near the open boundary. Comparison of the model-predicted velocity time series at a radius of 16,660 m, $\psi = 39.375°$, and for 0.35 m and 13.65 m below the sea surface with the analytic solution are shown in Fig. 6. The bottom velocity leads the surface velocity by 0.85 h. Predictions are again in excellent agreement with the analytic solution.

Turbulence Model Simulations

A simulation was performed in an open-closed, rectangular channel driven with tidal forcing, and a water depth of 10 m. The channel length is 51.34 km, and is represented by 20 horizontal grids. The tidal amplitude was 1.2 m, with a period of 12.42 h, $\gamma = 0.4$. A point 5.55 km from the open channel, where the pressure gradient has a magnitude that would give a current with amplitude 1.0 m/s in an inviscid calculation, was chosen to study the vertical structure of the velocity, eddy viscosity, and turbulent energy. The simulation assumed a ho-

TABLE 1. Model Prediction Errors (%) of Surface Velocity at $r = 16{,}660$ m and $\Psi = 39.4°$ for Annular Section Channel with Quadratic Bathymetry Using 8 and 20 Vertical Levels with Time Steps of 279.45, 558.9, and 1117.8 s

	8 Level			20 Level		
t (1)	279.45 s (CFL = 0.5) (2)	558.9 s (CFL = 1.0) (3)	1117.8 s (CFL = 2.0) (4)	279.45 s (CFL = 3.1) (5)	558.9 s (CFL = 6.2) (6)	1117.8 s (CFL = 12.4) (7)
T/8	4.1	4.2	4.8	3.9	4.0	4.6
T/4	3.7	3.7	4.0	3.5	3.5	3.9
3*T*/8	3.1	3.0	3.0	3.1	3.0	3.0
T/2	8.7	10.0	12.6	7.6	8.8	11.6

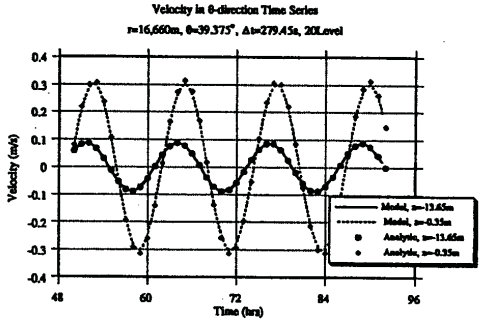

FIG. 6. Comparison of Model Predicted Velocity Time Series with Analytical Solution at $r = 16{,}660$ m and $\Psi = 39.4°$ for Three-Dimensional Model Test in Annular Section Channel Driven by M_2 Tide at Open Boundary with Varying Amplitude of $\zeta_o = 0.1 \cos(2\psi)$ m; $r_1 = 9{,}950$ m; $r_2 = 31{,}250$ m; $A_v/(\Omega h^2) = 0.1$; $kh/A_v = 10$; $\Delta t = 279.45$ s; and 20 Vertical Levels

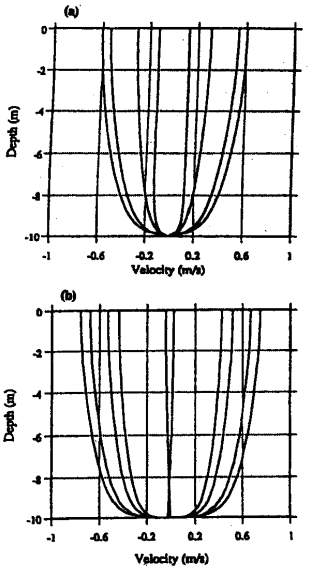

FIG. 7. Comparison of (a) Model Predicted Vertical Structure of Velocity with (b) Numerical Simulations of Davies and Jones (1990) for One-Dimensional Turbulence Model Test Driven by M_2 Tide with Imposed Pressure Gradient of 0.14 N/m³; No-Slip Bottom Boundary Condition; $\gamma = 0.4$; $\Delta t = 558.9$ s; and 40 Vertical Levels

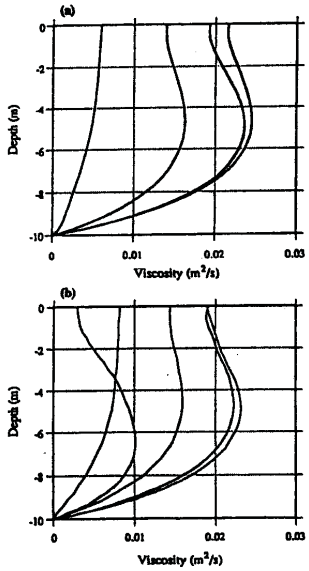

FIG. 8. Comparison of (a) Model Predicted Vertical Structure of Viscosity with (b) Numerical Simulations of Davies and Jones (1990) for One-Dimensional Turbulence Model Test Driven by M_2 Tide with Imposed Pressure Gradient of 0.14 N/m³; No-Slip Bottom Boundary Condition; $\gamma = 0.4$; $\Delta t = 558.9$ s; and 40 Vertical Levels

mogeneous fluid. The Coriolis, baroclinic, and advective terms were neglected to compare the present results with the circulation and turbulence model developed by Davies and Jones (1990).

For a no-slip condition at the bottom boundary, simulations were conducted using 40 levels with a time step of 558.9 s. A comparison between the results of the present model (40 levels) and Davies and Jones' (1990) with 100 levels and a logarithmic transformation is shown in Figs. 7–10. Results are given at one-eighth intervals during the tidal cycle. The maximum surface velocity of the present model is about 20%

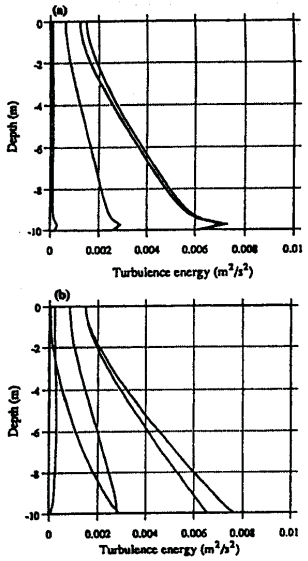

FIG. 9. Comparison of (a) Model Predicted Vertical Structure of Turbulence Energy with (b) Numerical Simulations of Davies and Jones (1990) for One-Dimensional Turbulence Model Test Driven by M_2 Tide with Imposed Pressure Gradient of 0.14 N/m³; No-Slip Bottom Boundary Condition; $\gamma = 0.4$; $\Delta t = 558.9$ s; and 40 Vertical Levels

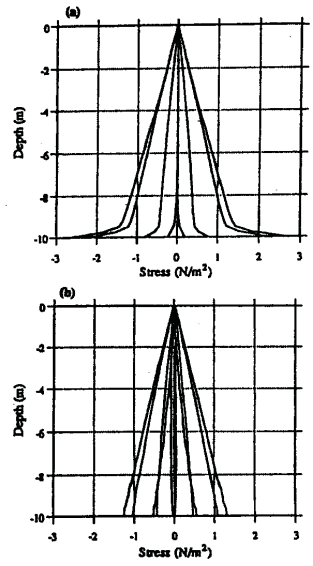

FIG. 10. Comparison of (a) Model Predicted Vertical Structure of Shear Stress with (b) Numerical Simulations of Davies and Jones (1990) for One-Dimensional Turbulence Model Test Driven by M_2 Tide with Imposed Pressure Gradient of 0.14 N/m³; No-Slip Bottom Boundary Condition; $\gamma = 0.4$; $\Delta t = 558.9$ s; and 40 Vertical Levels

lower than their results. The structure of the eddy viscosity, turbulent energy, and shear stress are similar. However, the bottom shear stresses are twice as high in Davies and Jones (1990) than in the present simulation because the present grid structure does not provide sufficient resolution in the near-bed region. This problem is more severe at low grid resolution.

For the bottom stress specification, simulations were performed using 10 and 40 levels with a time step of 279.45 s. In these simulations the bottom drag coefficient was set at 0.0025, and $\gamma = 0.4$. A comparison between simulations using high (40 levels) and low vertical resolution (10 level) is shown in Fig. 11 for the velocity profile. The maximum viscosity, shear stress, and energy (not shown) computed using the low resolution grid are approximately 25% higher than simulations using the high resolution grid. The velocity structure (Fig. 11), however, is not significantly affected. Further tests showed that a stable and accurate velocity prediction can be obtained using

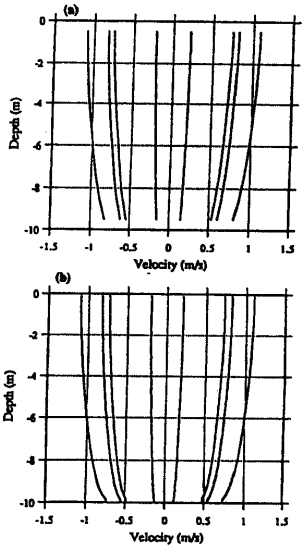

FIG. 11. Comparison of Model Predicted Vertical Structure of Velocity Using (a) 10 and (b) 40 Vertical Levels at Location 5.55 km from Open Boundary for Turbulence Model Test Driven by M_2 Tide; Bottom Stress Condition; $\gamma = 0.4$; $C_b = 0.0025$; $\Delta t = 558.9$ s

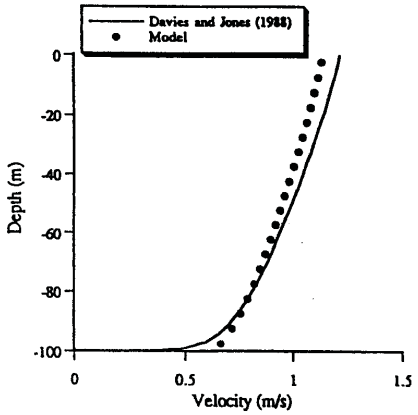

FIG. 12. Comparison of Model (Bottom Stress Condition) Predicted Vertical Structure of Velocity with Numerical Simulations of Davies and Jones (1988) Driven by Wind Stress; $\tau_s = 1.0$ N/m^2; $C_b = 0.0025$; and $\gamma = 0.2$

a time step of 1117.8 s (550 CFL, based on the diffusive time scale for 40 levels).

The model was also tested against steady wind-induced flow with a depth of 100 m, a wind stress of 1 N/m^2, a bottom stress specification; 20 levels, with a friction coefficient of, $C_b = 0.0025$, and $\gamma = 0.2$. A comparison of the velocity computed using the present model and similar results by Davies and Jones (1988) with 100 levels and a logarithmic transformation is presented in Fig. 12. The agreement is very good. A maximum difference of 5% is predicted near the surface and the sea bed. The model-predicted vertical structure of viscosity gives excellent agreement at middepth and near the surface, but slightly overpredicts at the bottom. The turbulent energy simulated by the present model is higher than Davies and Jones' (1988) model both at the surface and bottom. Differences that occur near the bottom are due to differences in the bottom boundary condition specification. The present simulations employ a bottom stress condition where the turbulent energy at the sea bed is specified while Davies and Jones (1988) use a no-slip bottom condition and specify no energy flux at the sea bed. In general the agreement is excellent although the present work uses relatively low grid resolution compared to Davies and Jones (1988).

Salinity Intrusion Simulations

Ippen and Harleman (1961) derived an analytical solution for salinity intrusion under the assumption that the salinity distribution can be represented by the equilibrium of the 1D convective-diffusion processes where the time and cross-sectionally averaged fresh water (seaward) flux of salt is balanced by the horizontal diffusive flux of salt (landward). The effect of gravitational convection by density differences (density included) is neglected. Consider a rectangular channel with a length of 105.5 km, a river flow velocity of 0.000714 m/s, and horizontal diffusion coefficients of 4, 6, 8, and 10 m^2/s. The advective term in the salt transport equation is solved by the Lax-Wendroff method. The open boundary is specified by a constant salinity of 30 ppt. Comparison between model predictions and the analytic solution for various values of the horizontal diffusion coefficient D_h is shown in Fig. 13. The agreement between the model and analytical solution is excellent.

Finally the model was used to predict the salinity intrusion in Rotterdam Waterway using identical conditions to those employed by Smith and Takhar (1981). The simulation was intended to evaluate the ability of the model to predict salinity intrusion. The waterway was represented by a rectangular channel with a length of 99 km. The width and depth were

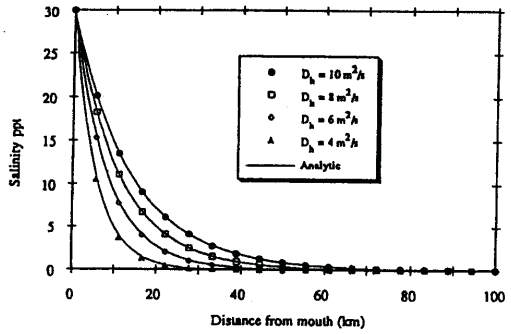

FIG. 13. Comparison of Model Predicted Salinity Distribution with Analytic Solution for One-Dimensional Salinity Intrusion Test (Transport Equation is Solved by Lax-Wendroff Method; River Flow Velocity is 0.000714 m/s; and Horizontal Diffusion Coefficients of 4, 6, 8, and 10 m^2/s Are Used)

kept constant with values of 400 and 13 m, respectively. The river inflow was 1,000 m^3/s. The model was run using 40 grids along the channel and 20 levels in the vertical. The initial conditions for velocity, elevation, and salinity were set to zero. Along the open boundary (mouth) the salinity distribution is assumed to vary from 30 ppt at the bottom to 20 ppt at the surface on inflow. The model was run with an M_2 tide. The time step was 558.9 s with a tidal amplitude at the open boundary of 0.9 m. The advective term in the salt transport equation was solved using the upwind method. The Lax-Wendroff method was not used because it required a large horizontal diffusivity (~5000 m^2/s) to maintain stability. The model was run for 66 d to achieve steady state.

A simulation was performed in which the vertical viscosity and diffusivity were calculated by the turbulence model. The bottom friction, C_b, was 0.0010. It was found that the model was very sensitive to the value of γ in the mixing length specification. Since the turbulent energy source is from the bottom boundary, the bottom drag coefficient, C_b, is also important in determining the vertical velocity structure. Fig. 14 shows the salinity distribution along the channel for $C_b = 0.0005$ and $\gamma = 0.03$ with the empirical formulation of (30), which was taken from Officer (1976), implemented to represent stratification effects. Smith and Takhar's (1981) model predictions and field observations are also shown [Fig. 14(a)]. The results show that the model-predicted high tide salinity distribution is in reasonable agreement with and an improvement over Smith and Takhar's results. Both the present and Smith and Takhar (1981) models do not accurately predict the low tide salinity distribution. As analyzed by Smith and Takhar (1981), the poor model performance for the low water salinity distribution is caused by the dock system in the waterway acting as a source and sink of salt on the ebb and flood tide, respectively.

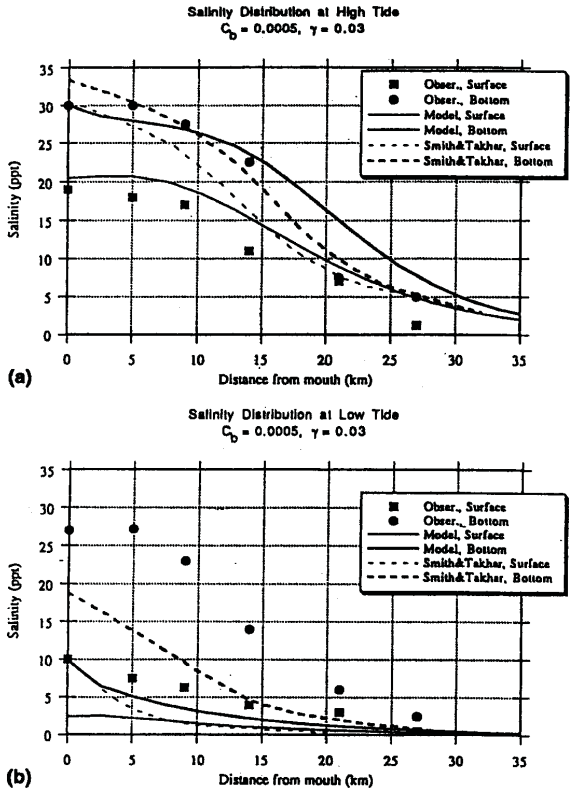

FIG. 14. Comparison of Model Predicted Salinity Distribution along Channel with Observations and Numerical Simulation of Smith and Takhar (1981) for Rotterdam Waterway at: (a) High Tide; and (b) Low Tide (Vertical Viscosity and Diffusivity Are Obtained from Turbulence Model Using Bottom Friction; C_b = 0.0005; and γ = 0.3)

CONCLUSION

A detailed description of the 3D boundary-fitted circulation model in spherical coordinates for coastal waters is presented. Both the dependent and independent horizontal variables are transformed to a boundary-fitted coordinate system. The equations are also transformed to σ-coordinates to resolve the variation in bathymetry. Both the exterior and interior mode are solved using the same time step. The numerical scheme is second order in time and space. The time step is not restricted by the shallow water gravity wave and vertical diffusion CFL criteria. The eddy viscosity/diffusivity can be specified or obtained from a one equation turbulence energy model.

A series of model tests to linear problems shows that the present model is fully capable of predicting the vertical structure of the flow in response to tidal, wind, river, and density forcing. The 3D model test in an annular section channel with quadratic bathymetry under tidal forcing has shown the model's ability to resolve a more complicated geometry and bathymetry.

The model, with a bottom stress condition, gives good predictions of the vertical structure of the velocity, shear stress, turbulence energy, and eddy viscosity even at modest vertical grid resolutions. No iteration or filtering is employed. The no-slip bottom boundary condition version of the present model fails to accurately predict the shear stress and energy distributions at the sea bed for 40 vertical levels because of the lack of vertical resolution near the sea bed.

Agreement between the model and analytic solution is excellent for the 1D salinity intrusion problem where the density gradient induced flow is neglected. The model accurately predicted the salinity distribution at high tide in the Rotterdam Waterway where the viscosity/diffusivity were obtained from a turbulence model. The poor results at low tide were probably caused by the lack of consideration of the effect of the dock system on the salinity field (Smith and Takhar 1981).

The CPU time of the internal mode with turbulence model for each water cell per computational step is 3.1×10^{-6} min on a 486/50 MHz personal computer system using a Lahey F7732 Version 5.1 Fortran compiler. The CPU time of the external mode is 2.9×10^{-6} min using the same machine and compiler.

APPENDIX I. REFERENCES

Abraham, G. (1988). "Turbulence and mixing in stratified tidal flows." *Physical processes in estuaries*, P. Dronkers and R. Leussen, eds., Springer-Verlag KG, Berlin, Germany.

ASCE Task Committee on Turbulence Models in Hydraulic Computations. (1988). "Turbulence modeling of surface water flow and transport: Part I." *J. Hydr. Engrg.*, ASCE, 114(9), 970–991.

Blackadar, A. K. (1962). "The vertical distribution of wind and turbulent exchange in a neutral atmosphere." *J. Geophys. Res.*, 67, 3095–3120.

Celik, I., and Rodi, W. (1985). "Calculation of wave-induced turbulent flows in estuaries." *Oc. Engrg.*, 12(6), 531–542.

Cheng, R. T., and Smith, P. E. (1990). "A survey of three-dimensional numerical estuarine models." *Estuarine and coastal modeling*, M. L. Spaulding, ed., ASCE, New York, N.Y., 1–15.

Davies, A. M., and Jones, J. E. (1988). "Modelling turbulence in shallow sea regions." *Small-scale turbulence and mixing in the ocean, Proc., 19 Liege Colloquium on Oc. Hydrodyn.*, J. C. Nihoul and B. M. Jamart, eds., Univ. of Liege, Liege, Belgium.

Davies, A. M., and Jones, J. E. (1990). "On the numerical solution of the turbulence energy equations for wave and tidal flows." *Int. J. for Numer. Meth. in Fluids*, 11, 1–25.

Fletcher, C. A. J. (1988). *Computational techniques for fluid dynamics, volume I, fundamental and general techniques.* Springer-Verlag New York, Inc., New York, N.Y.
Ippen, A. T., and Harleman, D. R. F. (1961). "One-dimensional analysis of salinity intrusion in estuaries." *Tech. Bull. No. 5*, Com. on Tidal Hydr., U.S. Army Corps of Engrs., Fort Belvoir, Va.
Johnson, B. H. (1980). "VAHM-A vertically averaged hydrodynamic model using boundary-fitted coordinates." *MP HL-80-3*, U.S. Army Corps of Engrs. Wtrwy. Experiment Station, Vicksburg, Miss.
Lamb, H. (1945). *Hydrodynamics.* Dover Publications, Inc., New York, N.Y.
Lynch, D. R., and Gray, W. G. (1978). "Analytic solutions for computer flow model testing." *J. Hydr. Div.*, ASCE, 104(00), 1409–1428.
Lynch, D. R., and Officer, C. B. (1985). "Analytic solutions for three-dimensional hydrodynamic model testing." *Int. J. for Numer. Meth. in Fluids*, 5, 529–543.
Lynch, D. R., and Werner, F. E. (1987). "Three-dimensional hydrodynamics on finite-element. Part I: Linearized harmonic model." *Int. J. for Numer. Meth. in Fluids*, 7, 871–909.
Mofjeld, H. O., and Lavelle, J. W. (1984). "Setting the length scale in a second-order closure model of the unstratified bottom boundary layer." *J. Phys. Oceanography*, 14, 833–839.
Muin, M. (1993). "A three-dimensional boundary-fitted circulation model in spherical coordinates," PhD dissertation, Univ. of Rhode Island, Narragansett Bay Campus, Narragansett, R.I.
Muin, M., and Spaulding, M. L. (1996). "Two-dimensional boundary-fitted circulation model in spherical coordinates." *J. Hydr. Engrg.*, ASCE, 122(9), 512–521.
Munk, W. H., and Anderson, E. R. (1948). "Notes on theory of thermocline." *J. Marine Res.*, 7, 276.
Officer, C. B. (1976). *Physical oceanography of estuaries.* John Wiley & Sons, Inc., New York, N.Y., 120.
Prandle, D. (1982). "The vertical structure of tidal currents." *Geophys. Astrophys. Fluid Dyn.*, 22, 29–49.
Sheng, Y. P. (1986). "A three-dimensional mathematical model of coastal, estuarine and lake currents using boundary-fitted grid." *Tech. Rep. No. 585*, Aeronautical Research Associates of Princeton, Princeton, N.J.
Smith, T. J., and Takhar, H. S. (1981). "A mathematical model for partially mixed estuaries using the turbulence energy equation." *Estuarine, Coast., and Shelf Sci.*, 13, 27–45.
Spaulding, M. L. (1984). "A vertically averaged circulation model using boundary-fitted coordinates." *J. Phys. Oceanography*, 14, 973–982.
Swanson, J. C. (1986). "A three-dimensional numerical model system of coastal circulation and water quality," PhD dissertation, Univ. of Rhode Island, Kingston, R.I.

APPENDIX II. NOTATION

The following symbols are used in this paper:

A_v = vertical eddy viscosity;
a = tidal wave amplitude;
b = turbulence kinetic energy;
C_μ = empirical constant in eddy viscosity relationship;
C_a = drag coefficient at surface;
C_b = drag coefficient at bottom;
C_d = empirical constant in energy dissipation relationship;
D = elevation + water depth;
D_h = horizontal eddy diffusivity;
D_v = vertical eddy diffusivity;
g = gravitation;
h = water depth;
J = Jacobian of curvilinear coordinate;
K = Von Karman constant;
k = linearized bottom friction;
L = wave length;
L_m = mixing length;
l = length of channel;
n = node number;
p = pressure;
q = concentration of substance;
R = radius of earth;
R_i = Richardson number;
S = salinity;
T = wave period;
t = time;
u_o = river flow;
U_{*_s} = friction velocity due to wind stress;
U_{*_b} = friction velocity due to bottom stress;
U, V = vertically averaged velocity in ϕ and θ direction;
U^c, V^c = vertically averaged velocity in curvilinear coordinate;
u, v, w = water velocity in ϕ, θ, r direction;
u^c, v^c = water velocity in curvilinear coordinate;
u_b = bottom velocity in ϕ direction;
v_b = bottom velocity in θ direction;
W_ϕ = wind speed in ϕ direction;
W_θ = wind speed in θ direction;
β = volumetric expansion coefficient;
γ = constant parameter in mixing length formulation;
ε = dissipation rate of energy;
ζ = water elevation;
ζ_o = water elevation amplitude at open boundary;
Θ = temperature °C;
ι = water surface slope;
κ = wave number;
Λ = horizontal density gradient;
ξ, η = generalized curvilinear coordinate system;
ρ = water density;
ρ_a = air density;
ρ_o = water density average;
$\bar{\rho}$ = vertically averaged of water density;
ρ' = vertically density difference;
σ = vertical coordinate transformation;
σ_b = empirical diffusion constant;
σ_t = Schmidt number;
τ_b = bottom shear stress;
τ_s = wind shear stress;
Φ = mean scalar quantity;
ϕ, θ, r = spherical coordinate system;
Ω = wave frequency; and
ω = vertical velocity in σ transform coordinate.

Appendix B: Development of an Estuarine Thermal Environmental Model in a Boundary Fitted, Curvilinear Coordinate System (Mendelsohn, 1998)

Development of an Estuarine Thermal Environmental Model in a Boundary-Fitted, Curvilinear Coordinate System

Daniel L. Mendelsohn
Applied Science Associates, Inc.
Narragansett, Rhode Island 02882

INTRODUCTION

With the deregulation of the power industries in the United States there has been a rekindled interest in the development of new power generation station and the re-permitting of existing older or dormant stations. In the last two decades however increased public awareness of the possible adverse environmental effects of using 'once through cooling' in natural water bodies has lead to substantial pressure on regulators as well as the utilities to study, understand and mitigate against potential degradation. Once through cooling involves the intake of water from a natural water body, (e.g. river, lake, estuary), the use of that water to cool process water, (e.g. to condense steam) and the subsequent expulsion of the now warmer water back into the environment. The incentives for this form of cooling are both efficiency and economics.

The two most prevalent and more important concerns associated with once through cooling are: 1) the potential an unacceptable increase in temperatures in the power station effluent receiving waters; 2) the possibility that increased surface water temperatures will enhance thermal stratification of the water column resulting in a reduction of hypolimnetic reaeration. Increased temperature and reduced oxygen are both considered degredation of habitat and can cause avoidance and increased mortality to indigenous marine floral and faunal populations. For the case of an existing facility, when measurements of temperature and dissolved oxygen are made in the environment, the question is, to what extent are those measurements influenced by the thermal effluent? These are difficult concerns to address in both the scientific and the regulatory realms. Increasingly, parties involved in the decision making process have come to rely on computer modeling to address the physical, chemical and, occasionally, biological aspects of a problem, allowing regulatory and engineering decisions to be made on a solid scientific basis.

Recent improvements in computing power and observational data retrieval, storage and dissemination have made possible the development and application of a new generation of hydro-thermal models capable of addressing the concerns listed above.

THERMAL MODEL DEVELOPMENT

The development of the temperature model follows the formulation of the coupled, three-dimensional, boundary-fitted, general curvilinear coordinate, hydrodynamic and salinity transport model system for which it is to become a component. For a detailed description of the hydrodynamic model system development and testing the interested reader is referred to Muin and Spaulding, 1997 a; Mendelsohn et al. 1995 and Muin, 1993. Additional model applications can be found in Muin and Spaulding, 1997 b; Huang and Spaulding, 1995a,b; Swanson and Mendelsohn, 1996, 1993; Peene et.al. 1998.

The temperature model is designed to be integrated into and coupled with the hydrodynamic model system and use the transformed currents directly. The temperature equation must therefore be transformed as well.

Conservation of Temperature

Starting with the differential form of the conservation of energy equation, the three-dimensional conservation of temperature equation in spherical polar coordinates can be written as follows:

$$\frac{\partial T}{\partial t}+\frac{u}{r\cos\theta}\frac{\partial T}{\partial \phi}+\text{voverr}\frac{\partial T}{\partial \theta}+w\frac{\partial T}{\partial r}=\frac{Q_s}{\rho C_p V}+\frac{q_{env}}{\rho C_p \delta r}+\frac{\partial}{\partial r}\left(A_v\right)+\frac{A_h}{r^2}\left[\frac{\partial^2 T}{\cos^2\theta\partial\phi^2}+\frac{\partial^2 T}{\partial\theta^2}\right] \quad (1)$$

where,

T = temperature, (^oC)
t = time, (s)
u = east, φ, velocity vector component, (m/s)
v = north, θ, velocity vector component, (m/s)
w = vertical, r, velocity vector component, (m/s)
A_v = vertical eddy diffusivity, (m^2/s)

A_h = horizontal eddy diffusivity, (m^2/s)
Q_s = system heat sources and sinks, (W)
q_{env} = net surface heat exchange with the environment, (W/m^2)
ρ = water density, (kg/m^3)
C_p = specific heat of water, (J/kg ^oC)
V = volume, (m^3)

The horizontal velocities and independent variables are next transformed to a general curvilinear coordinate system in the horizontal and at the same time the well known sigma transform, (Phillips, 1956) is applied in the vertical. The equations for the conservation of substance in a curvilinear coordinate system (ξ, η) in terms of the contravariant velocity components are as follows:

$$\frac{\partial T}{\partial t} + \frac{u^c}{r\cos\theta}\frac{\partial T}{\partial \xi} + \frac{v^c}{r}\frac{\partial T}{\partial \eta} = \frac{Q_s}{\rho\, Csubp V} + \frac{2\, q_{env}}{\rho\, C_p\, D\, \delta\sigma} + \frac{4}{D^2}\frac{\partial}{\partial\sigma}\left(A_v\frac{\partial T}{\partial\sigma}\right) + \tag{2}$$

$$\frac{A_h}{r^2 J^2}\left[\left(\frac{\theta_\eta\theta_\eta}{\cos^2\theta} + \phi_\eta\phi_\eta\right)\frac{\partial^2 T}{\partial\xi^2} - 2\left(\frac{\theta_\xi\theta_\eta}{\cos^2\theta} + \phi_\xi\phi_\xi\right)\frac{\partial^2 T}{\partial\xi\partial\eta} + \left(\frac{\theta_\xi\theta_\xi}{\cos^2\theta} + \phi\xi\phi\xi\right)\frac{\partial^2 T}{\partial\eta^2}\right]$$

where,
u^c = contravariant velocity component in the ξ direction
v^c = contravariant velocity component in the η direction
σ = transformed vertical coordinate
ζ = water surface elevation, (m)
D = total depth = ζ+ local depth, (m)
J = the Jacobian = $\varphi_\xi\varphi_\eta - \varphi_\eta\theta_\xi$

The relationship between the contravariant transformed velocities (u^c, v^c) and physical velocities in spherical coordinates (u,v) is given by

$$u = \cos\theta\,\phi_\xi\, u^c + \cos\theta\,\phi_\eta\, v^2$$
$$v = \theta_\xi\, u^c + \theta_\eta\, v^c \tag{3}$$

The temperature transport model (Eq. 2) is solved by a simple explicit technique except for the vertical diffusion term which is solved by a three time level, implicit scheme to ease the time step restriction due to the small vertical length scale. The advection terms are solved using either an upwind-differencing scheme which introduces minor numerical (artificial) diffusivities and is

first order accurate or the second order accurate QUICKEST formulation. Experimentation found that although the QUICKEST scheme was for the most part more conservative it was also less stable, requiring a smaller time step and consequently longer run-times than when using the 1st order upwind scheme. Horizontal gradients in temperature, (as well as in salinity, density and pressure) are evaluated along lines of constant depth to reduce the artificial numerical dispersion in the vertical associated with the sigma transform system.

The horizontal diffusion terms are solved by a centered-in-space, explicit technique. The diffusive and advective stability criteria for the numerical techniques are, $\Delta t<\Delta s^2/(2D_h)$, and $\Delta t<\Delta s/U_s$, where Δs and U_s are horizontal grid size and velocity, respectively.

Bottom Boundary Condition

The water bottom boundary condition is specified to assume that the water and bottom material are in thermal equilibrium, therefore there is no heat transfer between the water in the bottom layer and the bottom boundary. This may be written as:

$$\frac{\partial T_b}{\partial \sigma} = 0 \tag{4}$$

Surface Boundary Condition

At the water surface the temperature is influenced by a number of factors in the environment above. The most important terms in the heat transfer with the environmental can be summarized as follows:

- shortwave solar radiation
- longwave atmospheric radiation
- longwave radiation emitted from the water surface
- convection, (sensible) heat transfer between water and air
- evaporation, (latent) heat transfer between water and air

The net rate of heat transfer with the environment, q_{env} in Eq(2), including the primary forcing factors listed above can be written as:

$$q_{env} = q_{sw} - q_{sw\,r} + q_{lw} - q_{lw\,r} - q_{lw\,b} + q_c + q_e \tag{5}$$

where,

q_{sw} = solar short wave radiation, (W/m^2)

q_{swr} = reflected solar short wave radiation, (W/m^2)
q_{lw} = atmospheric long wave radiation, (W/m^2)
q_{lwr} = reflected atmospheric long wave radiation, (W/m^2)
$q_{lw\,b}$ = long wave, (back) radiation, emitted by the water surface, (W/m^2)
q_c = convection, (sensible) heat transfer, (W/m^2)
q_e = evaporation, (latent) heat transfer, (W/m^2)

Each of the terms in the surface heat balance is described below.

Solar shortwave radiation

The solar short wave radiation is often an available, measured quantity, in which case it can be entered directly into the model as data. It can often be obtained from local airport records or from radiation model analyses for example, (DeGaetano et. al., 1993). Local measured radiation data is valued in that it contains information on both the solar radiation and the cloud cover and its influence, and is the actual radiation hitting the water surface at that date and time.

In the absence of data, solar radiation can be predicted following the method as presented by Duffie and Beckman, (1980). Starting with the clear sky radiation, G_{ctot}:

$$G_{ctot} = G_{cb} + G_{cd} \quad (6)$$

where

$$G_{cb} = G_{on}\,\tau_b \cos\theta_z \quad \text{= clear sky beam radiation} \quad (7)$$

$$G_{cd} = G_{on}\,\tau_d \cos\theta_z \quad \text{= clear sky diffuse radiation} \quad (8)$$

and the extraterrestrial, normal radiation, G_{on} is defined as

$$G_{on} = G_{sc}\,[1 + 0.33 \cos(360n / 365)] \quad (9)$$

where

G_{sc} = 1353 (W/m^2) = solar constant

The beam and diffuse atmospheric transmittance coefficients, τ_b and τ_d, respectively, can be defined as:

$$\tau_b = a_0 + a_1 e^{-k / \cos\theta z} \quad (10)$$

where

$a_0 = r_0\, a^*_0$, $a^*_0 = 0.4237 - 0.00821\,(6 - A)^2$
$a_1 = r_1\, a^*_1$, $a^*_1 = 0.5055 - 0.00595\,(6.5 - A)^2$
$k = r_k\, k^*$, $k^* = 0.2711 - 0.01858\,(2.5 - A)^2$

and

$r_0 = 0.97$
$r_1 = 0.99$
$r_k = 1.02$
A = altitude, (km)

and the diffuse transmittance is,

$$\tau_d = 0.2710 - 0.2939\ \tau_b \quad (11)$$

The zenith angle, $\cos \theta_z$ is defined as:

$$\cos \theta_z = \cos \delta \cos \varphi \cos \omega + \sin \delta \sin \varphi \quad (12)$$

where,

φ = lattitude, (deg)
δ = declination of the sun, (deg) = $23.45 \sin [360 (284 + n) / 365]$
n = day of the year
ω = hour angle, (deg)

Finally, the hour angle, ω is calculated from the local longitude and solar time as:

$$\omega = (t_s - 12)\ 15\ ^{o}/hr$$

where,

t_s = solar time = standard time + $4 (L_{st} - L_{loc}) + E$
L_{st} = standard meridian, (deg) (e.g. 75^{o} W for Rhode Island)
L_{loc} = local longitude, (deg)

and E is the equation of time defined by:

$$E = 9.87 \sin 2B - 7.53 \cos B - 1.5\ B$$

where,

$B = [\ 360 (n - 81) / 364\ ]$

The total clear sky radiation, G_{ctot} can then be corrected for cloud cover effects with the use of a clearness index, K_T. This value can be defined on an monthly, daily or hourly basis dependent on available data and use and is often available with meteorological data when measured radiation data is not. The clearness index is the ratio of the average radiation on an horizontal surface to the average extraterrestrial radiation at the same latitude and longitude;

$$K_t = \frac{\overline{G}}{G_{on}} \tag{13}$$

The value $\overline{G}$ would then be used in place of G_{on} in equations (7) and (8) to create G_{tot}.

Finally, the net solar shortwave radiation, q_{net} , absorbed through the water surface, can be calculated as;

$$q_{net} = q_{sw} - q_{swr} = \alpha_w (1 - albedo_w) G_{tot} \tag{14}$$

where,

α_w = water absorptivity, (-) $\cong 0.97$
$albedo_w$ = albedo of the water surface (-), (see below)

Reflected solar short wave radiation

The reflected solar short wave radiation, as included in Equation (14), and can defined as;

$$q_{swr} = albedo_w G_{tot} \tag{15}$$

where the albedo is a measure of the reflective property of the material surface, (water in this case) and can be defined as:

$albedo_w$ = reflected energy / incident energy

Values for the albedo for water are both a function of wave state and strongly of solar altitude, Stull, (1988). They can range from 0.03 when the sun is overhead to near 1.0 at low elevation angles. Stull, (1988) gives an equation for calculating the albedo for varying solar altitudes, (azimuth angle):

$$albedo_w = -0.0139 + 0.0467 \tan\theta_z \tag{16}$$

Atmospheric long wave radiation

In addition to the short wave radiation, the atmosphere and the water surface are also exchanging long wave radiation. The atmospheric long wave radiation is a function of the air temperature and water vapor content and may be calculated from an effective sky temperature, (Duffie & Bechman, 1980). From the Stephan-Bolzmann law long wave radiation to the water surface is

then:

$$q_{lw} = \sigma_{sb} T_{sky}^{4} \quad (17)$$

where,

σ_{sb} = Stephan-Bolzmann constant, (5.669×10^{-8} W / m^2 K^4)
T_{sky} = effective sky temperature, (K)

Duffie and Beckman suggest that the sky temperature be calculated from an empirical relationship, (Bliss, 1961) as:

$$T_{sky} = [0.8 + \frac{(T_{dp} - 273)}{250}]^{\frac{1}{4}} \quad (18)$$

where

T_{dp} = dew point temperature, (C).

Thomann and Mueller suggest an alternate formulation:

$$q_{lw} = \sigma_{sb} T_{ak}^{4} (A + 0.031\sqrt{e_a}) \quad (19)$$

where

T_{ak} = air temperature, (K)
e_a = vapor pressure at air temperature, T_a (mm Hg)
= (relative humidity fraction) x (e_{sat} @ T_a)
e_{sat} = saturation vapor pressure (mm Hg)
T_a = air temperature, (C)
A = coefficient to account for air temperature and clearness index, with a range of 0.5 - 0.7.

The saturation vapor pressure can be calculated from the air temperature (T_a) using the following equation, (List, 1951):

$$e_{sat} = 4.58123 \times 10^{[7.5 T_a / T_{ak}]} \quad (20)$$

Results for the two long wave radiation formulations only vary slightly for a given set of conditions with Equation (19) consistently giving a larger value, by approximately 3%, than (17). No independent confirmation for either formulation has been given to date.

Reflected atmospheric long wave radiation

The reflected long wave radiation over a water body is generally small, about 3% of the incoming long wave, (Thomann & Mueller, 1987) and can be calculated as:

$$q_{lwr} = (1 - \varepsilon_w) q_{lw} \quad (21)$$

where

ε_w = emissivity of water $\cong$ 0.97

Long wave radiation, emitted by the water surface

The water surface also emits long wave radiation at a rate proportional to the surface temperature in Kelvins:

$$q_{lw} = \varepsilon_w \sigma_{sb} T_{wk}^4 \quad (22)$$

where

T_{wk} = water surface temperature, (K)

Convection heat transfer

The rate of convective heat transfer between the water surface and the air depends on the temperature difference between the two and is suggested to be proportional to the square of the wind speed, (Thomann and Mueller, 1987; Edinger et. al. 1974). This can be written as,

$$q_c = c_1 (19.0 + 0.95 U_w^2) (T_a - T_w) \quad (23)$$

where

T_w = water surface temperature, (C)

c_1 = Bowen's coefficient = 0.47 mm Hg / ^oC

Evaporation heat transfer

Similar to the rate of convective heat transfer the evaporative heat transfer between the water and the air can be thought of as depending on the difference between the vapor pressures of the two and is also suggested to be proportional to the square of the wind speed, (Thomann and Mueller, 1987; Edinger et. al. 1974). This can be written as,

$$q_c = (19.0 + 0.95 U_w^2) (e_a - e_w) \quad (24)$$

where

e_w = vapor pressure at water surface temperature, T_w (mm Hg)

REFERENCES

DeGaetano, Arthur T., Keith L. Eggleston and Warren W. Knapp, 1993. Daily Solar Radiation Estimates for the Northeast United States. Northeast Regional Climate Center Research Series, Publication No. RR93-4, May 1993.

Duffie, John A. and William Beckamn, 1980. Solar Engineering of Thermal Processes. John Wiley and Sons, New York.

Edinger, J.E., D.K.Brady and J.C. Geyer, 1974. Heat Exchange and Transport in the Environment. Report No. 14, Electric Power Res. Inst. Pub. No. EA-74-049-00-3, Palo Alto, Ca, Nov. 1974, 125pp.

Huang, W. and M.L. Spaulding, 1995a. Modeling of CSO-induced pollutant transport in Mt. Hope Bay. ASCE J. of Environmental Engineering, Vol. 121, No. 7, July, 1995, 492-498.

Huang, W. and M.L. Spaulding, 1995b. A three dimensional numerical model of estuarine circulation and water quality induced by surface discharges. ASCE Journal of Hydraulic Engineering, 121:(4) April 1995, p. 300-311.

List, R.J. 1951/1984. Smithsonian Meteorological Tables. Smithsonian Institution Press, Washington DC.

Mendelsohn, D.L., E. Howlett and J.C. Swanson, 1995. WQMAP in a Windows Environment. published in proceedings of: 4th International Conference on Estuarine and Coastal Modeling, ASCE, San Diego, October 26-28, 1995.

Muin, M. and M.L. Spaulding, 1997a. A 3-D boundary-fitted circulation model. Journal of Hydraulic Engineering, Vol. 123, No. 1.

Muin, M., M.L. Spaulding, 1997b. Application of Three-Dimensional Boundary-Fitted Circulation Model To Providence River, published in: Journal of Hydraulic Engineering, Vol. 123, No. 1.

Muin, M., 1993. A Three-Dimensional Boundary-Fitted Circulation Model in Spherical Coordinates, Ph.D. Dissertation, Univ. of Rhode Island, Narragansett Bay Campus, Narragansett, RI.

Peene, S., E. Yassuda and D. Mendelsohn, 1998. Development of a Waste Load Allocation Model within Charleston HarborEstuary. Phase I: Barotropic Circulation. published in proceedings of: 5th International Conference on Estuarine and Coastal Modeling. Ed Malcolm L. Spaulding and Alan F. Blumberg. ASCE, Alexandria, Virginia, October 22-24,1997.

Phillips, Norman, 1956. Monthly Weather Review, AGU.

Stull, Roland B., 1988. An Introduction to Boundary Layer Meteorology. Kluwer Academic Publishers, P.O. Box 17, 3300 AA Dordrecht, The Netherlands.

Swanson, J. C. and D. Mendelsohn, 1996. Water Quality Impacts of Dredging and Disposal Operations in Boston Harbor. presented at: ASCE North American Water and Environmental Congress '96 (NAWEC '96), Anaheim, CA, 22-28 June 1996.

Swanson, J.C., D. Mendelsohn, 1993. Application of WQMAP to upper Narragansett Bay, Rhode Island. Estuarine and Coastal Modeling III. Proceedings of the 3rd International Conference, sponsored by the Waterway, Port, Coastal and Ocean Division of the ASCE, Oak Brook, IL, September 8-10, 1993.

Thomann and Mueller, 1987. Principles of Surface Water Quality Modeling and Control. Harper and Row, Publishers Inc., New York, N.Y.